Multiscale numerical modelling of microstructured reinforced composites

Fermin Otero Gruer

Escola Tècnica Superior d'Enginyers de Camins, Canals i Ports de Barcelona

Universitat Politècnica de Catalunya

Doctoral Thesis
Structural Analysis Programme

Advisors:

Prof. Sergio Oller Martínez

Prof. Xavier Martínez Garcia

November 2015

Multiscale numerical modelling of microstructured reinforced composites

November 2015
Universitat Politècnica de Catalunya
c/ Jordi Girona 1-3, 08034 Barcelona
www.upc.edu

UNIVERSITAT POLITÈCNICA DE CATALUNYA
BARCELONATECH
Escola de Doctorat

Curs acadèmic: 2015/16

Acta de qualificació de tesi doctoral

Nom i cognoms Fermin E. Otero Gruer

Programa de doctorat Anàlisi Estructural

Unitat estructural responsable del programa Departament de Resistència de Materials i Estructures a l'Enginyeria

Resolució del Tribunal

Reunit el Tribunal designat a l'efecte, el doctorand / la doctoranda exposa el tema de la seva tesi doctoral titulada

Multiscale numerical modelling of microstructured reinforced composites.

Acabada la lectura i després de donar resposta a les qüestions formulades pels membres titulars del tribunal, aquest atorga la qualificació:

☐ NO APTE ☐ APROVAT ☐ NOTABLE ☐ EXCEL·LENT

(Nom, cognoms i signatura) President/a	(Nom, cognoms i signatura) Secretari/ària	
(Nom, cognoms i signatura) Vocal	(Nom, cognoms i signatura) Vocal	(Nom, cognoms i signatura) Vocal

_____, _____ d'/de _____ de _____

El resultat de l'escrutini dels vots emesos pels membres titulars del tribunal, efectuat per l'Escola de Doctorat, a instància de la Comissió de Doctorat de la UPC, atorga la MENCIÓ CUM LAUDE:

☐ SÍ ☐ NO

(Nom, cognoms i signatura) President de la Comissió Permanent de l'Escola de Doctorat	(Nom, cognoms i signatura) Secretari de la Comissió Permanent de l'Escola de Doctorat

Barcelona, _____ d'/de _____ de _____

Diligència "Internacional del títol de doctor o doctora"

- Com a secretari/ària del tribunal faig constar que la tesi s'ha defensat en part, i com a mínim pel que fa al resum i les conclusions, en una de les llengües habituals per a la comunicació científica en el seu camp de coneixement i diferent de les que són oficials a Espanya. Aquesta norma no s'aplica si l'estada, els informes i els experts provenen d'un país de parla hispana.

(Nom, cognoms i signatura) Secretari/ària del Tribunal

Acknowledgements

Este trabajo no hubiera podido realizarse sin la ayuda, concejo, colaboración, compañía, cariño y sobre todo paciencia de muchas personas que me han caminado junto a mí hasta llegar hasta aquí.

En primer lugar, un gracias especial a mis directores Sergio y Xavier por la confianza, la paciencia y más paciencia, la sincera dedicación y más que nada, por los consejos en lo académico primero y por los demás, los formativos de vida, los bien intencionados y orientados solo al mejor desarrollo personal sin pensar en nada más, Gracias.

A mi familia, mis padres y hermanos, por su incondicional confianza y apoyo. Por el cariño sincero y permanente, por creer en mí, a veces desmedidamente. Todo eso ha influido positivamente en mí persona empujando hacia adelante, dando ese extra de energía que se necesita en esos momentos de incertidumbre, haciendo creíble eso de "vamos que se puede".

A mis compañeros de oficina y pacillo, los presentes y pasados, por compartir, escuchar, aconsejar y más que nada, soportar. Al café/infusión post almuerzo, en los que tantas veces arreglamos el mundo y más importante, por escucharme y ayudarme a arreglar mi personal mundo.

Una especial gracias en mayúsculas a Raquel mi compañera, amiga y amante. Por tu confianza y paciencia y por escuchar... y volver a escuchar... por dejarte aburrir. Por mostrarme y recordarme por pasivo lo que es importante y lo que no. Por estar conmigo y además por amarme libremente.

Martina, gracias por existir, gracias por tu increíble comprensión, crece pero intenta no cambies tu esencia, eres genial. Te amo por sobre todo lo demás.

Y por supuesto, a todos mis amigos de vida.

This work was financially supported by CIMNE together with the European Community under grant: NMP-2009-2.5-1 246067 M_RECT "Multiscale Reinforcement of Semi-crystalline Thermoplastic Sheets and Honeycombs", by European Research Council through of Advanced Grant:
ERC-2012-AdG 320815 COMP-DES-MAT "Advanced tools for computational design of engineering materials", by Dirección General de Investigación Científica y Técnica:
MAT2014-60647-R OMMC "Optimización multi-escala y multi-objetivo de estructuras de laminados compuestos", by "Abengoa Research", and by Universitat Politècnica de Catalunya (UPC).
All this support is gratefully acknowledged.

Abstract

Most of the existing materials around us can be considered composite materials, since they are composed by several phases or components at certain spatial scale. The physical and chemical properties of composites, as occurs with structures composed by two or more materials, is defined by the response provided by their constituents. Therefore, a good characterization of the composite requires considering the performance of its components. In the last decades, several methods have been proposed with this approach to characterize composite materials, most of them based on multiscale techniques.

Nowadays, multiscale homogenization analysis is a popular topic in the simulation of composite materials. This is because the complexity of new composites demands of advanced analysis techniques for their correct characterization, and thanks to the continuous increase of computational capacity. However, the computational cost when multiscale procedures are taken to the non-linear range and are applied to real-size structures is still excessively high. In this context, this work presents a comprehensive homogenization formulation for an efficient non-linear multiscale modeling of composite structures.

The development of a composite multiscale constitutive model is addressed from two different homogenization approaches. The first one corresponds to a phenomenological homogenization procedure for the non-linear analysis of carbon nanotubes reinforced composites. The second one is a general two-scale homogenization procedure to analyze three-dimensional composite structures.

Carbon nanotubes (CNTs) have been regarded as ideal reinforcements for high-performance composites. The formulation developed takes into account explicitly the performance of the interface between the matrix and the CNTs. The load is transferred to the nanotubes through the considered interface. The composite non-linear behavior results from the non-linearities of its constituents, and in case of interface damage, it also becomes non-linear the law defined to couple the interface with the CNTs. The formulation is validated studying the elastic response and non-linear behavior of several composites.

In the context of multiscale homogenization, a first-order and an enhanced-first-order formulation is developed. The results obtained for laminate composites using the first-order formulation are compared with other microscopic formulations, showing that the homogenization method is an excellent alternative when microstructural effects must be taken into account. Then, a strategy to conduct non-linear multiscale analysis in an efficient way is proposed. The procedure conserves the dissipated energy through the scales and is mesh independent. The analysis of academic examples is used to show the capacity of the non-linear strategy. Finally, the simulation of an industrial composite component proves the performance and benefits of the non-linear homogenization procedure developed.

Contents

List of Figures

List of Acronyms

BVP	Boundary Value Problem
CNTs	Carbon Nanotubes
CVD	Chemical Vapor Deposition
DDM	Discrete Damage Mechanics
FE	Finite Element
FEM	Finite Element Method
FE^2	Finite Element Two-Scale
IFSS	Interfacial Shear Strength
MWCNTs	Multiwall Carbon Nanotubes
NLAF	Non-Linear Activation Function
NLS	Non-Linear Strategy
POD	Proper Orthogonal Decomposition
RVE	Representative Volume Element
SFS	Smart First Step
SP	Serial-Parallel
SWCNTs	Single Wall Carbon Nanotubes

Introduction

The continuum mechanics theory has made a great effort to obtain the behavior of homogeneous materials using physical and mathematical concepts showing a good agreement with reality. Furthermore, the constant develop of computer technology and computer machines has allowed to improve the numerical tools used to simulate mechanical structures. In the numerical simulation field, one of the most extended method used for several applications is the Finite Element Method (FEM) [137]. In a FEM analysis the behavior of the homogeneous materials in the structure is simulated by a specific constitutive law or constitutive model with some calibrated parameters.

The composite materials are non-homogeneous materials formed by two or more different components which can be homogeneous materials or even micro-heterogeneous materials. The homogenized behavior of the composites depends strongly on the internal spatial distribution, the size and the properties of the material components and their respective interfaces. Therefore, composites require more complex and advanced constitutive models than the ones use in single materials.

For a linear analysis or a structural analysis to failure study it is enough simulated the composites with one orthotropic homogenized characterization and a constitutive law with some complexity. However, more realistic composite constitutive models are necessary to simulate the structures beyond their elastic limit, to obtain the post critic behavior of these or to estimate their tenacity and structural integrity.

The direct application of the FEM is not the most appropriate or effective manner to face the described problem. In a classical FEM analysis each component materials have their own constitutive models. Therefore, the numerical model of the structure must to be discretized with a Finite Element (FE) size of at least the size of the components in the composite. In general, this restriction gives as result FE meshes with large number of finite elements which demand an extremely expensive computational cost, or even, in some cases the analysis is unfeasible to perform. Consequently, to analyze composite structures and to characterize their behavior or fracture modes more suitable strategies must be developed.

Background and motivation

The complexity of the composite materials has promoted that several formulations appeared to predict their behavior, which are more o less suitable according to computational cost available, the accuracy in the results desired or even the expected failure type. Further, the development of a new generation of composites with improved properties, more reliable and cheap has extended its use to many industrial application.

The phenomenological homogenization methods are a possibility to analyze composite materials with a heterogeneous internal structure. In this context, the most usual method is the classical mixing theory proposed initially by Truesdell and Toupin [123]. The formulation obtains the homogenized behavior of the composite through the compatibility equation and from the mechanical performance of the component materials, which are simulated with their own constitutive laws. Later, several modifications and extensions of this classical theory of mixtures have enabled the resolution of any composite with reinforced matrix, without the limitation required by the compatibility equation [92].

One of the most significant modifications of the mixing theory is the Serial-Parallel (SP) continuum approach. In the SP formulation the mechanic characteristic of the composite is obtained using not only the properties and constitutive model of the material components but also taking into account their topological distribution [106]. The SP mixing theory assumes a serial-parallel self-adjusting behavior to the topological distribution of fiber embedded in the matrix of the composite material. This approach imposes the iso-strain condition in the fiber alignment direction on the components of the composite (as parallel materials) and the iso-stress condition in the orthogonal direction (as serial materials).

The reinforcements developed today, as the nanofibers or Carbon Nanotubes (CNTs) and the renewed composites as the reinforced concrete with short fibers, require sophisticated formulations for their simulation. The interface zone between matrix and reinforcement has a meaningful effect in the final properties and response of the composite structures made with these current composites. Many effort have been made to consider the debonding phenomenon in laminated composites but it is not enough to totally characterize the behavior of these micro-heterogeneous composites. Therefore, renovated formulations or renewed modifications of existing theories should be developed to face with the challenge of predict the behavior of these new composites.

The homogenization techniques are another option to analyze composite materials. In these methods the characterization of the entire composite is obtained through the analysis of its internal structure or microscopic structure. In this context, an approach extensively used is the called multiscale homogenization method. In general, the formulation is based on the use of the concept of unit cell or Representative Volume Element (RVE) [44]. The definition of the RVE corresponds with a microscopic subregion which is representative of the entire micro-structure (referred as micro-scale) level of the composite. This is employed to determine the homogenized properties and behavior of the composite level (also known as macro-scale). It is assumed that the RVE must contain a sufficient number of inclusions to make the homogenized moduli independent of homogeneous forces or displacements on the RVE boundary.

Within this context, one of the most extended and popular method is the known first-order homogenization approache [117]. This multiscale method uses the macro-scale deformation gradient tensor (or the strain tensor) to solve the micro-scale problem. The composite behavior (the macro-scale stress-strain relationship) is obtained by a detailed modeling of the internal heterogeneous structure of the composite in the RVE. Therefore, the approach does not require any composite constitutive assumption or compatibility equation to address the composite response. Moreover, there are not restriction about the constitutive law of the component materials, even non-linear materials and time-dependency models can be taken into account. The benefits of the method becomes in a challenge when a non-linear analysis of a three-dimensional structure is studied. Considering a FE^2 homogenization technique [116], it is required for each time step to solve one RVE at each point of integration at the macro-scale due to the non-linear threshold and non-linear behavior of the homogenized composite are unknown. Therefore, the spent computational cost in the non-linear analysis of an industrial component by using multiscale FE^2 homogenization is strongly expensive, and in many cases, is unsuitable to perform.

In addition to the computational cost to address the non-linear problem with multiscale homogenization methods, the softening issue must be considered too. The non-linear constitutive law of the component materials are defined in the RVE problem. Consequently, the non-linear behavior starts in the micro-scale and then, it move up to the macro-scale. Because of this, novel multiscale strategies dealing with non-linear problem computationally efficient should be developed taking into account also the conservation of the dissipated energy through the scales. Besides, they must be macro and micro mesh independent for the case of FE^2 homogenization.

In the last decade, a second-order computational homogenization was proposed as a natural extension of the first-order homogenization method [55]. It was developed to be applied in critical regions of intense deformation, where the characteristic wave length of the macro-scale deformation field is of the order of the size of the micro-scale. Therefore, in this approach the macroscopic gradient of the deformation gradient is also incorporated in the microscopic scale problem. The first-order equilibrium problem is conserved in the micro-scale though a higher-order equilibrium problem appears in the macro-scale. The solution of the proposed multiscale approach is made through a complex finite element implementation, which restricted its popular application.

The main advantage of the described second-order homogenization is that can considered intense localization phenomena, then it is a desirable approach for non-linear analysis. On the other hand, the benefit of the first-order homogenization is that considered first-order equilibrium equations at both scales, which represents an advantage from a point of view of computational implementation. Therefore, an enhanced-first-order approach could be an interesting proposed to account second-order effects of the macro-scale from the micro-scale by the incorporation of macroscopic second-order deformation measure in the microscopic BVP.

Objectives

The main objective of this study is developed a comprehensive formulation for the analysis of three-dimensional composite structures in linear and non-linear range. In this context, the partial targets to address the global aim of this dissertation can be written in a synthesized form as

Development of a phenomenological homogenization formulation based on the mixing theory for the analysis of CNTs reinforced composites. The formulation should consider the effect of the CNTs-matrix interface in the composite behavior.

Extension to three dimensions of the first-order multiscale homogenization for the numerical analysis of composite structures. Implementation of an elimination of redundant unknowns method to solve the microscopic boundary value problem considering the constraint conditions on the boundary domain.

Comparison of numerical simulations with other microscopic formulations to show the advantages and drawbacks of the proposed procedure.

Development of a non-linear strategy to optimize the computational cost of the analysis of real-size composites structures using a multiscale homogenization approach.

Improvement of the first-order multiscale approach implemented to consider second-order effects in the microscopic scale from the macroscopic scale.

In parallel to the developments of the described objectives previously other necessary tasks must be addressed to fulfill the main aim. They are

Parallel numerical implementation of the develop approaches through an OpenMP philosophy in a finite element code (PLCd [103]).

Development of a preprocessor manager to deal with the numerical models of the microstructure (RVE) through a problem type at GID [78, 18].

Numerical validation of the different formulations implemented in PLCd through the simulation of several composites and by the analysis of real-structural components.

Outline

In the present dissertation is possible to observe that from a theoretical point of view the main goal can be separated in two parts or two steps. For this reason, the following global document is arranged in two major self-contained sections.

In the Part I of this study a phenomenological homogenization model for the analysis of composites material using CNTs as reinforcement is presented. The formulation developed is based on the mixing theory. In this context, the Chapter 2 shows a review of the state of the art of the classical mixing theory and its subsequent modifications while Chapter 3 introduces general considerations about the CNTs and a state of the art of the production methods and of the measured mechanical properties. Then, Chapter 4 presents the formulation and numerical implementation of the "ad hoc" homogenization model developed in this study. Chapter 5 shows the validation and numerical examples analyzed using the formulation proposed in the above chapter. Finally, in the Chapter 6 the conclusions and future work about the model develop in this part of the dissertation is approached.

On the other hand, in the Part II the developed multiscale homogenization approaches for composite structures are described. The state of the art addressed in Chapter 2 shows the fundamental theories and the latest developments about this research topic. Chapter 3 presents the formulations and implementations of the first-order homogenization and the proposed enhanced-first-order extension to consider second-order effects. In Chapter 4 the implemented two-scale homogenization procedure is compared with other micro-structural formulations. Chapter 5 describes the non-linear strategy proposed for multiscale approaches, also its validation and numerical applications are shown. The conclusions and future work of this second part are addressed in Chapter 6.

In the final conclusions chapter the achievements of the present study are exposed along with concluding remarks and future works derived from this dissertation.

Research dissemination

The work included in this dissertation resulted in the following scientific publications:

Part I

F. Otero, S. Oller, X. Martinez and O. Salomon. Modelling of behaviour of carbon nanotube-reinforced composites. In: *MATCOMP'11 - IX Congreso Nacional de Materiales Compuestos.* Girona, España 2011.

F. Otero, S. Oller, X. Martinez and O. Salomon. Numerical modelling of behaviour of carbon nanotube-reinforced composites. In: *COMPLAS XI - XI International Conference on Computational Plasticity. Fundamentals and Applications.* Barcelona, España, 2011.

F. Otero, S. Oller, X. Martinez and O. Salomon. Modelling the elastic behavior of carbon nanotube-reinforced composites. In: *Composites 2001 - 3rd ECCOMAS Thematic Conference on the Mechanical Response of Composites.* Hannover, Germany, 2011.

F. Otero, S. Oller, X. Martinez and O. Salomon. Modelling viscoelastic behaviour of carbon nanotube-reinforced thermo-plastics. In: *MECOM 2012 - X Congreso Argentino de Mecanica Computacional.* Salta, Argentina, 2012.

F. Otero, X. Martinez, S. Oller and O. Salomon. Study and prediction of the mechanical performance of a nanotube-reinforced composite. *Composite Structures.* 2012, 94(9):2920-2930. doi: 10.1016/j.compstruct.2012.04.001.

Part II

X. Martinez, F. Otero and S. Oller. Strategy for an efficient material non-linear multiscale analysis In: *COMAT 2015 - VI International Conference on Science and Technology of Composite Materials.* Buenos Aires, Argentina, 2015.

F. Otero, S. Oller, X. Martinez and O. Salomon. Numerical homogenization for composite materials analysis. Comparison with other micro mechanical formulations. *Composite Structures.* 2015, 122:405-416. doi: 10.1016/j.compstruct.2014.11.041.

F. Otero, X. Martinez, S. Oller and O. Salomon. An efficient multi-scale method for non-linear analysis of composite structures. *Composite Structures.* 2015, 131:707-719. doi: 10.1016/j.compstruct.2015.06.006.

In addition, part of the work was presented at the following unpublished conferences:

F. Otero, S. Oller, X. Martinez and O. Salomon. *Numerical homogenization for the simulation of composites materials. Comparison with other micro mechanical formulations.* Mechanics of Composites (MECHCOMP2014). Long Island, NY State, USA, 8-12 June 2014.

F. Otero, S. Oller and X. Martinez. *Non-linear multiscale strategy to analyze composite materials efficiently.* 18th International Conference on Composites Structures (ICCS18). Lisbon, Portugal 15-18 June, 2015.

Finally, part of the work presented in this document is the result of the collaborating with external researchers during the following research stays:

WVU-(**W**est **V**irginia **U**niversity), 6-month doctoral research stay. Worked under the direct supervision of Prof. Ever J. Barbero in the Mechanical and Aerospace Engineering of the Benjamin M. Statler College of Engineering and Mineral Resources, WVU. Morgantown, USA. January - June 2014. The following article resulted from the work developed during the stay:

M.M. Moure, F. Otero, S.K. García-Castillo, S. Sánchez-Sáez, E. Barbero and E.J. Barbero. Damage evolution in open-hole laminated composite plates subjected to in-plane loads. *Composites Structures.* 2015, 133:1048-1057. doi: 10.1016/j.compstruct.2015.08.045.

CIMAT-(**C**entro de **I**nvestigación en **MAT**emáticas), 2-month research stay in the framework of the TCAiN-MaND project, a Marie Curie International Research Staff Exchange Scheme (IRSES) under grant agreement FP7-612607. Worked under the direct supervision of Dr. Salvador Botello in the Computational Sciences Department of CIMAT. Guanajuato, México. November - Dicember 2015.

Part I

Phenomenological homogenization

Chapter 1

Introduction

Composites are materials made of at least two different components. Generally, are constituted by a matrix that surrounds the reinforcing elements, which may be in the form of particles, nanotubes, short fibers, fibers, etc [4]. The main function of matrix component is to give cohesion, support the reinforcement and transfer the external actions to the reinforcements. While the main task of the reinforcement component is to improve the matrix properties. The appropriate design of structural elements made of this type of composite material requires the use of composite constitutive models capable of estimating their stiffness, strength and different failure modes.

In case of using fibers or nanotubes as reinforcement components, the performance of the composite depends on the achievement of the following four main characteristics:

Aspect ratio of the fibers. The fiber aspect ratio is a dimensionless geometric measurement that results from dividing the length of the reinforcement by its diameter. This parameter is important because the stress distribution in the reinforcement depends on it [49]. In fibers with high aspect ratios the fiber end effect is less important. The reinforcement is considered to behave as a long fiber when its aspect ratio is larger than 1000.

Dispersion of fibers in the composite. A uniform distribution of reinforcement in the composite is fundamental to ensure that it is completely surrounded by matrix. This is necessary to obtain an effective stress transfer. A good dispersion of the reinforcement in the composite also helps to have a more uniform stress distribution in it, reducing the regions susceptible having stress concentrations.

Fiber alignment. It has been shown that the difference between random distribution and perfect alignment may represent a factor of five in the composite Young's modulus [40]. Fiber alignment also affects the isotropy of the composite, as perfect alignments increase its anisotropy.

Load transmission from the matrix to the fiber. The last and probably most important factor is the interfacial tension between matrix and reinforcement. In general, the loads in a composite structure are introduced through the matrix and are transferred to the reinforcement through the interface [49]. Therefore, the interface can be defined as the region surrounding the reinforcement where this stress transfer takes place. The properties of the composite depend on the properties of this region, and on its ability to transfer the load efficiently.

On the other hand, the external load applied to a composite is shared disproportionately by the different components, as their elastic properties are different. In case of considering an iso-strain hypothesis [123] the stresses on the reinforcement will be larger than in the matrix, as the reinforcement is stiffer than the matrix. This unequal stress distribution generates shear stresses between both materials in a region that can is usually called the interface. The load transfer from the matrix to the reinforcement is produced in this region. Shear stresses in the interface increase proportionally to the external load until a critical value, beyond which the interface breaks. This critical value is known as Interfacial Shear Strength (IFSS) and it limits the stress transfer capacity.

In this context, the classical rule of mixtures was one of the first theory used to address a composite constitutive model from a phenomenological point of view [123]. The theory defines the manner in which all components interact to provide the material performance. The iso-strain hypothesis defined in the mixing theory implies a parallel distribution on the components in the composite. It is possible to think in

an inverse mixing theory which replaces the iso-strain assumption by an iso-stress assumption, therefore it means a serial distribution on the components in the composite. The characterization of the composite depends of the hypothesis used in the formulation. Then, modifications of the mixing theory capable to consider all possible behaviors of the composite: parallel, serial and mixed were proposed [88]. Finally, the serial/parallel concept was introduced in the theory, which replaced the iso-strain hypothesis by an iso-strain condition in the fiber direction and iso-stress condition in the transversal directions [106].

The mixing theory began to be considered as a constitutive equation manager when its hypothesis were coupled with a thermodynamical description of the composite components [96]. Therefore, the formulation obtains the relation between the components even when they have reached their elastic limit. With this at hand, the different failure phenomenons present in the composites such as debonding or delamination were modeled through of the constitutive law of the material components.

1.1 Part's outline

In this part of the dissertation a renewed modification of the mixing theory is proposed to consider the effect of the reinforcement-matrix interface zone in the final response of composite. The present formulation is developed for composites that use CNTs as reinforcement.

Following this aim, the Chapter 2 shows an state of the art of the classical mixing theory and its modifications since the early inclusion of the SP concept until the current sophisticated modifications. While in Chapter 3 a review of the state of the art about the different production methods and measured mechanical properties found in the literature of the CNTs is presented. In this chapter is also addressed the different issues to should be considered in a constitutive formulation for reinforced composites with CNTs.

In Chapter 4 the phenomenological homogenization based in the on the mixing theory is developed. The insertion of the concepts of serial and parallel behavior in the CNTs-matrix bonding through of the definition of a parallel factor is shown. The CNTs debonding phenomena is also considered by a material non-linearity proposed. At the end of the chapter, the implementation in the FEM code PLCd is presented.

Chapter 5 shows the results of validation of the implemented composite constitutive model using information data from literature. The validation of the model is made for linear and non-linear behavior using experimental data of several composites. Then, numerical examples are developed showing the good behavior of the "ad hoc" homogenization model developed.

Finally, In Chapter 6 the conclusions about the composite constitutive formulation developed in this part of the study are in detail addressed.

Chapter 2

State of the art

The first part of the present study proposes a phenomenological composite constitutive model which is based on the classical rule of mixtures. Therefore, in the following a literature review is dedicated to explain this mixing theory and its modifications which have been developed over the years.

2.1 Classical mixing theory

The mixing theory was originally proposed by Truesdell and Toupin [123]. Later, Truesdell [122] extended the theory to linear systems and Green and Adkins [35] presented a general non-lineal constitutive equations. Finally, Ortiz and Popov [97, 98] proposed a general constitutive equations for unreinforced concrete idealized as a composite material.

The classical mixing theory is based on the mechanical of local continuous solid and it is appropriated to explain the behavior of a point in a solid compound. It is based on the principle of interaction of the component substances in the composite material, assuming the following hypothesis: *i*) on each infinitesimal volume of the composite are involved a set of component substances,*ii*) each component contributes to the behavior of the compound material in the same proportion as their volumetric fraction, *iii*) all component materials have the same deformation (compatibility equation or closure equation) and *iv*) the occupied volume of each component is much smaller than the total volume of the composite.

The second hypothesis implies a homogeneous distribution of all substances in the compound material. The volume fraction, the internal distribution and the interaction between the different substances components, which have its respective constitutive law, determine the behavior of the composite material. This allows combining materials with different behavior (elastic, elasto-plastic, elasto-damage, etc.), which have an evolutionary behavior governed by its own law and internal variables [98, 96].

The third hypothesis demands that the following condition of compatibility must be fulfilled

$$\varepsilon_{ij} = (\varepsilon_{ij})_1 = (\varepsilon_{ij})_2 = \cdots = (\varepsilon_{ij})_n \,, \tag{2.1}$$

where the assumption of infinitesimal deformations on each components are considered and where, ε_{ij} and $(\varepsilon_{ij})_n$ are the strain tensors of the composite and of the $n-th$ component of the compound material, respectively.

The specific Helmholtz free energy of the composite is given by the sum of the specific Helmholtz free energies of each components of the composite multiplied by its volume fraction, that is

$$\Psi\left(\boldsymbol{\varepsilon}^e, \theta, \boldsymbol{\alpha}\right) = \sum_{c=1}^{n} k_c \Psi_c \left(\boldsymbol{\varepsilon}_c, \boldsymbol{\varepsilon}_c^p, \theta, \boldsymbol{\alpha}_c\right), \tag{2.2}$$

where Ψ_c is the specific Helmholtz free energy, k_c is the volume fraction, $\boldsymbol{\varepsilon}_c^p$ is the plastic strain tensor and $\boldsymbol{\alpha}_c$ are the inner variables of each one of the $n-th$ components in the composite.

The volume fraction coefficient allows to consider the contribution of each material to the composite and it is obtained with the following equation as

$$k_c = \frac{dV_c}{dV_0}, \tag{2.3}$$

where dV_c is the volume of the $c-th$ component and dV_0 is the total volume of the composite. The volume fractions of the components must to satisfied the following condition:

$$\sum_{c=1}^{n} k_c = 1. \tag{2.4}$$

Equation (2.4) guarantees the conservation of mass. Following with the procedure used for a simple material [91, 66, 65, 95], from the Clausius-Duhem inequality and applying the Coleman method, the constitutive equation of the composite is obtained as

$$\sigma_{ij} = \frac{\partial \Psi\left(\varepsilon_{ij}, \theta, \alpha_i\right)}{\partial \varepsilon_{ij}} = \sum_{c=1}^{n} k_c \frac{\partial \Psi_c\left(\varepsilon_{ij}, \theta, \alpha_i\right)}{\partial \varepsilon_{ij}} = \sum_{c=1}^{n} k_c \left(\sigma_{ij}\right)_c, \tag{2.5}$$

where, σ_{ij} and $\left(\sigma_{ij}\right)_c$ are the stress tensors of the composite and of the $c-th$ component of the compound material, respectively. The composite constitutive tensor is obtained considering the variation of the composite stress tensor respect to the strain tensor, therefore

$$C_{ijkl} = \frac{\partial \sigma_{ij}}{\partial \varepsilon_{kl}} = \frac{\partial^2 \Psi\left(\varepsilon_{ij}, \theta, \alpha_i\right)}{\partial \varepsilon_{ij} \partial \varepsilon_{kl}} = \sum_{c=1}^{n} k_c \left(C_{ijkl}\right)_c. \tag{2.6}$$

However, the closure equation given by (2.1) imposes a strong limitation of the classical theory of mixtures because it is strictly valid only for composites with parallel behavior. Moreover, this limitation is extended to non-linear range because each component can have different deformation for a given load step. Because of this, several formulations have been proposed from the classical mixing theory in order to consider different internal behavior (not only parallel behavior) and the nonlinearity of each components too.

2.2 Modifications to the mixing theory

Over the years the classical mixing theory has had many modifications and improvements with the objective of expanding its scope. Some of the most relevant developments are presented in this section.

2.2.1 Mixing theory using serial-parallel model

The classical theory of mixtures was modified by Oller et al. [94] and Neamtu et al. [88] introducing the serial-parallel concept. The model allows to represent composites for various possible combinations of serial and/or parallel behavior of their components. The properties of the composite are obtained using the properties of each component and taking into account its topological distribution. The modification is based on the definition of the total strain field as a weighted sum of the contributions of the deformation components in series and parallel. Therefore

$$\varepsilon_{ij} = (1 - \aleph)\, \varepsilon_{ij}^{par} + \aleph\, \varepsilon_{ij}^{ser}, \tag{2.7}$$

where ε_{ij} is the total strain tensor of the composite, ε_{ij}^{par} and ε_{ij}^{ser} represent the parallel and serial strain tensor, respectively. And $\aleph$ is the coupling parameter that relates in weighted form the serial-parallel behavior, it has a value range since 0 to 1. The deformation components in parallel and serial behavior are approximated by

$$\varepsilon_{ij}^{par} \approxeq \frac{1}{n} \sum_{c=1}^{n} \left(\varepsilon_{ij}\right)_c \qquad , \qquad \varepsilon_{ij}^{ser} = \sum_{c=1}^{n} k_c \left(\varepsilon_{ij}\right)_c. \tag{2.8}$$

This modification of the classical mixing theory has the disadvantage that the coupling parameter, in general, must be calibrated with experimental tests of the composite.

2.2.2 Generalized mixing theory

The proposed modification of the classical theory of mixtures by Oller [92] is a generalization of this theory. The new proposed is enabled to solve any reinforced matrix composite, without the limitation of

the compatibility equation (see (2.1)) required by the classical theory. The closure equation is satisfied automatically by the proposed modification. The fundamental hypothesis of this theory's generalization is a new definition of the third hypothesis of the classical theory. The new third hypothesis is: *iii*) the components must satisfy a generalized compatibility equation to fit the topology of the serial-parallel composite. The new hypothesis allows establishing the relationship between the composite deformation and the deformation of each component. The new compatibility equation provides the link between the parallel behavior and the serial behavior and can be expressed as

$$(\varepsilon_{ij})_c = \underbrace{(1-\chi_c)\cdot I_{ijkl}\,\varepsilon_{kl}}_{(\varepsilon^{par}_{ij})_c} + \underbrace{\chi_c\cdot[(\phi_{ijkl})_c\cdot(\varepsilon_{kl}-\varepsilon^p_{kl})+(\varepsilon^p_{kl})_c]}_{(\varepsilon^{ser}_{ij})_c}, \tag{2.9}$$

where $(\varepsilon_{ij})_c$ is the strain tensor of the $c-th$ component, which can be separated in its parallel $(\varepsilon^{par}_{ij})_c$ and serial $(\varepsilon^{ser}_{ij})_c$ component, respectively, and ε_{ij} is the total strain tensor in the composite. Equation (2.9) can be rewritten as

$$(\varepsilon_{ij})_c = [(1-\chi_c)\cdot I_{ijkl}+\chi_c\cdot(\phi_{ijkl})_c]:\varepsilon_{kl}-\chi_c(\hat{\varepsilon}^p_{kl})_c, \tag{2.10}$$

where $(\hat{\varepsilon}^p_{kl})_c$ is a plastic strain tensor without physical meaning, which is defined only for operating purpose and it is obtained from the plastic strain tensor of the composite distributed among its components according to $(\phi_{ijkl})_c\,\varepsilon^p_{kl}$ and the plastic strain tensor of the current component $(\varepsilon^p_{kl})_c$. The serial-parallel coupling parameter is defined as $0 \leq \chi_c = \sin\alpha_\chi \leq 1$, where α_χ corresponds to the existing angle between the reinforcement orientation and the orientation of the higher principal stress.

2.2.3 Mixing theory expressed in finite strains

The extension to finite strains of the classical theory of mixtures considers that the third hypothesis (original closure equation given by (2.1)) must be verified on the referential configuration and on the spatial configuration for each component[11]

$$\begin{aligned} E_{ij} &= (E_{ij})_1 = (E_{ij})_2 = \cdots = (E_{ij})_n \\ e_{ij} &= (e_{ij})_1 = (e_{ij})_2 = \cdots = (e_{ij})_n, \end{aligned} \tag{2.11}$$

where E_{ij} is the Green-Lagrange strain tensor and e_{ij} is the Almansi strain tensor. Considering the definition of the right Gauchy-Green tensor and (2.11) the compatibility equation can be written as a function of the deformation gradient tensor as

$$F_{ij} = (F_{ij})_1 = (F_{ij})_2 = \cdots = (F_{ij})_n. \tag{2.12}$$

The others hypothesis of the classical theory must be also verified. The relationship between the volume of a component in the spatial configuration and in the referential configuration is given by the determinant of the deformation gradient tensor and it is

$$dV_c = \frac{1}{J}dv_c. \tag{2.13}$$

With (2.13) it is possible to demonstrate that the volume fraction of the components do not change in both configurations.

The solution process starts by estimating the strain increments at the reference configuration and then through tensor transport operations ("push-forward") the strain tensor in the updated configuration it is obtained. The constitutive equation of each components of the composite is integrated in the updated configuration. Each of these components may have different kinds of constitutive behavior (plasticity, damage, etc.) and also, these constitutive models may be isotropic or anisotropic. Then, with the integrated stress state of the components it is possible to obtain the stress state and the constitutive tensor of the composite. Finally, the obtained composite informations are transported ("back-forward") to the reference configuration and then, the internal forces are computed. The balance between the internal forces and applied external forces is verified in an iterative procedure until convergence.

2.2.4 Generalized mixing theory expressed in finite strains

The procedure to extend the generalized theory of mixtures to finite strains is the same than the one used to extend the classical mixing theory in Section 2.2.3. This generalized theory starts with the non-compliance of the classical compatibility equation. Therefore, the proposed new closure equation given by (2.10) must be written now in the reference and the updated configuration, that is

$$\begin{aligned}(E_{ij})_c &= [(1-\chi_c)\cdot I_{ijkl} + \chi_c\cdot(\Phi_{ijkl})_c] : E_{kl} - \chi_c(\hat{E}^p_{kl})_c \\ (e_{ij})_c &= [(1-\chi_c)\cdot I_{ijkl} + \chi_c\cdot(\phi_{ijkl})_c] : e_{kl} - \chi_c(\hat{e}^p_{kl})_c.\end{aligned} \tag{2.14}$$

Equations (2.14) give the strain tensors for each component in both configurations. The constitutive equations are obtained following a similar formulation used in the classical theory of mixtures in finite strains. Finally, the stress tensors of the composite in the reference configuration $\mathbf{S}$ and in the current configuration, the Kirchoff stress tensor $\boldsymbol{\tau}$ are, respectively

$$\mathbf{S} = \sum_{c=1}^{n} k_c [(1-\chi_c)\cdot\mathbf{I}_4 + \chi_c\cdot(\Phi)_c]^T : [(\mathbf{C}^S)_c : [(1-\chi_c)\cdot\mathbf{I}_4 + \chi_c\cdot(\Phi)_c] : (\mathbf{E}^e)_c] \tag{2.15}$$

$$\boldsymbol{\tau} = \sum_{c=1}^{n} k_c [(1-\chi_c)\cdot\mathbf{I}_4 + \chi_c\cdot(\Phi)_c]^T : [(\mathbf{c}^\tau)_c : [(1-\chi_c)\cdot\mathbf{I}_4 + \chi_c\cdot(\Phi)_c] : (\mathbf{e}^e)_c] = J\boldsymbol{\sigma}, \tag{2.16}$$

where $\mathbf{I}_4$ is the fourth order identify tensor, $(\mathbf{C}^S)_c$ and $(\mathbf{c}^\tau)_c$ are the tangent constitutive tensors for the $c-th$ component in each configuration, $(\mathbf{E}^e)_c$ and $(\mathbf{e}^e)_c$ are the elastic strain tensors and $\boldsymbol{\sigma}$ is the Cauchy stress tensor.

2.2.5 Mixing Theory by short fiber reinforcements

The formulation of the mixing theory is oriented to a composite where the reinforcements are long fibers, and the condition of the compatibility equations is verified. However, when the aspect ratio of the fiber decreases, the condition of fiber-matrix compatibility is not satisfied. This is because the effect of slip and the limit transmission of forces between fiber and matrix at the ends of the fiber take increasingly significant. This situation creates conditions of stress concentration and distortion in the fiber and the surrounding matrix because of the discontinuity. The effectiveness of the fibers in the composite stiffness decreases when the length of the fiber decreases.

Equation (2.17) shows the axial stress distribution along the fiber [49] as

$$\sigma_f(x) = C_f^\sigma E_m \left[1 - \frac{\cosh\left(\beta\left(\frac{l}{2} - x\right)\right)}{\cosh\left(\beta\frac{l}{2}\right)}\right] \qquad \forall \quad 0 \le x \le \frac{l}{2}, \tag{2.17}$$

where C_f^σ is the Young's modulus, l is the length of the reinforcement, E_m is the longitudinal strain of the matrix and the parameter β is defined as

$$\beta = \sqrt{\frac{G_c}{C_f^\sigma}\frac{2\pi}{A_f ln\frac{r'}{r}}}, \tag{2.18}$$

where A_f is the cross section of the fiber, G_c is the shear modulus of the composite and r' is the mean distance between the reinforcing fibers.

One way to consider the contribution of the short fiber reinforcement in the classical mixing theory is through the average stress along the fiber, then

$$\bar{\sigma}_f = \frac{1}{l}\int_0^l \sigma_f(x)\,dx = C_f^\sigma\left[1 - \frac{\tanh\left(\beta\frac{l}{2}\right)}{\left(\beta\frac{l}{2}\right)}\right]E_m = \widetilde{C}_f^\sigma E_m. \tag{2.19}$$

Here, $\widetilde{C}_f^\sigma$ is the average or homogenized Young's modulus of the reinforcement, which is function of the length of the fiber and of the geometric parameters of the composite.

The obtained short fiber homogenized Young's modulus is smaller than the real fiber Young's modulus, this shows that its participation on the mechanical properties of the composite depend not only of its

mechanical properties but also of the overall properties of the matrix-reinforcement assemblage. The same concept used to homogenize the stress along the fiber can be extended to get the three dimension homogenized constitutive tensor of the short fiber reinforcement as

$$\widetilde{C}_f^S = C_f^S \left[1 - \frac{\tanh\left(\beta \frac{l}{2}\right)}{\left(\beta \frac{l}{2}\right)} \right], \tag{2.20}$$

where C_f^S is the orthotropic constitutive tensor in the referential configuration of the reinforcement. Using the previously described concept, the incorporation of the short fiber in the theory of mixtures can be extend to finite strains too [92].

2.2.6 Serial-Parallel (SP) continuum approach

The SP continuum approach proposed by Rastellini et al.[106] has as principal hypothesis assumes that the components of the composite behave as parallel materials in the fibers alignment direction and as serial materials in the orthogonal direction. The model makes the composite behavior dependent on the constitutive laws of the component materials and of their morphological distribution inside the composite. The proposed composite model is based on the appropriate management of the constitutive models of component phases within a continuum framework by making use of suitable 'closure equations' that characterize the composite micro-mechanics.

In this theory the definition of a material model for the composite needs the introduction of additional equations that specify somehow the interaction between the component phases. Then, the resulting material model will depend crucially on the adopted specific additional equations that characterizes the mechanical interaction at the micro-scale. These additional sets of equations are referred to as closure equations and are obtained taking the iso-strain hypothesis in fiber direction and iso-stress hypothesis in transversal directions, then

$$\begin{aligned} {}^m\varepsilon_P &= {}^f\varepsilon_P \\ {}^m\sigma_S &= {}^f\sigma_S, \end{aligned} \tag{2.21}$$

where ε and σ are the total strain and the stress, the subscripts S and P correspond to the serial and parallel behavior and the superscripts f and m denote the quantities related to the fiber and matrix, respectively.

This new kind of serial-parallel mixing theory was extended to tri-dimensional framework by Martinez et al. [71] and applied for the numerical simulation of structures of reinforced concrete retrofitted with carbon fiber reinforced polymers. In this study the tangent constitutive tensor of each component of the composite is obtained by means of a perturbation method.

Chapter 3

Considerations about nanotubes

Since their discovery by Lijima in 1991 [48], CNTs are considered a new generation of reinforcements [17]. Their "nano" size structure makes them potentially free of defects, which gives them with excellent physical properties [108, 109]. A nanotube is a tubular cylinder formed by sp2 bonds between the carbon atoms along its length. There are two main nanotube types: Single Wall Carbon Nanotubes (SWCNTs), which are made of a single wall tube with an outer diameter in the order of 1 nm; and Multiwall Carbon Nanotubes (MWCNTs), which consist in several concentric walls, one inside the other, separated by a distance of 0.34 nm [48]. The diameters range of MWCNT varies from 2 to 100 nm. MWCNT can have lengths up to 100 μm.

Carbon nanotubes can be obtained by several procedures. The first method used was the arc-discharge [10], which consists in generating an arc discharge between two graphite electrodes in an inert gas atmosphere at low pressure. The continuous electric discharge sublimates the carbon atoms of the electrodes and forms a plasma around them. This method produces free defect nanotubes along their length. The length of these nanotubes can reach 50 μm. Another procedure is the laser ablation. This consists in vaporizing the graphite by radiation with a laser pulse, in an inert gas atmosphere, inside a high temperature reactor. The nanotubes are formed when the graphite vapor touches the cold walls of the reactor. Finally, the most common procedure used for commercial production of carbon nanotubes is the deposition of Catalytic Vapour Phase (also named, Chemical Vapor Deposition (CVD)). This procedure allows producing large amounts of nanotubes at a low cost. This method prepares a substrate with a metal layer. The nanotube diameter depends on the size of the metal particles. The process starts by mixing two gases; one of them is used as a source of carbon, and the other for the process itself. The nanotubes grow on the side of the metal catalyst. The generated nanotubes have defects on its surface. This method can provide oriented nanotubes if there is plasma during their growth.

Nanotubes obtained by arc-discharge have Young's modulus values in the order of 1TPa. Recent measurements carried out in arc-MWCNTs (multiwall nanotubes made by arc-discharge) have provide Young's modulus values with values varying from 0.27 to 0.95 TPa, ultimate strain values higher than 12%, and ultimate tensile stresses in the range of 11 to 63 GPa [133]. In these measurements it was also obtained the stress-strain curve of the MWCNTs with help an electric microscope.

The properties obtained for CVD-MWCNTs (multiwall carbon nanotubes obtained by CVD) are low due to the defects in the nanotubes surface. The firsts Young modulus measurement known was made with an atomic force microscope [110] and the values obtained were in the range of 12 to 50 GPa. Later on, new measurements have shown Young modulus values in order of 0.45 TPA, and ultimate tensile stresses of 3.6 GPa [131]. The lower measured values were associated with defects in the nanotube and with the slipping of the inner tubes in MWCNTs. The difference in measured values between CVD-MWCNTs and arc-MWCNTs shows the influence of defects on the properties of these new materials.

It is not entirely clear which nanotube type performs better as a reinforcement. A recent study made by Cadeck et al. [9] comparing the properties of a polyvinylalcohol (PVA) matrix reinforced with different types of CNTs nanotubes (double wall nanotubes (DWCNT), SWCNTs, arc-MWCNTs and CVD-MWCNTs) showed that the effectiveness of reinforcement is inversely proportional to its diameter, except when using SWCNTs. The study also proved that the composite properties are proportional to the total interface area. The composite reinforced with SWCNTs had the lowest properties; this result is associated with slipping of SWCNTs inside the bundles. Finally, the study states that the best properties are obtained with the CVD-MWCNTs with smaller diameter.

Currently, there are several methods that can be used to produce nanotube-reinforced composites. The choice of the most appropriate method depends of nature of the involved components [17]. All methods seek to produce a composite with a good dispersion of the CNT reinforcement and to create an interface capable of transmitting the external load to the nanotubes. The manufacturing process has to be selected taking into account that it must not affect the properties of the composite components.

Several studies have shown that the composite formation generates an interface zone around the carbon nanotubes. This interface has a different morphology and properties than the original matrix [77, 76]. The size, shape and properties of the interface have a strong dependence on the matrix type [132] and the formation process. Pull out experimental tests indicate that IFSS values are much higher than the theoretical ones [124], which are calculated using the shear strength of the matrix. This result suggests that the interface region around the nanotube has better properties than the rest of the matrix [19]. Some studies estimate that in this region matrix properties may improve by an order of magnitude [3]. Fracture surface images obtained from composites with strong nanotube-matrix bond show that the interface zone has a thickness several times larger than the nanotube diameter [26, 114]. In the case of semi-crystalline matrices, the interface zone is associated with crystal nucleation around the nanotubes [113].

All manufacture processes seek to obtain a composite with a strong bond between the nanotube and the matrix, in order to transfer effectively the loads. The IFSS defines the capacity of the bond. Values of 500 MPa have been obtained for the IFSS when observing the stresses induced to a broken nanotube, these values where obtained using a Transmission Electron Microscope (TEM). The study attributes this value to the presence of covalent bonds between the matrix and the nanotube [126]. Molecular Dynamics (MD) simulations carried out confirm that strong bonds are obtained when these are covalent. In fact, the transfer load of the interface increases by an order of magnitude with just a 1% of covalent bonds in its surface [29]. On the other hand, the generation of many covalent bonds in the interface is detrimental to the intrinsic properties of the nanotube [29, 30].

When there are not covalent bonds, the interaction between matrix and nanotube is made with Van der Waals forces. Several studies show that this union is weaker. Molecular Dynamics simulations made by [29] predicted values of the IFSS that do not exceed 2.8 MPa. Another study made by [62] predicted values up to 160 MPa. According to [63], the differences in the results depend on the polymer type and they can be in the range of 80 to 135 Mpa. The difference in the results, and the good values of IFSS, were attributed to the morphology and the capacity of the matrix to generate helical chains around the nanotube. On the other hand, nanotubes have a smoother outer surface and therefore, the contribution of the frictional forces to the IFSS are an order of magnitude lower [2].

Experimental results of pull-out tests show values of IFSS between 20-90 MPa [3, 2]. Other experiments using the drag-out technique have shown values between 35-376 MPa [19]. The disparity of the results suggests that is not always possible to generate covalent bonds. The maximum values obtained experimentally are associated to covalent bonds and consider that the interface zone has better properties than the rest of the matrix.

Carbon nanotubes, mainly SWCNTs, tend to agglomerate. This makes very difficult to obtain a good dispersion of those in the polymer. Besides, the smooth surface of the nanotubes leads to a possible lack of bond between the nanotube and the matrix. Currently these problems are solved with a chemical functionalization of the CNTs. The covalent functionalization can be done by modifying the carboxylic acid groups on the nanotube surface and or by direct addition of reagents. The drawback of functionalizing the nanotubes is that there is an intrinsic degradation of their properties [30]. In general, two different methods have been used for the functionalization: “grafting from” and “grafting to”.

The “grafting from” method is based on the initial immobilization of initiators on the nanotube surface, followed by an in situ polymerization of the suitable matrix for the formation of polymer molecules around the nanotube [47, 130]. The advantage of this method is that it allows the formation of composites with a high density of nanotubes. The disadvantage is that this method requires strict control of the quantities and the conditions in which the polymerization reaction takes place.

The “grafting to” method makes the union of preformed polymer molecules to functional groups on the surface of the nanotube through chemical reactions [64, 7]. The advantage of this method is that it can be used with commercial polymers. However, it has as a limitation that the initial union of the polymer chains inhibits the diffusion of macromolecules to the surface. Therefore, the density of functionalization is low.

The above description shows that the final properties of the composite depend on many parameters. Together with these, there are others aspects that may also condition the final properties of the composite,

such as the undulation and misalignment of the nanotubes inside the matrix. All this variability can be considered the responsible of not having yet an accepted theory capable of describing correctly the performance of nanotube-reinforced composites. It is also the reason because the existing theories fail in their predictions. Comparisons between measured mechanical properties and theoretical results, show that the theoretical predictions are generally three times higher than measured results [114, 23].

Chapter 4

Formulation and numerical implementation

Carbon nanotubes have been regarded as ideal reinforcements of high performance composites. A key factor for the reinforcement efficiency is the interface bonding between the CNTs and the matrix. In this chapter the formulation and numerical implementation of a new constitutive model to predict the performance of composites made of CNTs is presented. The composite constitutive model takes intro account explicitly the mechanical performance of the interface between the matrix and the CNTs. The proposed model is based in the classical mixing theory. As it is written, the mixing theory can be understood as a constitutive model manager. Therefore, the mechanical performances of the composite are obtained from the behavior of the composite components, each one simulated with its own constitutive law [11]. The present new composite constitutive model is formulated with the same philosophy, which increases its versatility and simulation capability.

4.1 Description of the composite constitutive model

The proposed composite constitutive model assumes that the composite is a combination of three different materials: matrix, CNTs and an interface [16]. The interface component corresponds to the matrix that surrounds the CNTs. It is considered as an independent component, with its own constitutive law. The interface is used to define the capacity of the matrix to transfer the loads to the reinforcement.

Although the phenomenological performance of the composite already justifies the definition of an interface material; images obtained with Scanning Electron Microscope (SEM) of CNTs reinforced composites, such the ones shown in Figure 4.1, prove its actual existence. These images reveal that the structures protruding from the fractured surface have larger diameters than the original MWCNTs used in the sample preparation [26]. The material surrounding the CNTs corresponds to the interface. The presence of an interface, as a differentiable material, is also proved by Differential Scanning Calorimetry (DSC) measurements carried out in composites with a semi-crystalline polymer as matrix. These measurements show a linear increase of crystalline matrix as the nanotube volume fraction increases, suggesting that each nanotube has a crystalline coating [8].

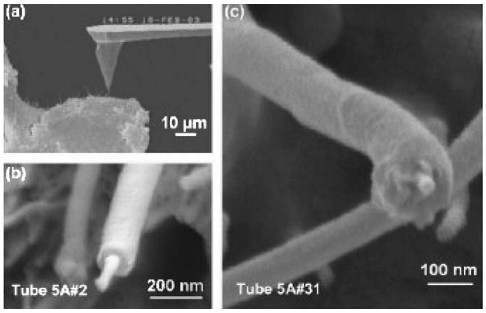

Figure 4.1: SEM image of nanomanipulation and fracture surface of composites [26].

Once having conveyed the necessity of including the interface material in the formulation to simulate the mechanical performance of CNTs reinforced composites, in the following is described the new procedure proposed, which is summarized in Figure 4.2. This figure shows that the composite is divided in several layers, each one containing carbon nanotubes with a different orientation. All layers are coupled together using the parallel mixing theory. This is, assuming that all layers have the same deformation. The new formulation developed provides the mechanical performance of each layer by combining the response of the three coexisting materials: matrix, interface and CNTs. The layer response depends on the materials and on their volumetric participation in the composite.

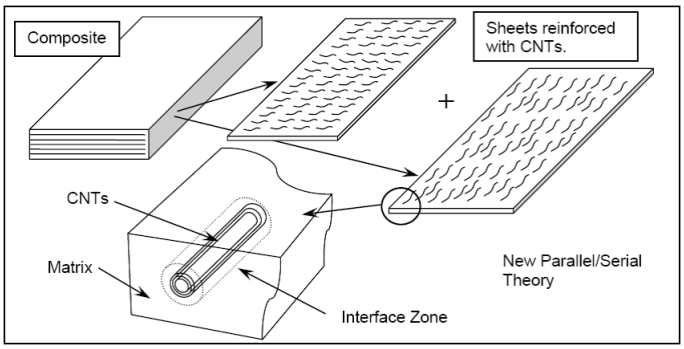

Figure 4.2: Representation of formation for reinforced composite.

First, the layer is split into matrix and a new material that results of coupling the CNTs with the interface. The relation between the matrix and the CNT-interface material is established in terms of the parallel mixing theory (they are assumed to have an iso-strain behavior). On the other hand, CNTs and the interface are coupled together with a combination of parallel and serial mixing theories. The serial mixing theory assumes that all components have the same stresses.

Figure 4.3 shows scheme used to obtain the performance of the CNT-interface material. This is based in the short-fiber model developed by Jayatilaka [49]. According to this model, the load is transferred from the interface to the nanotube at the ends of the reinforcement, through shear stresses. In this region normal stresses in the fiber increase from zero to their maximum value, which is reached in the central part of the reinforcement. In this region there is not load transfer and shear stresses are null. This whole stress transfer scheme can be simplified assuming a CNT-interface performance defined by a serial mixing theory at the ends of the reinforcement and a parallel mixing theory at the center of it.

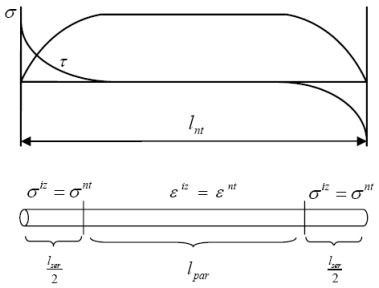

Figure 4.3: Different regions in the new material CNT-interface.

A parallel factor named N^{par} is defined to differentiate these two regions. This parameter, multiplied by the nanotube length, provides the length of the nanotube-interface element with a parallel behavior. The length with a serial performance is defined by the complementary factor.

4.2 Formulation of the composite constitutive model

The Helmholtz free energy [67] of a material point subjected to infinitesimal deformations can be described with the following thermodynamic formulation [96, 66]

$$\Psi = \Psi\left(\boldsymbol{\varepsilon}, \theta, \boldsymbol{\alpha}\right), \tag{4.1}$$

where $\boldsymbol{\varepsilon}$ is the strain tensor, θ a measure of temperature and $\boldsymbol{\alpha} = \{\boldsymbol{\varepsilon}^p, d, s\}$ a set of inner variables, for example: $\boldsymbol{\varepsilon}^p$ is the plastic strain tensor, d damage inner variable and s any other material internal variables.

The proposed model simulates the composite combining the different components using the serial and parallel mixing theories. If this combination is performed according to what has been described in previous Section 4.1, the expression of the Helmholtz free energy may be written as

$$\begin{aligned}\Psi \quad &= k_m \Psi_m + \\ &+ (k_{nt} + k_{iz}) [\underbrace{N^{par} (\overline{k}_{nt} \Psi_{nt} + \overline{k}_{iz} \Psi_{iz})}_{\tilde{\Psi}^{par}_{ntiz}} + \underbrace{(1 - N^{par}) (\overline{k}_{nt} \Psi_{nt} + \overline{k}_{iz} \Psi_{iz})}_{\tilde{\Psi}^{ser}_{ntiz}}],\end{aligned} \tag{4.2}$$

where Ψ_m, Ψ_{nt} and Ψ_{iz} are the specific Helmholtz free energy for the matrix, the nanotube and the interface components, respectively; k_m, k_{nt} and k_{iz} are the volume fraction of each component, N^{par} is the parallel factor and,

$$\overline{k}_{nt} = \frac{k_{nt}}{k_{nt} + k_{iz}} \qquad \overline{k}_{iz} = \frac{k_{iz}}{k_{nt} + k_{iz}} \tag{4.3}$$

are the volume fractions of the carbon nanotubes and the interface in the new CNT-interface material. These volume fractions must verify

$$k_m + k_{nt} + k_{iz} = 1 \qquad \overline{k}_{nt} + \overline{k}_{iz} = 1. \tag{4.4}$$

The relation among the strain tensors of the different components is

$$\boldsymbol{\varepsilon} = \boldsymbol{\varepsilon}_m = \boldsymbol{\varepsilon}^{par}_{ntiz} = \boldsymbol{\varepsilon}^{ser}_{ntiz}, \tag{4.5}$$

being $\boldsymbol{\varepsilon}$ and $\boldsymbol{\varepsilon}_m$ the composite and matrix strain tensor, respectively; $\boldsymbol{\varepsilon}^{par}_{ntiz}$ the strain tensor of the new CNT-interface material with a parallel behavior; and $\boldsymbol{\varepsilon}^{ser}_{ntiz}$ the strain tensor of the CNT-interface material with a serial behavior.

The tangent constitutive tensor of the composite material may be derived from (4.2) as

$$\mathbf{C} = \frac{\partial^2 \Psi}{\partial \boldsymbol{\varepsilon} \otimes \partial \boldsymbol{\varepsilon}} = k_m \frac{\partial^2 \Psi_m}{\partial \boldsymbol{\varepsilon}_m \otimes \partial \boldsymbol{\varepsilon}_m} + \frac{\partial^2 \tilde{\Psi}^{par}_{ntiz}}{\partial \boldsymbol{\varepsilon}^{par}_{ntiz} \otimes \partial \boldsymbol{\varepsilon}^{par}_{ntiz}} + \frac{\partial^2 \tilde{\Psi}^{ser}_{ntiz}}{\partial \boldsymbol{\varepsilon}^{ser}_{ntiz} \otimes \partial \boldsymbol{\varepsilon}^{ser}_{ntiz}}. \tag{4.6}$$

A parallel behavior means that all composite constituents have the same strain value. Therefore:

$$\boldsymbol{\varepsilon}^{par}_{ntiz} = \boldsymbol{\varepsilon}_{nt} = \boldsymbol{\varepsilon}_{iz} \tag{4.7}$$

$$\frac{\partial^2 \tilde{\Psi}^{par}_{ntiz}}{\partial \boldsymbol{\varepsilon}^{par}_{ntiz} \otimes \partial \boldsymbol{\varepsilon}^{par}_{ntiz}} = N^{par} \left[\overline{k}_{nt} \mathbf{C}_{nt} + \overline{k}_{iz} \mathbf{C}_{iz} \right] = N^{par} \mathbf{C}^{par}_{ntiz}. \tag{4.8}$$

And, a serial behavior means that all composite constituents have the same stress value. Thus:

$$\begin{gathered}\boldsymbol{\sigma}^{ser}_{ntiz} = \boldsymbol{\sigma}_{nt} = \boldsymbol{\sigma}_{iz} \\ \boldsymbol{\varepsilon}_{nt} = \mathbf{C}^{-1}_{nt} : \mathbf{C}^{ser}_{ntiz} : \boldsymbol{\varepsilon}^{ser}_{ntiz} \quad ; \quad \boldsymbol{\varepsilon}_{iz} = \mathbf{C}^{-1}_{iz} : \mathbf{C}^{ser}_{ntiz} : \boldsymbol{\varepsilon}^{ser}_{ntiz}\end{gathered} \tag{4.9}$$

$$\frac{\partial^2 \tilde{\Psi}^{ser}_{ntiz}}{\partial \boldsymbol{\varepsilon}^{ser}_{ntiz} \otimes \partial \boldsymbol{\varepsilon}^{ser}_{ntiz}} = (1 - N^{par}) \left[\overline{k}_{nt} \mathbf{C}^{-1}_{nt} + \overline{k}_{iz} \mathbf{C}^{-1}_{iz} \right]^{-1} = (1 - N^{par}) \mathbf{C}^{ser}_{ntiz}. \tag{4.10}$$

Replacing (4.8) and (4.10) in (4.6) it is possible to obtain a simplified expression of the tangent constitutive tensor as

$$\mathbf{C} = k_m \mathbf{C}_m + (k_{nt} + k_{iz}) \left[N^{par} \mathbf{C}^{par}_{ntiz} + (1 - N^{par}) \mathbf{C}^{ser}_{ntiz} \right]. \tag{4.11}$$

The formulation developed require all composite components to fulfill the expression given by (4.1). Therefore, it is possible to use any constitutive law to describe the mechanical performance of the different components.

4.2.1 Definition of the parallel factor

The parallel factor is defined as

$$N^{par} = \frac{l_{par}}{l_{nt}} \quad , \quad 0 \leq N^{par} \leq 1, \tag{4.12}$$

where l_{nt} is the length of the nanotube and l_{par} is function of geometry and mechanical properties of the nanotube and the interface. The value of this length can be obtained from the equation of tension distribution in a reinforcement considering perfect bond with the matrix, which is [49]

$$\boldsymbol{\sigma}_{nt}(x) = E_{nt}\left[1 - \frac{\cosh\left(\beta\left(l_{nt} - 2x\right)\right)}{\cosh\left(\beta l_{nt}\right)}\right]\boldsymbol{\varepsilon}_m \tag{4.13}$$

$$\beta = \sqrt{\frac{2G_{iz}}{E_{nt}d_{nt}^2 \ln\left(1 + \frac{b}{r_{nt}}\right)}}, \tag{4.14}$$

where x represents the longitudinal positions in the reinforcement, and the subscripts "nt" and "iz" refers to the properties of nanotube and interface zone, respectively. E and G are the Young's modulus and the shear modulus, and b is the thickness material around of the CNTs associated with the interface zone.

Defining $l_{par} = l_{nt} - 2x$, its value can be obtained by finding the position "x" for which the effective modulus obtained from the integration of the tension distribution becomes

$$E_{eff} = \frac{l_{par}}{l_{nt}}E_{ntiz}^{par} + \left(1 - \frac{l_{par}}{l_{nt}}\right)E_{ntiz}^{ser}. \tag{4.15}$$

This procedure provides a value of the parallel length of

$$l_{par} = \frac{1}{\beta}\cosh^{-1}\left[\frac{1}{3}\cosh\left(\beta l_{nt}\right)\right]. \tag{4.16}$$

4.2.2 Definition of the volume fraction of the interface region

Based on the results reported in [8], the interface zone can be considered the region surrounding the carbon nanotube in which an amorphous matrix becomes crystalline. The volume fraction of the interface zone can be obtained as

$$\chi_c = \chi_o + k_{iz}, \tag{4.17}$$

where χ_c, χ_o are the volume fractions of crystalline matrix with and without CNTs, respectively. Assuming that the interface zone is a cylinder around the CNTs, it is possible to relate the volume fraction of the interface zone with the parameter $\frac{b}{r_{nt}}$ as

$$k_{iz} = \frac{N\left(\pi r^2 l_{nt} - \pi r_{nt}^2 l_{nt}\right)}{V} = \frac{N\pi r_{nt}^2 l_{nt}}{V}\left[\left(\frac{r}{r_{nt}}\right)^2 - 1\right] = k_{nt}\left[\left(\frac{r}{r_{nt}}\right)^2 - 1\right], \tag{4.18}$$

where V is the total composite volume, r is the radius of interface zone and N is the total number of nanotubes in the composite.

The relation between the radius of the nanotube and the interface is obtained replacing (4.18) in (4.17) as

$$\frac{r}{r_{nt}} = +\sqrt{\frac{(\chi_c - \chi_o)}{k_{nt}} + 1} \quad , \quad \chi_c \geq \chi_o, \tag{4.19}$$

and therefore

$$\frac{r}{r_{nt}} = 1 + \frac{b}{r_{nt}} \quad \Rightarrow \quad \frac{b}{r_{nt}} = +\sqrt{\frac{k_{iz}}{k_{nt}} + 1} - 1 \quad , \quad k_{iz} \geq 0. \tag{4.20}$$

4.2.3 Equivalent properties for MWCNTs

MWCNTs consist of concentric SWCNTs joined together with relatively weak van der Waals forces. For this reason, the capacity to transfer the load from the external wall to the internal walls is low. Some papers [121, 136] propose to simulate the CNTs like a solid cylinder with same exterior diameter and length, but with effective properties. The effective properties are obtained assuming that the outer wall takes the total load. In this approach it is assumed that the properties of the outer wall correspond to those of a graphite sheet. The effective stiffness of the MWCNT is calculated by imposing that for a same applied force, the deformation must be the same

$$\bar{\boldsymbol{\varepsilon}}_{nt} = \boldsymbol{\varepsilon}_{nt} \quad \Rightarrow \quad \bar{E}_{nt} = \frac{A_{ow}}{\bar{A}_{nt}} E_g, \tag{4.21}$$

where $\bar{E}_{nt}$ and E_g are the Young's modulus of the effective solid nanotube and graphite sheet, respectively, and $\bar{A}_{nt}$ and A_{ow} are the areas of the effective solid nanotube and outer wall, respectively. Equation (4.21) can be also read as

$$\bar{E}_{nt} = \left[1 - \left(1 - \frac{2t}{d_{nt}}\right)^2\right] E_g \qquad , \qquad \frac{t}{d_{nt}} \leq 0.5, \tag{4.22}$$

being t the thickness of one wall in the MWCNT and d_{nt} is the external diameter of the MWCNT.

Using the same procedure it is possible to obtain the shear modulus of the solid cylinder, by forcing the same twist when applying the same torque (T).

$$\bar{\phi}_{nt} = \phi_{nt} \quad \Rightarrow \quad \frac{T l_{nt}}{\bar{G}_{nt} \bar{J}_{nt}} = \frac{T l_{nt}}{G_g J_{ow}} \quad \Rightarrow \quad \bar{G}_{nt} = \frac{J_{ow}}{\bar{J}_{nt}} G_g, \tag{4.23}$$

where $\bar{G}_{nt}$ and G_g are the shear modulus of the effective solid CNTs and graphite sheet, respectively, and $\bar{J}_{nt}$ and J_{ow} are the polar moment of inertia of the effective solid CNTs and outer wall, respectively. They are

$$\bar{J}_{nt} = \frac{\pi d_{nt}^4}{32} \quad , \quad J_{ow} = \frac{\pi \left(d_{nt}^4 - (d_{nt} - 2t)^4\right)}{32}. \tag{4.24}$$

Replacing the expressions given by (4.24) in (4.23), the equivalent shear modulus can be written as

$$\bar{G}_{nt} = \left[1 - \left(1 - \frac{2t}{d_{nt}}\right)^4\right] G_g. \tag{4.25}$$

Finally, it is necessary to obtain the new density of the effective solid CNTs, as the total weight of the MWCNTs can not change in the composite when they are considered a solid cylinder, then

$$\bar{\rho}_{nt} = \frac{A_{nt}}{\bar{A}_{nt}} \rho_g \quad \Rightarrow \quad \bar{\rho}_{nt} = \left[1 - \left(\frac{d_i}{d_{nt}}\right)^2\right] \rho_g, \tag{4.26}$$

being ρ_g the density of the graphite sheet ($\rho_g = 2.25\ [g\,cm^{-3}]$) and d_i the internal diameter of the MWCNTs.

The most common parameter used to define the amount of CNTs added to a composite is their weight fraction. However, the composite constitutive model developed requires knowing the volume fraction. The volume fraction of CNTs in the composite is the volume that occupies a solid cylinder with the same external diameter. This parameter can be calculated with the following expression [121] as

$$k_{nt} = \frac{w_{nt}}{w_{nt} + \frac{\bar{\rho_{nt}}}{\rho_m} - \frac{\bar{\rho_{nt}}}{\rho_m} w_{nt}}, \tag{4.27}$$

where w_{nt} is the weight fraction and ρ_m is the density of the matrix.

4.2.4 Material non-linearity of the proposed model

In the proposed model, the composite performance is obtained from the mechanical response of its constituent materials, and each component is simulated with its own constitutive law. Therefore, if a constituent (i.e. the interface) is simulated with a non-linear law, the whole composite will become non-linear. As it has been already explained, with the present model it is possible to use any non-linear formulation to simulate the component behavior, such as plasticity, damage, viscosity, etc.

Besides the non-linear performance provided by each constituent, the load transfer capacity of the interface region is also affected if the interface is damaged. This effect must be included in the formulation.

According to Figure 4.3, the load is transferred from the interface to the CNTs reinforcement at their ends. Interface damage is expected to occur at the ends of the reinforcement, where there is larger stress concentrations. Assuming that the damaged region is unable to transfer loads and that the length required to transfer loads must remain constant, interface damage ends up affecting the parallel length of the nanotube, which can be calculated as

$$l_{par} = l^o_{par}\,(1-d)\,. \tag{4.28}$$

Here, l^o_{par} is the initial length of the nanotube working in parallel and d is the interface damage inner variable.

The dependence of the parallel length on the interface material damage provides a non-linear response of the composite, even when matrix and the carbon nantotube reinforcement are in their linear range.

4.3 Numerical Implementation

The proposed composite constitutive model has been implemented in PLCd [103], a finite element code that works with 3D solid geometries. The algorithm developed is described in Figure 4.4. PLCd has already implemented the constitutive laws that will be used to predict the performance of the composite components (elasto-plastic, elasto-damage and elastic). The formulation proposed has been written so that the constitutive laws of the constituents are seen as "black boxes", following the recommendations of [71] and [106].

The FEM code enters into the new formulation with the prediction of the strain tensor of the composite material in the actual time step. Layers are assumed to have all the same strain; therefore the strain tensor of each layer is obtained rotating the composite strain to the direction in which the CNTs are oriented. In each layer, the strain of the matrix and the CNTs-interface are the same, as they work in parallel, (see (4.5)). Knowing the strains for matrix material it is possible to obtain its stresses straightforward. On the other hand, to obtain the stresses for the CNT-interface material, it is necessary to separate it in two regions. In the flow chart, it is shown in Figure 4.4, these two regions are represented as "Parallel Block" and "Serial Block". This division is performed based on the value of N^{par} (defined in (4.12)). This value depends on the damage evolution of the interface, as has been explained in section 4.2.4.

The Parallel Block corresponds to the central region, where the CNTs and the interface work in parallel behavior and, therefore, they have the same strains. In this region the stresses for each component are obtained from the strain tensor, using their constitutive equation. Finally, the stress tensor of the CNT-interface material in the "Parallel Block" at time $t+\Delta t$ is

$$[\sigma^{par}_{ntiz}]^{t+\Delta t} = \bar{k}_{nt}\,[\sigma^{par}_{nt}]^{t+\Delta t} + \bar{k}_{iz}\,[\sigma^{par}_{iz}]^{t+\Delta t}\,. \tag{4.29}$$

On the other hand, at the ends of the CNTs, the interface-CNTs material has a serial behavior and it is necessary an initial prediction of the CNT or of the interface strains, in order to integrate the local stress in both components. If this initial prediction is made on the interface, its strains can be computed as

$$\Delta\varepsilon^{ser}_{ntiz} = [\varepsilon^{ser}_{ntiz}]^{t+\Delta t} - [\varepsilon^{ser}_{ntiz}]^{t} \tag{4.30}$$

$$[\Delta\varepsilon^{ser}_{iz}]_o = [C^{ser}_{iz}]^{-1} : C^{ser}_{ntiz} : \Delta\varepsilon^{ser}_{ntiz} \tag{4.31}$$

$$[\varepsilon^{ser}_{iz}]^{t+\Delta t}_o = [\varepsilon^{ser}_{iz}]^{t} + [\Delta\varepsilon^{ser}_{iz}]_o\,. \tag{4.32}$$

And, the strain tensor of the interface in the iteration step n is used to calculate the strain tensor of the CNT as

$$\varepsilon^{ser}_{ntiz} = \bar{k}_{nt}\varepsilon^{ser}_{nt} + \bar{k}_{iz}\varepsilon^{ser}_{iz} \tag{4.33}$$

$$[\varepsilon_{nt}^{ser}]_n = \frac{1}{\bar{k}_{nt}} [\varepsilon_{ntiz}^{ser}] - \frac{\bar{k}_{iz}}{\bar{k}_{nt}} [\varepsilon_{iz}^{ser}]_n \,. \tag{4.34}$$

Once knowing the strain tensor of both component materials, the constitutive law of each one is used to calculate their stress tensor. Afterwards it is necessary to verify that the iso-stress condition is indeed fulfilled. Therefore

$$[\Delta\sigma^{ser}]_n = [\sigma_{iz}^{ser}]_n - [\sigma_{nt}^{ser}]_n \leq tolerance. \tag{4.35}$$

If the residual stress is greater than the tolerance, the prediction of the interface strain must be corrected. A Newton-Raphson scheme is adopted to do this correction. The method uses the Jacobian to update the unknown variable, in this case, the interface strain, then

$$\begin{aligned} J_n &= \frac{\partial[\Delta\sigma^{ser}]_n}{\partial\varepsilon_{iz}^{ser}}\bigg|_{\varepsilon_{iz}^{ser}=[\varepsilon_{iz}^{ser}]_n} = \frac{\partial[\sigma_{iz}^{ser}]_n}{\partial\varepsilon_{iz}^{ser}} - \frac{\partial[\sigma_{nt}^{ser}]_n}{\partial\varepsilon_{nt}^{ser}} : \frac{\partial\varepsilon_{nt}^{ser}}{\partial\varepsilon_{iz}^{ser}} \\ &= [C_{iz}^{ser}]_n - [C_{nt}^{ser}]_n \left(-\frac{\bar{k}_{iz}}{k_{nt}}\right), \end{aligned} \tag{4.36}$$

and, finally

$$J_n = [C_{iz}^{ser}]_n + [C_{nt}^{ser}]_n \left(\frac{\bar{k}_{iz}}{\bar{k}_{nt}}\right). \tag{4.37}$$

Therefore, the strain tensor of the interface for the next step n+1 is estimated as

$$[\varepsilon_{iz}^{ser}]_{n+1} = [\varepsilon_{iz}^{ser}]_n - J_n^{-1} : [\Delta\sigma^{ser}]_n \,. \tag{4.38}$$

This iterative process continues until the residual stress is smaller than the required tolerance.

The final stresses in the serial region "Serial Block" of the CNTs-interface are

$$[\sigma_{ntiz}^{ser}]^{t+\Delta t} = [\sigma_{nt}^{ser}]^{t+\Delta t} = [\sigma_{iz}^{ser}]^{t+\Delta t} \,. \tag{4.39}$$

And at the end, the final stress tensor for a specific layer is obtained as

$$\begin{aligned} [\sigma]^{t+\Delta t} &= k_m [\sigma_m]^{t+\Delta t} + \\ &+ (k_{nt} + k_{iz}) \left\{ [N^{par}]^{t+\Delta t} [\sigma_{ntiz}^{par}]^{t+\Delta t} + [1 - N^{par}]^{t+\Delta t} [\sigma_{ntiz}^{ser}]^{t+\Delta t} \right\}. \end{aligned} \tag{4.40}$$

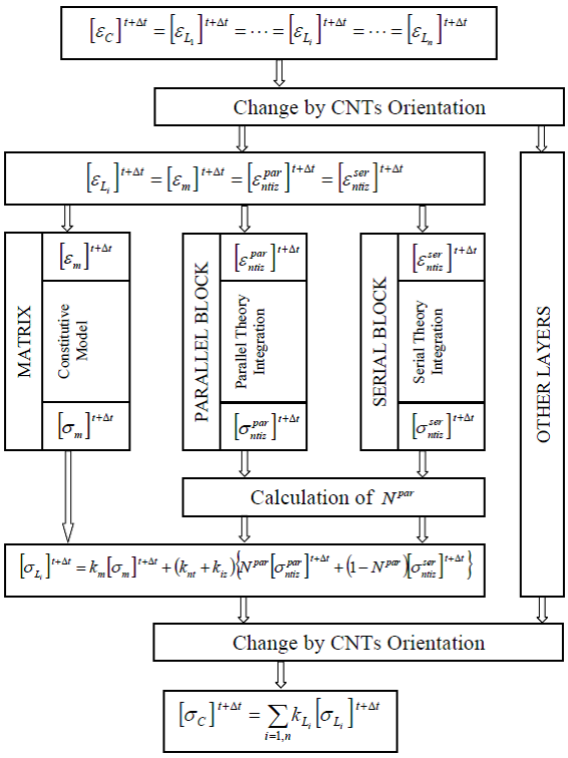

Figure 4.4: Flow chart of the proposed model in a FEM code.

Chapter 5

Validation and numerical results

In this chapter, the validation of the proposed constitutive model using data from the literature is presented. Then, a numerical example is shown using the model calibrated. The basic formulation of the different constitutive models used for the simple materials is showing in the Appendix A.

5.1 Validation of the elastic response

In the following section are compared the composite stiffness predicted by the composite constitutive model (see Section 4.2) with experimental data obtained from the literature. For this elastic properties validation the experimental data presented in the papers of Coleman et al. [16, 15] is used. In these works several composites made of the same matrix with different MWCNTs are experimental tested.

Materials description

In the following, it will present the mechanical properties of the material components used and the composites data.

Matrix component: The matrix material is polyvinyl alcohol (PVA) and its Young's modulus is given by the authors as $E_m = 1.9 \pm 0.3$ [GPa] [16].

Interface component: The authors found that the Young's modulus of the crystalline polymer phase is of $E_{iz} = 46$ [GPa]. On the other hand, the parameter $\frac{b}{r_{nt}}$ is estimated following the procedure described in Section 4.2.2.

MWNTs component: The nanotubes used in [16] are an arc grown MWCNT (Arc-MWCNT), two types of catalytic MWCNT from Nanocyl S.A. (CVD-1, CVD-2), a catalytic MWCNT produced in Orléans (France) (CVD-3), and a double walled nanotube (Dwnt). While in [15] the nanotube used is MWCNT from Nanocyl S.A. (MWCNT).

The maximum Young's modulus of the CNTs is ~ 1 [TPa][16], which corresponds to the stiffness of a perfect graphite sheet. The equivalent stiffness (see Section 4.2.3) of the nanotubes are calculated using this perfect stiffness value and considering a thickness of the outer layer of $t = 0.34$ [nm][48, 121].

The most important collected data of the nanotubes used are presented in table 5.1:

Type	d_{nt} (nm)	l_{nt} (µm)	l_{nt}/d_{nt}	b/r_{nt}	E_{nt} (GPa)	N^{par}
Arc-MWCNT	24	1	42	0.81	56	0.97
CVD-3	16	3.8	238	1.47	83	0.99
CVD-2	14	2.1	150	2.27	95	0.99
CVD-1	15	1.8	120	2.83	89	0.98
Dwnt	2.5	2.2	880	4.87	470	0.99
MWCNT	15	1.72	115	3.30	89	0.98

Table 5.1: Relevant data of the nanotubes used by Coleman el al. [16, 15].

Composites: A parameter missing in table 5.1 is the direction distributions of the CNT. In general, obtaining this information from the composite is very complicated. To outstep this impediment it is possible to rewrite equation given by (4.11) for one layer as

$$\mathbf{C}_{layer} = k_m \mathbf{C}_m + k_{ntiz} \mathbf{C}^{eff}_{ntiz}, \tag{5.1}$$

where

$$k_{ntiz} = k_{nt} + k_{iz} \qquad \mathbf{C}^{eff}_{ntiz} = N^{par} \mathbf{C}^{par}_{ntiz} + (1 - N^{par})\, \mathbf{C}^{ser}_{ntiz}. \tag{5.2}$$

Cox [20] and Krenchel [56] modified the rule of mixtures proposing the following equation to calculate the composite Young's modulus

$$E = k_m E_m + k_f \eta_o E_{eff}, \tag{5.3}$$

where E_m and E_{eff}, are the Young's modulus of the matrix and effective reinforcement, respectively. The volume fraction for each component is k and η_o is a fiber orientation efficiency factor. For the present validation (5.3) will be modified, adapting it to the developed formulation. Therefore

$$C_{composite} = k_m C_m + k_{ntiz} \eta_o C^{eff}_{ntiz}. \tag{5.4}$$

The value of the efficiency factor related to fiber orientation was taken from literature. In composites with a random distribution, $\eta_o = 0.38$.

Results

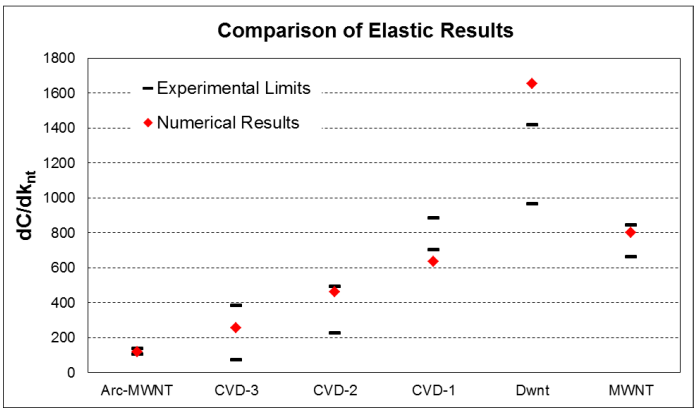

Figure 5.1: Comparison of numerical and experimental results [16, 15].

Figure 5.1 shows the values of dC/dk_{nt}, this is: the slope of the curves of Young's modulus (C) divided by volume fractions of nanotubes (k_{nt}), for the different composites considered. In the figure the short lines represent the limits of the range experimental results presented in [16, 15] and the red points correspond to the numerical result for each CNT type, obtained with the proposed composite model.

This figure shows that the formulation is capable of predicting the elastic stiffness of the composite, as most of the values obtained are comprehended between the limits defined by the experimental tests. There is only one case in which the value obtained exceed the limits of the experimental test. This is because the effective Young's modulus of the Dwnt is highest since its diameter is really low.

5.2 Validation of the non-linear performance

The non-linear behavior of the composite constitutive model has been validated comparing the results provided by the model with the experimental data obtained from the paper of Meng et al. [79]. In that article the matrix used is Polyamide 6 (PA6) and all composites contained a 1 wt% of MWCNTs reinforcement.

The MWCNTs used in the experimental tests were purchased from Chengdu Organic Chemistry Co. Ltd. Two different composites where manufactured with these nanotubes. One of them contains the

nanotubes "as is", without any previous treatments. These nanotubes are called U-MWCNT. The other composite uses nanotubes that where treated with a mixture of concentrated sulfuric and nitric acids. These are called A-MWCNT.

Materials description

In the following, it will present the properties of the material components used and the information of the composites.

Matrix component: The matrix material is characterized with an isotropic, elasto-plastic model using a Von-Mises yield criterion. The mechanical parameters of the model were calibrated using the experimental data described in [79], obtaining a Young's modulus of $E_m = 2.67$ [GPa], a Poisson ratio of $\nu_m = 0.4$ and an elastic threshold of 35 [MPa]. The parameters used to simulate matrix material are validated comparing the stress-strain graph obtained with the numerical model with the experimental one. This comparison is shown in Figure 5.2.

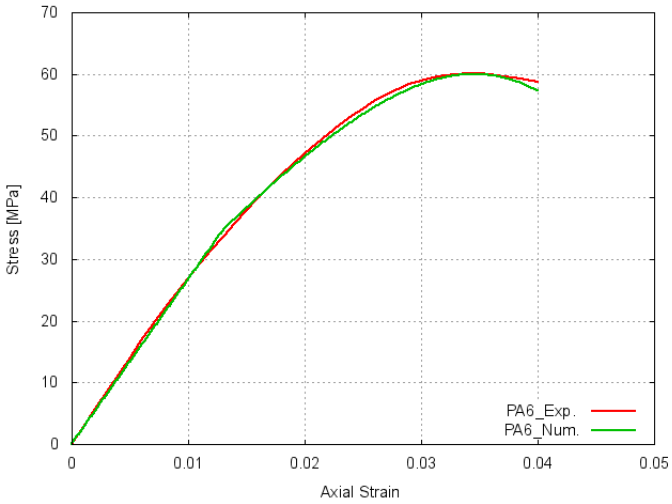

Figure 5.2: PA6 stress-strain relations for static tests [79].

Interface component: The interface zone is associated with the crystalline matrix around of MWCNTs. The properties of this material are better than those of the amorphous matrix. The volume fraction of the interface zone has been estimated with the data presented in the paper of Meng [79] and the equations developed in Section 4.2.2. On the other hand, the mechanical properties of the interface are used to calibrate the model. In current simulation, the interface has been defined with a isotropic, elasto-damage model with linear softening and Tresca yield surface. The mechanical parameters used are $E_{iz} = 5$ [GPa], $\nu_{iz} = 0.4$ and $G_{iz} = 1.8$ [GPa]. Damage in the interface starts for a stress threshold of 120 [MPa]. This value is in the range of theoretical and experimental tests value obtained in [124].

MWCNTs component: Numerical simulations of molecular structural mechanics of CNTs show that the Young's moduli are in the range of 1.05 ± 0.05 [TPa] and the shear moduli is about 0.4 ± 0.05 [TPa] [61]. It has been also shown that these values do not change significantly for CNTs with two, tree or four walls.

Regarding the transverse modulus of CNTs, it has been assessed from numerical and experimental results that there is an inverse relationship between axial and transverse modulus for carbon fibers [75]. Higher axial stiffness is associated to a longer and more aligned crystalline structure of the nanotube in this direction, which reduces properties in the transverse direction. Following this approach, in current simulation the transverse moduli of the MWCNTs are defined with the same values of the interface component.

Therefore, the equivalent properties of the MWCNTs were obtained using the equations described in section 4.2.3. The diameter of MWCNT is $d_{nt} = 50$ [nm]. The measurement of several MWCNTs provided an estimation of the internal diameter of $d_i = 8.2$ [nm] [121]. The effective density of MWCNTs has a value of $\bar{\rho}_{nt} = 2.2\,[g\,cm^{-3}]$; and the volume fraction of MWCNTs in the composite is 0.51 %. The MWCNTs have been simulated using an elastic orthotropic material with the following properties:

$$E_{1nt} = \bar{E}_{nt} = 56 \text{ [GPa]} \ , \ E_{2nt} = E_{3nt} = E_{iz} = 5 \text{ [GPa]}$$

$$G_{12nt} = G_{13nt} = \bar{G}_{nt} = 41 \text{ [GPa]} \ , \ G_{23nt} = G_{iz} = 1.8 \text{ [GPa]}$$

$$\nu_{12nt} = \nu_{13nt} = \nu_{23nt} = \nu_{nt} = 0.2$$

$$\nu_{ij} = \frac{E_i}{E_j}\nu_{ji} \quad \Rightarrow \quad \nu_{21nt} = \nu_{31nt} = 0.018 \quad \nu_{32nt} = 0.2$$

Composite: The composites tested had a random distribution of the MWCNTs. This is simulated in the numerical model by dividing the composite in several layers, each one containing CNTs with a different orientation. Current simulation divides the composite in 10 layers and CNTs angles varying from 0° to 90°. Each layer has a volume fraction of 10 %. Table 5.2 shows the volume fractions of the three composite components in each layer. This table also shows some geometry information of the MWCNTs and the interface zone, as well as the initial value of N^{par}.

Composite	k_{nt}[%]	k_{iz}[%]	k_m[%]	l_{nt}/d_{nt}	b/r_{nt}	N^{par}
PA6/A-MWCNT	0.5	4.1	95.4	250	2.00	0.98
PA6/U-MWCNT	0.5	5.3	94.2	250	2.35	0.98

Table 5.2: Data of the composites.

Results

In Figure 5.3 are represented the numerical and experimental results obtained for the composite made with A-MWCNTs. This figure shows an initial reduction of the composite stiffness, result of matrix yielding. Afterwards damage begins in the interface zone and, consequently, the composite continues reducing its stiffness. Interface damage leads to a reduction of the parallel length (see (4.28)). When the interface is completely damaged, the whole CNT-interface material has a serial performance. At this stage stresses in the interface are zero, and so must be the stresses in the carbon nanotubes. Therefore, the final stiffness of the composite corresponds to a material with a volumetric participation of 95.4 % of PA6 matrix, and the rest of the material correspond to voids.

Figure 5.4 shows the results for the composite made with U-MWCNTs. This composite is the same than the previous one (made with A-MWCNTs), with the only difference that in this case the bond between U-MWCNTs and interface zone is weaker. To take into account this difference, the numerical model used for this composite is the same used for the previous one, varying the threshold at which damage starts in the interface. In current simulation this value is reduced to 70 [MPa].

This simulation provides a maximum stress in the composite lower than the value obtained for previous one, consequence of having a weaker interface. The simulation also shows some divergences between the numerical and the experimental values. Both graphs start to differ for a strain of 2.5 % and the maximum load reached by the numerical simulation is larger than in the experimental tests. However, it has to be noted that the experimental tests provide a maximum stress lower than having just plain matrix (see Figure 5.2). Therefore, the differences observed in Figure 5.4 may be justified.

5.3 Numerical application

This section presents the numerical simulation of a four points bending beam (see Figure 5.8), which is used to show the numerical performance of the proposed composite constitutive model. The composite used in the simulation is a reinforced matrix with MWCNTs and it has been proposed in the framework of M-RECT project. The matrix in the composite is a Polyether Ether Ketone (PEEK) thermoplastic polymer provided by Victrex® company. While the MWCNTs are the Nanocyl™NC7000 from Nanocyl S.A.

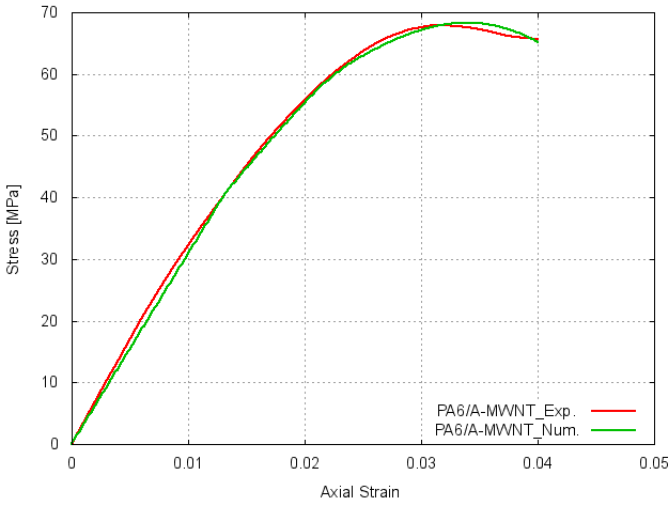

Figure 5.3: PA6/A-MWCNT stress-strain relations for static tests [79].

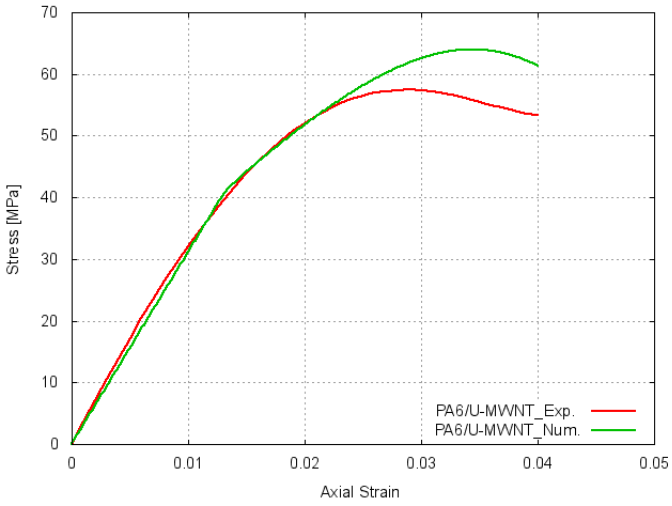

Figure 5.4: PA6/U-MWCNT stress-strain relations for static tests [79].

Two composite with different weight fractions percentage (0.5 and 2.0 wt%) of MWCNTs reinforcement will be analyzed.

Materials description

In the following, it will describe the properties and constitutive model of the material components and the composites information.

Matrix component: An elasto-plastic constitutive model with hardening is applied to characterize the behavior of the PEEK component. The matrix material has a Young's modulus of $E_m = 3.9$ [GPA], a shear modulus of $G_m = 1.9$ [GPA], a Poisson ratio of $v_m = 0.4$. These elastic mechanical properties are obtained from M-RECT project and of the information provided by Victrex® (http://www.victrex.com). The constitutive model is calibrated with an elastic threshold of 32 [MPa] and an ultimate tensile strength of 90 [MPa]. Figure 5.5 shows the comparison between the experimental data from the project and numerical results obtained with the constitutive model calibrated.

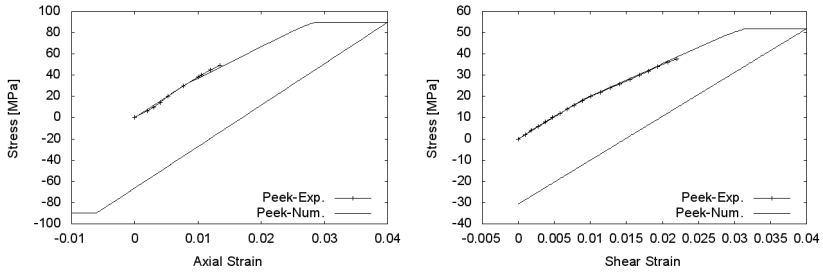

Figure 5.5: Comparison of the experimental data with the numerical results for PEEK.

Interface component: The constitutive model used to simulate the behavior of the crystalline PEEK around of the MWCNTs is an elasto-damage model with exponential softening. The mechanic properties of this interface zone are obtained following the same procedure used by Coleman et al. [16] but using the information presented in the works of Diez-Pascual et al. [24, 25], which use the PEEK material as matrix too. Then, the properties obtained are, a Young's modulus of $E_{iz} = 5.1$ [GPa], a shear modulus of $G_{iz} = 2.5$ [GPa] and a Poisson ratio of $v_{iz} = 0.4$. The value of the elastic threshold used in the model is of 28 [MPa]. This parameter is obtained when the composite constitutive model is calibrated to reproduce the experimental curve shown in Figure 5.6. This experimental data is for a PEEK reinforced with 3 wt% of MWCNTs obtained in the framework of the previous referred project.

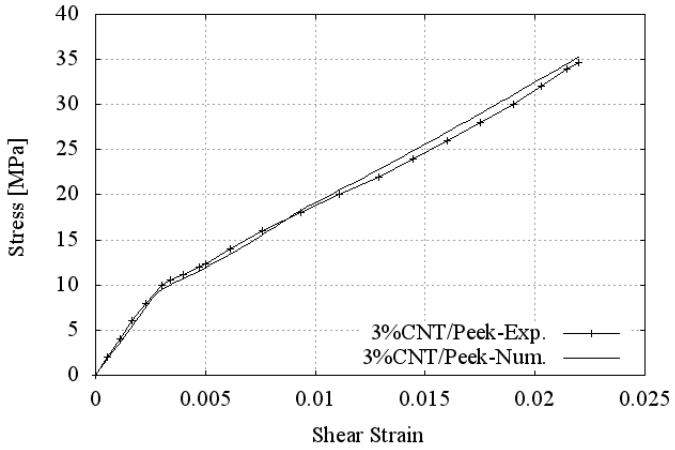

Figure 5.6: Experimental data and numerical response with the calibrated interface component model.

MWCNTs component: The geometric characteristics of the MWCNTs are obtained from the paper of Jiang et al. [50], who obtains as average diameter and length of 10.4 [nm] and 0.7 [μm], respectively. For the simulation the MWCNTs are considered as an orthotropic elastic material. The equivalent properties are obtained using the equations described in Section 4.2.3, assuming $E_g = 1.05 \pm 0.05$ [TPa] and $G_g = 0.4 \pm 0.05$ [TPa][61] and a thickness of the outer layer of $t = 0.34$ [nm][48, 121]. And taking the same consideration than before, the transverse properties are defined with the same values of the interface.

$$E_{1nt} = \bar{E}_{nt} = 131 \text{ [GPa]} \ , \ E_{2nt} = E_{3nt} = E_{iz} = 5.1 \text{ [GPa]}$$

$$G_{12nt} = G_{13nt} = \bar{G}_{nt} = 104 \text{ [GPa]} \ , \ G_{23nt} = G_{iz} = 2.5 \text{ [GPa]}$$

$$\nu_{12nt} = \nu_{13nt} = \nu_{23nt} = \nu_{nt} = 0.2$$

$$\nu_{ij} = \frac{E_i}{E_j}\nu_{ji} \quad \Rightarrow \quad \nu_{21nt} = \nu_{31nt} = 0.008 \quad \nu_{32nt} = 0.2$$

Composite	$k_m[\%]$	$k_{nt}[\%]$	$k_{iz}[\%]$
PEEK-0.5CNT	84.95	0.35	14.7
PEEK-2.0CNT	91.89	1.41	6.70

Table 5.3: Volume fractions in the composites.

Composites Table 5.3 shows the volume fractions of each component in the composites simulated.

The orientation distribution of the MWCNTs has been defined assuming that the composite is formed by several layers, each one with a specific angle and volume fraction of MWCNTs. The volume fractions of the MWCNTs for the different layer in the composite are shown in the Figure 5.7. The value of the volume fractions in the figure are relative values respect to the total volume fraction of the MWCNTs in the composite.

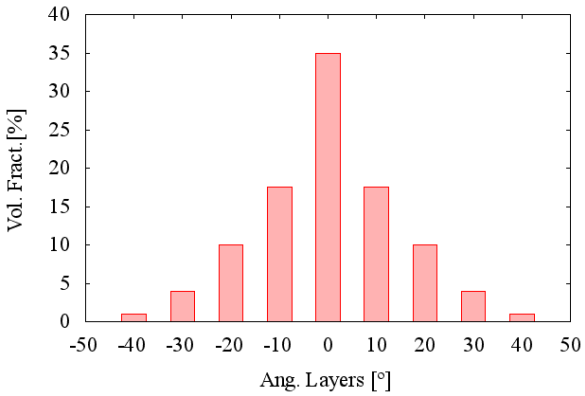

Figure 5.7: MWCNTs orientation distribution in the composite.

Geometry and FE model of the structure

The selected structure for the numerical simulations is a simple supported beam with two concentrated loads, which are applied at 1/3 of both beam ends.

Geometry Figure 5.8 shows the geometry and its dimensions, the boundary conditions and the load position on the analyzed structure.

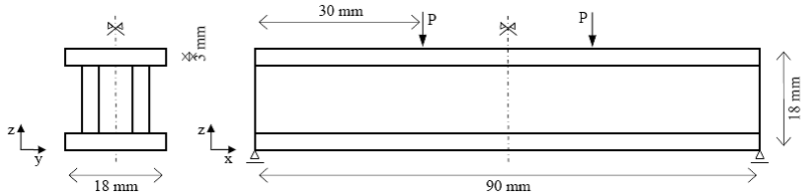

Figure 5.8: Geometry and extra information of the analyzed structure.

FE model The symmetry of the geometry, of the applied load and of the boundary conditions of the structure allows to reduce the numerical model in the simulation. For this case, the reduced FE model is a quarter of the real geometry of the structure. Figure 5.9 shows the numerical model and the FE mesh used for the numerical analysis. The more relevant data about the FE mesh is shown in the Table 5.4.

In order to obtain the real behavior of the structure with the reduced FE model it is necessary impose the restrictions on the numerical model given by the symmetry. There are two symmetry planes: The

Item	Nodes	Elements	Type Elem.	Order
Quantity/Type	1953	1200	Hexahedron	Quadratic

Table 5.4: Mesh information.

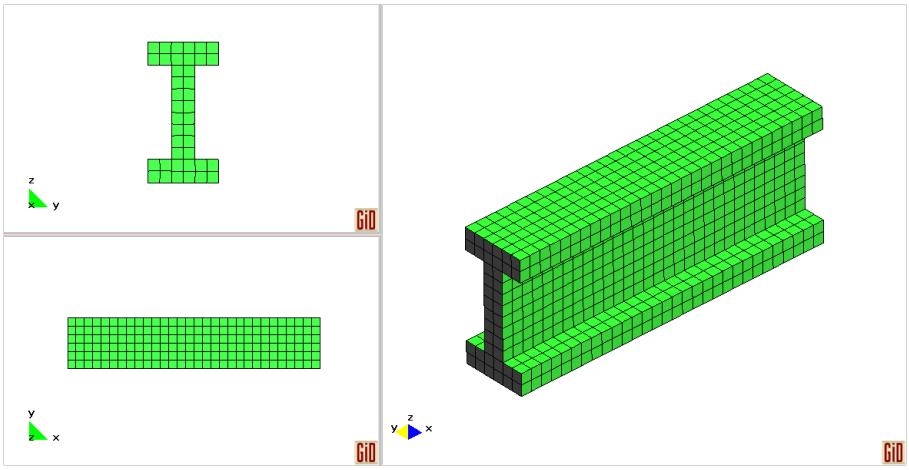

Figure 5.9: FE mesh used in the reduce model.

X-axis symmetry plane that has as normal axis the longitudinal axis (X-axis). In this symmetry plane, X direction displacements on the plane's nodes are restricted to zero. The other symmetry plane is the Y-axis symmetry plate, which has as normal axis the Y-axis in the model. For this symmetry plane, the null displacements restriction on the plane's nodes is Y direction. The longitudinal direction in the numerical model (X-axis) is taking as a reference direction for the definition of the layes' angle in the composite.

Results

Elastic results The numerical results obtained in the simulation are presented in comparative form, taking as reference the result obtained for the non-reinforced matrix (plain PEEK material).

In all cases, the applied load for elastic analysis is a fixed displacement of a -0.001 [mm] in Z direction at P position (see the Figure 5.8). The result considered for the comparison is the reaction force in Z direction on the support. As the imposed displacement is the same for all analysis, the reaction force increases when the material is the PEEK reinforced. Table 5.5 shows the results obtained for the different composites normalized by the non-reinforced PEEK results.

PEEK	PEEK-0.5%CNT	PEEK-2.0%CNT
1	1.20	1.52

Table 5.5: Normalized values obtained in the elastic simulation.

In the central section of the beam, between concentrated loads, there is a pure bending situation. While, at both ends of the beam there are a coupling bending and shear conditions. In Table 5.6, it is possible to observe the longitudinal (X direction) and shear (XZ direction) stresses obtained in the structure with the different composites.

Non-linear results In order to obtain the non-linear response of the structure the fixed displacement at P position is gradually increased in the simulation. Therefore, the reaction force in the support in Z direction increases too until the maximum value that the structure is able to take. The total force is four times the value obtained from the numerical model because the symmetry. The vertical (Z direction) displacement at the middle of the beam is taking as the reference loading increase.

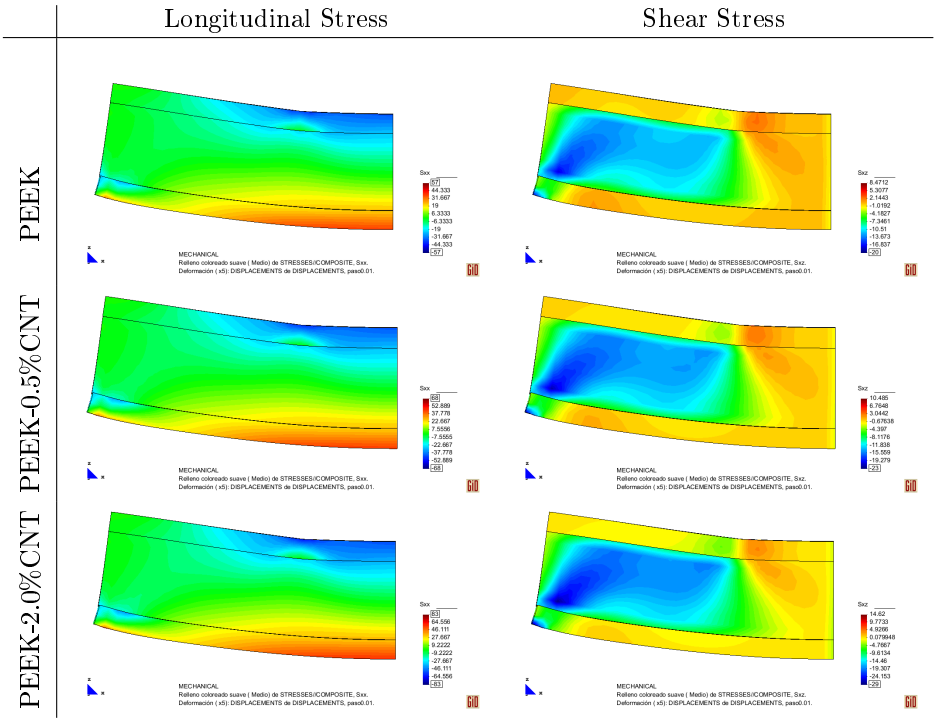

Table 5.6: Stress distribution for elastic results.

The fixed displacement is applied to the numerical model in 100 load steps of 0.1 [mm]. Figure 5.10 shows the results obtained in the simulation for the different composites. When the vertical displacement is around 1.5 [mm] the curves show the first loss of stiffness. This is because in the middle of the beam starts the plasticity in the PEEK. Then, when the vertical deformation is between 3 [mm] to 6 [mm] there is the second loss of stiffness. In this case, it is due to the damage in the interface zone. Subsequently, it is possible to observe that the model with non-reinforced PEEK has a higher stiffness than the ones with MWCNTs. This strange phenomenon is because at this point of the simulation the interface zone is completely damaged and, therefore, the contribution of the MWCNTs to the global stiffness is null. The stiffness obtained with the composites with MWCNTs are equivalent to the stiffness of a plain PEEK material but with some holes. This effect is clearly observed in Figure 5.11. This Figure shows the curves obtained for the simulation until a vertical displacement of 50 [mm].

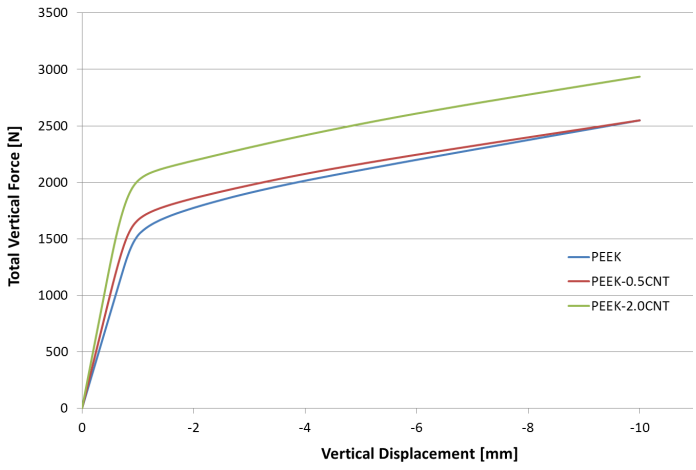

Figure 5.10: Structural response for PEEK-CNT.

Figure 5.11 shows a new loss of stiffness that takes place from 30 [mm] to 40 [mm] of vertical displace-

ment. This laster loss of stiffness is because the plasticity model in the PEEK arrives to the ultimate tensile strength in the middle zone of the beam.

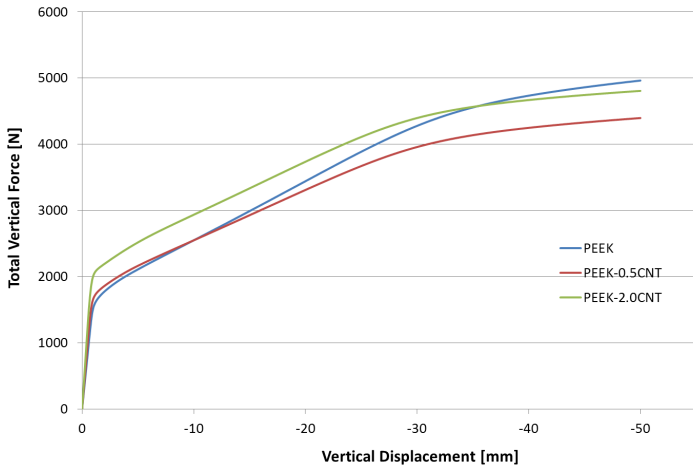

Figure 5.11: Structural response for PEEK-CNT up to 50 [mm] of vertical displacement.

Figure 5.12 shows the distribution of the longitudinal and shear stresses for the composite reinforced with MWCNTs. The longitudinal plastic strain and the equivalent stress for the composite are shown in Figure 5.13.

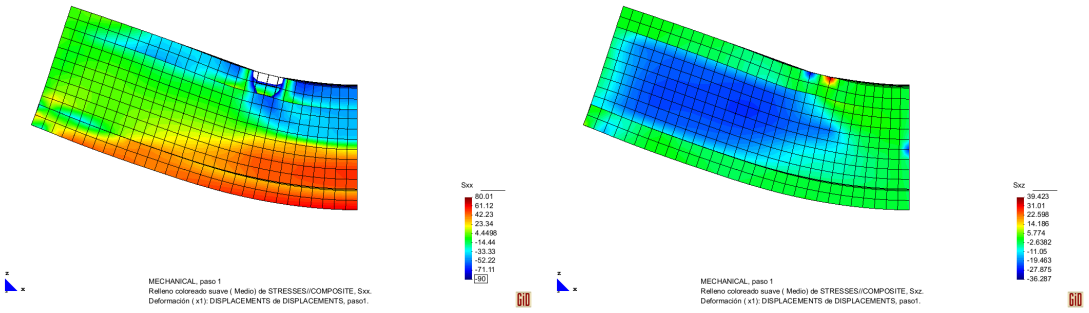

Figure 5.12: Longitudinal and shear stresses PEEK-CNT.

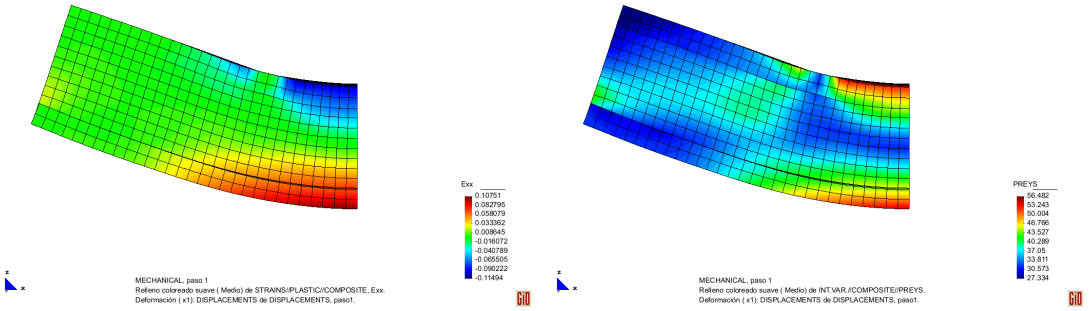

Figure 5.13: Longitudinal plastic strain and equivalent stress in the composite.

5.3.1 Visco-elastic analysis

In order to obtain a viscous response of the composite it is necessary to use a visco-elastic model to characterize its components. The visco-elastic model used for the matrix and the interface zone is the generalized Maxwell model. Figure 5.14 shows a scheme of the viscous model already implemented in the PLCd code. To conduct the visco-elastic analysis, the MWCNTs are considered to have a linear elastic behavior.

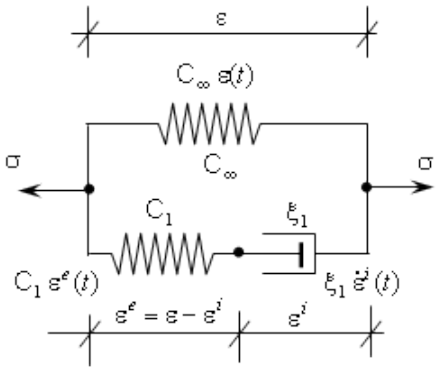

Figure 5.14: Generalized Maxwell model implemented.

The response obtained, after calibrating the model, is shown in Figure 5.15. This figure shows the stress-strain curve of a point inside of the structure in a complete load-unload cycle. The numerical simulation has been conducted using the two composites previously described (0.5% and 2.0% wt) and the plain PEEK. The Figure 5.15 shows that the area enclosed by the curve, in the load-unload cycle, in the composites reinforced with MWCNTs is larger than the non-reinforced matrix (plain PEEK). In other words, the dissipation capacity of a composite with MWCNTs is better than the matrix alone. The composite reinforced with 0.5% wt of MWCNTs has higher dissipative capacity than the other composite (2.0% wt). This is because, in this composite, the volume fraction of the interface zone is higher than in the other, as it is shown in Table 5.3. This phenomenon occurs because when the volume fraction of the MWCNTs in the composite is low, their distribution in the composite improves, and then, increasing the interface volume.

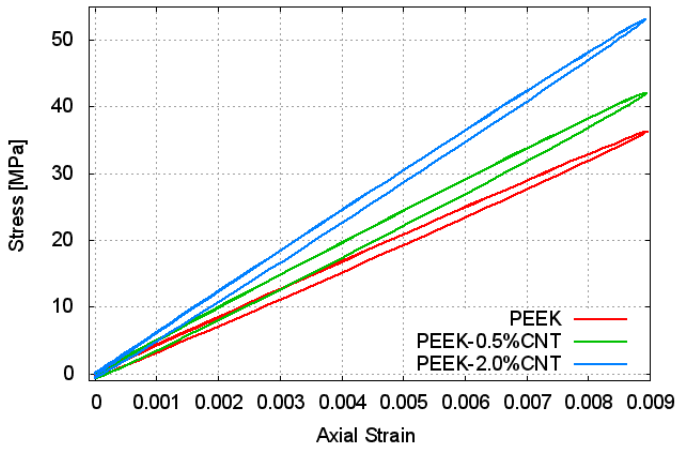

Figure 5.15: Structural response at 1 Hz.

5.4 Effect of the nanotube angle

The study of influence the angle of CNTs over the elastic properties has been done with information from the M-Rect project (see acknowledgements).

The composite used has a 3% weight of MWNT (1.94% volume, Baytubes® C 70 P). However, measurements made with X-rays show an apparent 5% weight. This difference is obtained because the nanotubes have a higher apparent diameter than the pristine one. Therefore, the b/rnt is calculated assuming that difference of 2% in weight is the result of having a coating polymer, or an interface, around the nanotubes. This interface represents approximately a 1.31% of the total composite volume. It is also necessary to know the mechanical properties of the interface zone. The Young's modulus of the interface zone is estimated with the same consideration made by Coleman et al. [16] using the data defined in the paper of Díez-Pascual et al. [24, 25]. This calculation provides a Young's modulus of 5 [GPa]. The poisson's ratio was taken equal to the Peek material and the shear modulus was estimated as Giz = (Eiz/Em).Gm, then Giz = 2.46 [GPa] and viz = 0.4.

The matrix used in the composite is PEEK; which Young's modulus and shear modulus were measured and had a value of 3.9 [GPa] and 1.9 [GPa], respectively. The nanotube is considered as an orthotropic material so its mechanical properties are different along the directions of each of the axes. The properties of the CNTs used to get the effective properties were Eg = 1 [TPa], Gg = 0.44 [TPa] (the shear modulus of graphite sheet) and its thickness t = 0.34[nm] [136]. The effective shear modulus of nanotubes is Gnt = [1- (1-2.t/dnt)4].Gg.

The model developed requires also some data of the nanotube geometry. The data used is shown in the Table 5.7.

Type	d_{nt} (nm)	l_{nt} (µm)	l_{nt}/d_{nt}	b/r_{nt}	$\bar{E}_{nt}$ (GPa)	$\bar{G}_{nt}$ (GPa)	N^{par}
MWCNT	13	1	77	0.3	105	85	0.97

Table 5.7: Project data for the implementation of the model

.

The final properties of the CNTs used in the model were:

Assuming that the transversal properties of nanotubes are the same that of interface zone:

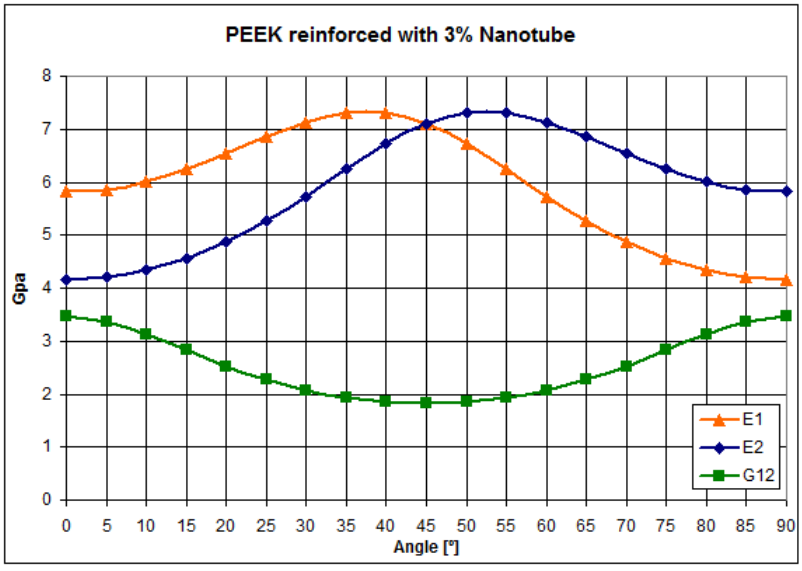

Figure 5.16: Elastic properties of PEEK reinforced with nanotubes

.

Figure 5.16 shows the change of elastic properties with the angle of the nanotubes, "E1" represent the Young's modulus in load direction; "E2" is the transversal Young's modulus and "G12" is the Shear modulus. The curves shown in the figure 5 are symmetrical respect to the line of 45°, but these are

different to the typical results for the reinforced matrices. In general the maximum value for the E1 is in 0^o. In this case, the E1 and E2 increase until 40^o, in return, the G12 decreases. This happening because the value of the Gnt is higher than the common estimate that it is used in fiber.

Chapter 6

Conclusions

A new composite constitutive model, based on the mixing theory, capable of predicting the mechanical performance of composites reinforced with carbon nanotubes has been presented. The formulation presented relates the reinforcement and the matrix in which they are embedded, using an interface material. This approach makes possible to consider non-linear phenomenons, such as debonding, by using non-linear constitutive laws to characterize the interface material. The formulation is written in a way in which all materials can be defined with their own constitutive law, improving the versatility of the model.

It has been shown that the elastic properties estimated with the model are in good agreement with experimental values obtained from literature. Only the numerical model of the composite made with the Dwnt reinforcement has given results in which the composite stiffness is overestimated. This is because the Dwnt has a very small diameter, which leads to a very high value of its equivalent Young's modulus.

The validation of the non-linear response provided by the proposed composite model has been performed using the experimental data of two different composites made with MWCNTs randomly distributed. The numerical curve obtained for the A-MWCNT is in good agreement with the experimental results. On the other hand, the numerical prediction obtained for the U-MWCNTs differs from the experimental results for strains larger than 2.5 %. However, it has to be said that the experimental results are lower than expected, as this composite is weaker than plain matrix.

Then, the formulation has used to predict and compare the mechanical properties of a straight beam subjected to four-point bending, with different material configurations. A non-linear analysis has also been made using the same structure and composites. The non-linear response of the beam obtained from the numerical simulation shows different points where there is a loss of structural stiffness. This structural behavior is obtained because the component materials in the composite reach their elastic thresholds and ultimate strength.

A visco-elastic material constitutive model is used for the polymeric matrix and the interface zone. The viscous response within the elastic range of the materials has been studied. The good capacity of energy dissipation in composites reinforced with MWCNTs has been proved with the simulations performed.

Part II

Multiscale homogenization

Chapter 1

Introduction

In the last decades, several formulations have been developed to mathematically characterize and model composites as heterogeneous materials. Large number of composite models have been proposed to assess the global behavior of these materials by fulfilling the thermodynamic laws in linear and non-linear range. Constitutive equations have been developed for composites with different arrangements such as materials with long and short fibers, nanofibers, fibers laminated with one or more directions, and even random reinforcement distributions, etc. However, these formulations are limited because the constitutive relationships were made on a particular composite material and in general, can not be extrapolated to other composites.

The homogenization methods analyze the composite materials from an internal structure point of view. Over the years, many techniques have been developed, among them: the effective medium approach [27], the self-consistent method [45], the variational boundary method which provides upper and lower limits of the total stiffness [42, 104] and the asymptotic homogenization method [6, 111]. Due to the complex task that is required to represent the microscopic mechanical behavior of composites makes that the homogenization approaches which use the RVE concept altogether with the stable computational methods to be very convenient in most of the cases, in comparison to the rest of procedures developed. In these procedures, the behavior of the whole composite is obtained by a micromechanical study of the material components and their interaction within of the composite's microstructure through an RVE model.

Within the context of the homogenization methods, the known multiscale techniques use the RVE concept to address the characterization of composites and structures. As a result, these multiscale procedures do not obtain a closed form for the general constitutive equations. The stress-strain relationship of the composite is obtained by performing a detailed modeling of the its microstructure at the micro-scale in the RVE model. Among the main advantages of these techniques it is found that: they do not require any composite constitute assumption at the macro-scale; they can use any constitutive law in the simple materials, even non-linear response and time-dependency; and they can employ many computational techniques to find the response at the micro-scale, such as, the FEM, the Voronoi cell method, or numerical methods based on the fast Fourier transforms, etc.

The first-order homogenization [117] is one of the most extended and popular multiscale method nowadays used. The approach uses the macro-scale deformation gradient tensor (or the strain tensor) to solve the micro-scale problem and then, by means of the microscopic results obtain the macro-scale stress tensor. The microscopic problem is solved through a Boundary Value Problem (BVP) on the RVE with particular boundary conditions, which are obtained using the macroscopic input. The resolution of the micro-scale BVP can be obtained through any mathematical or numerical approaches. After the solution of microstructural BVP, the microscopic displacement, deformation and stress fields are found and then, the macroscopic stress tensor is calculated as the volume average of the microscopic stress field. The BVP on the macro structure can be also approached through mathematical or numerical methods. When the solution of the couple macro-micro BVPs is faced by FEM at both scales the formulation/implementation is called FE^2 homogenization [116].

The advantages above described of the multiscale techniques become in a challenge when a non-linear analysis is made on a realistic three-dimensional structure using a FE^2 homogenization approach. In general, the spent computational cost is strongly expensive for non-linear simulations because for each integration point at the macro-scale one RVE is solved at each time step of the analysis. Further, from a energy point of view the method must be consistent and therefore, the conservation of the dissipated

energy through the scales should be guaranteed.

In the last decade, a second-order computational approach was proposed to be applied in critical regions of intense deformation, where the characteristic wave length of the macro-scale deformation field is of the order of the size of the micro-scale [55]. The homogenization technique has been developed as a natural extension of the first-order homogenization method. In the approach, the macroscopic gradient of the deformation gradient is also incorporated in the microscopic BVP and them, the stress tensor and a second-order stress tensor are retrieved. In the micro-scale level a first-order equilibrium problem is conserved but extra boundary condition in the BVP must be verified. However, a full second gradient continuum theory appears in the macro-scale level, which requires solving a higher-order equilibrium problem. The solution of the reformulated macroscopic BVP is made through a complex finite element implementation, which has restricted its massive application.

The use of a second-order approach for the non-linear analysis of structures has the advantage of including higher-order effects on the micro-scale. Nevertheless, the complex computational implementation to solve the macro-scale BVP restricts its application to realistic composite structures. From a mathematical and computational point of view the first-order approach is simpler than the second-order scheme. Then, it would be interesting to develop an enhanced-first-order approach which retains the easy computational implementation but with an enriched solution in the micro-scale.

1.1 Part's outline

In this second part of the present dissertation a multiscale homogenization model for composite structures is addressed. The proposed formulation can simulate the behavior of three-dimensional structures in non-linear range.

Following this objective, in Chapter 2 a review of the state of the art of the more relevant homogenization theories is shown. The asymptotic homogenization theory introduced the concept of two or more length scales, therefore it laid the foundations of what is today known as multiscale homogenization using RVE concept. At the end of the chapter a review of the most important multiscale approaches found in the literature is made.

Chapter 3 presents the formulation of the two-scale homogenization developed in this study. In the beginning, the first-order homogenization approach is described and then, using concepts of the second-order approach, a enhanced-first-order homogenization is proposed. The BVPs in both scales and their computational implementation through of an efficient three-dimensional FEM is also shown.

In Chapter 4 the results obtains with the first-order homogenization proposed are validated with other microscopic formulations. From the comparison can be observed that the multiscale formulation obtains a good characterization of the composite without any special consideration because the microstructure is modeled through of the RVE. The computational run times and memory used are also compared showing the advantage and drawback of the proposed implementation of the described first-order method.

Chapter 5 presents a novel strategy for the non-linear simulation of composite structures using multiscale homogenization approaches. The formulation is implemented in the FE code PLCd showing mesh independent at both scales as the develop approach conserves the energy through the scales.

Finally, in Chapter 6 the conclusions of the formulations presented in this part of the dissertation are in detail shown.

Chapter 2

State of the art

The modeling of heterogeneous composite materials have a high degree of complexity because the constitutive behavior of these is strongly dependent on micro-structural effects. The development of formulations based on multiple scales, able to predict the response of a heterogeneous material phenomenological according to information derived from a study at the micro-mechanical, is a natural choice to address the problem.

Numerous efforts have been made to mathematically model composite materials and structures using the homogenization method by using suitable multiscale techniques with relatively good approximation to the real global response of the composite. The most significant multiscale techniques, each of which, based in different theoretical principles, are:

2.1 The effective medium approximation

The method proposed originally by Eshelby [27] consists to find the current stresses in an elastic solid when a region of this (normally called "inclusion") suffered a change of shape and size which, if the surrounding material was absent, is represented by a uniform homogeneous deformation. By mean of the Eshelby solution a number of very important boundary value problems can be solved, like: *i*) the solution for an ellipsoidal inclusion embedded within an elastically mismatched matrix, *ii*) the solution for an ellipsoidal cavity in an elastic solid and *iii*) the solutions for circular and elliptical cracks in an elastic solid. Moreover, several theories which estimate the elastic properties of composite materials use the Eshelby solution. Further developments by Hashin [41], obtain expressions for the elastic moduli and their values bounds of many-phase heterogeneous materials using an approximate method based on the variational theorems of the elasticity theory and on a concentric-spheres model. Besides, Mori and Tanaka [87] develop a method of calculating the average internal stress in the matrix of a material containing inclusions with transformation strain. The obtained actual stress in the matrix is the average stress plus the locally fluctuating stress, the average of which vanishes in the matrix. The developed method also shows that the average stress in the matrix is uniform throughout the material and independent of the position of the domain where the average treatment is carried out.

2.2 The self-consistent method

It may be considered as an extension of the effective medium approximation. The method is proposed by Hill [45] and it uses similar concepts to the Hershey-Kröner theory of crystalline aggregates. The macroscopic elastic moduli of two-phase composites taking into account the inhomogeneity of stress and strain fields are estimated. It is required phases with the character of matrix and of effectively ellipsoidal inclusions, but they may have in any concentrations in the composite. The model of three phases or generalized self-consistent model given by Christensen and Lo [12] is a more elaborate version. The method embeds the spherical (or cylindrical fibers) in a cap (spherical or cylindrical) which represents the elastic properties of the matrix. Then, this set in turn is embedded in an infinite medium with the effective properties of the composite material to be determined. Finally, the effective elastic shear modulus of the material is obtained integrating the differential equations governing the behavior of the three-phase boundary conditions and of the applied loads.

A more recent work by Mercier and Molinari [81], which is based on the interaction law (postulated by Molinari [85] and validated by Mercier et al. [80] on the Eshelby problem) proposed two self-consistent schemes for perfectly disordered materials. The first one is valid for any non-linear behavior. And the second scheme is used to aggregates with phases having the same strain rate sensitivity. Both schemes predict accurately overall response of the composite material and they are able to capture the strain and stress histories of the components too.

2.3 Bounding methods

The bounding methods provide the lower and upper limits to the total stiffness of the system or of the composites. In general, these methods obtain a simpler expressions for the effective elastic properties through the minimum potential and complementary energies.

2.3.1 The classical bounds of Voigt and Reuss

The Voigt approach determine the elastic moduli by averaging stresses, expressed in terms of strains. The method assumes strain uniformity throughout the composite material. Therefore, the average strain of each phase is equal to the applied strain in the composite, which is similar to the rule of mixture assumption. Hence, considering that each component is linear-elastic, the following relationship can be obtained

$$\mathbf{C} = \sum_{i=1}^{n} \mathbf{C}_i \cdot \phi_i, \tag{2.1}$$

where $\mathbf{C}$ is the effective elastic tensor of the composite, $\mathbf{C}_i$ and ϕ_i are the elastic constitutive tensor and the volume fraction of the $i-th$ phase, respectively.

On the other hand, Reuss proposed to determine the elastic moduli by averaging strains, expressed in terms of stresses but assuming stress uniformity and then all components have the same stress. Therefore, the following estimation for the effective elastic tensor of the composite is obtained as

$$\mathbf{C} = \left[\sum_{i=1}^{n} \frac{\phi_i}{\mathbf{C}_i} \right]^{-1}. \tag{2.2}$$

The Voigt and Reuss methods give an upper and lower bounds for the elastic moduli of a composite with an arbitrary random microgeometry. The Voigt approach gives the upper bound of the elastic moduli for the compound material, while the Reuss approach gives the lower bound. These bounding methods depend only of the phase volume fractions, and of course of the elastic constitutive tensors of the components, but do not require any further information or assumption in respect of the microstructure. The expressions obtained for the bounding effective moduli are valid even for anisotropic component materials

2.3.2 The variational bounding method

The authors Hashin and Shtrikman [42] use the variational formulation to obtained the upper and lower bounds for the effective elastic moduli of quasi-isotropic and quasi-homogeneous multiphase materials of arbitrary phase geometry. The obtained bounds are close enough to provide a good estimate to the effective moduli when the ratios between the different phase moduli are not too large. The method obtains analytical expressions for the elastic constants of a heterogeneous material with a random isotropic distribution of phases. Later, Walpole [127, 128] generalized the bounding method of Hashin and Shtrikman for materials with several phases, which may be arbitrarily anisotropic.

A variational method for bounding the effective properties of nonlinear composite materials with isotropic components with full variational principle status was proposed by Ponte Castañeda [104]. The author proposed two dual versions of the new variational principle and it is demonstrated their equivalence to each other and to the classical variational principles. The approaches are used to determines bounds and estimates for the effective energy functions of nonlinear composites in the context of the deformation theory of plasticity. For completely anisotropic composites simpler forms of the classical bounds of Voigt and Reuss are recovered from the new variational principles. Also, for isotropic, particle-reinforced

composites, as well as for transversely isotropic, fiber-reinforced composites simpler forms for nonlinear Hashin-Shtrikman bounds are obtained.

Lahellec and Suquet [59] proposed a new method for determining the overall behavior of composite materials which can be composed by nonlinear inelastic components. The evolution equations describing the constitutive behavior of the components can be reduced to the minimization of an incremental energy function by using an implicit time-discretization scheme. The alternative minimization problem is rigorously equivalent to a nonlinear thermoelastic problem with a transformation strain which is a nonuniform field. Comparisons with full-field simulations show that the present model is good as long as the variational procedure is accurate in the purely dissipative setting, when elastic deformations are neglected. If this is the case, the model accounts in a very satisfactory manner for the coupling between reversible and irreversible effects and is therefore an accurate model for treating nonlinear viscoelastic and elasto-viscoplastic materials. Lahellec and Suquet [60] in a second part, of the described work, proposed a proper modification of the second-order procedure of Ponte Castañeda and leads to replacing, at each time-step, the actual nonlinear viscoelastic composite by a linear viscoelastic one. The linearized problem is even further simplified by using an effective internal variable in each individual component. The resulting predictions are in good agreement with exact results and improve the predictions of the previous work. The analytical models presented in the previous sections are reasonably able to predict equivalent material properties for relatively simple geometries and low volume fraction of the second component inclusions. But they are, in general, incapable to obtain the evolution of stresses and strains in the microstructure. Moreover, the actual heterogeneous materials cannot be treated with these models because normally these composites have an arbitrary microstructural morphology.

2.4 The asymptotic homogenization theory

This theory has proven to be a powerful technique for the analysis of structural arrangements in which two or more length scales naturally exist. Through the use of asymptotic expansions of displacement and stress fields and appropriate variational principles, the homogenization methods can provide not only the effective (homogenized) material parameters, but also distributions of stresses and strains at the two levels. Bensoussan et al. [6] proposed an asymptotica expansion of the solution in terms of a parameter ϵ, which is the ratio of the period of the structure to a typical length in the domain. The link from the microscopic to the macroscopic description of the behavior of the system is given by solving the problem in two scales defined by the spatial variables x and y, where x is a macroscopic quantity and $y = x/\epsilon$ is a microscopic quantity; y is associated with the small length scale of the inclusions or heterogeneities. The asymptotic problem is formulated in mathematical terms as a family of partial differential operators, depending on the small parameter ϵ. The operators may be time independent or time dependent, steady or of evolution type, linear or nonlinear, etc. The coefficients of the operators are periodic functions in all or in some variables with periods proportional to ϵ. Since ϵ is assumed to be small, it is has a family of operators with rapidly oscillation coefficients. The standard classical formulation of this theory is found in the work of Sanchez-Palencia [111, 112]. The two-scale process introduced in the partial differential equations of the problem produces equations in x, in y and in both variables. Normally, the equations in y are solvable if the microscopic structure is periodic, and this leads to deduction of the macroscopic equations for the global behavior in x. It is emphasized that the homogenized coefficients depend on the local structure of the medium. Fish et al. [28] presented a generalization of the mathematical homogenization method based on double-scale asymptotic expansion to account for damage effects in heterogeneous media. A closed-form expression relating local fields to the overall strain and damage is derived. Non-local damage theory is developed by introducing the concept of non-local phase fields (stress, strain, free energy density, damage release rate, etc.) in a manner analogous to that currently practiced in concrete. Numerical results of the model were found to be in good agreement with experimental data.

2.5 Homogenization using the RVE concept

The multiscale homogenization based on the use of a unit cell or RVE has emerged as one of the most promising methods to compute the response of composite structures. The unit cell is defined as a microscopic subregion that is representative of the entire microstructure in an average sense. The RVE is employed to obtain the effective properties for the homogenized material because it is assumed that it must contain a sufficient number of heterogeneities.

A thorough examination of the several representative volume element definitions found in the literature can be consulted in the review made by Gitman [33]. Moreover, Ostoja-Starzewki [99] points out that the RVE is very clearly defined in two situations only: *i)* unit cell in a periodic microstructure, as shown Figure 2.1a and *ii)* volume containing a very large (mathematically infinite) set of sub-scale elements, possessing statistically homogeneous and ergodic properties as shown Figure 2.1b.

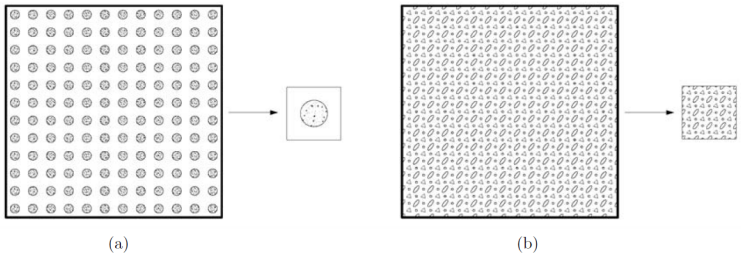

Figure 2.1: Representative volume element models: (a) unit cell approach; (b) statistical and ergodic approach [1].

On the other hand, Suquet [117] gives the basic principles of homogenization to obtain the constitutive equations for homogenized properties of a heterogeneous material. The process is resumed in the following three-step scheme and in Figure 2.2.

- Definition of a representative volume element. The size of this should be large enough to contain a sufficient number of micro heterogeneities of which the constitutive behaviour on these individual constituents is assumed to be known.
- Microscopic boundary conditions are obtained based on the macroscopic input variables (e.g. strain tensor), taking into account the geometry, constitutive laws, etc.
- Macroscopic output variables are obtained based on the solve of the microscopic behaviour of the RVE. Macroscopic properties of the equivalent homogeneous medium are evaluated.

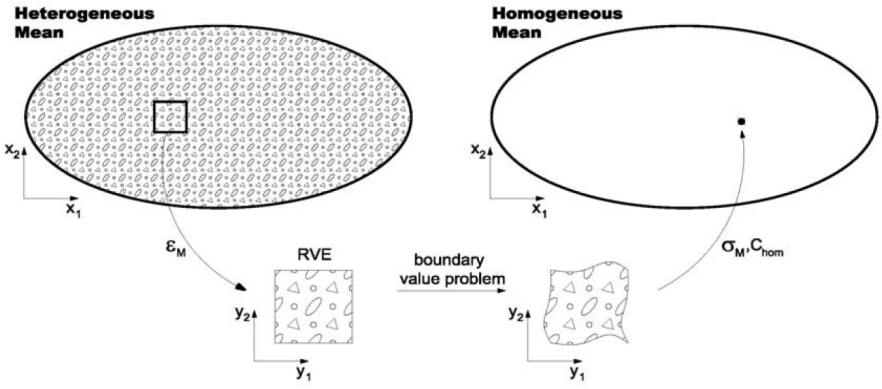

Figure 2.2: Representative homogenization scheme [1].

Renard and Marmonier [107] were the first to use a finite element discretization to model heterogeneous materials with multiscale approach. The method consists in solving two finite element problems, one for each scale. In the micro scale the geometry of the RVE is meshed and homogenization rules are used to link this with the macro scale problem.

Guedes and Kikuchi [36] studied the mechanical behavior of linear elastic 2D and 3D composite materials through the homogenization method. This study was one of the first that used homogenization in three dimensions. The method was implemented via a finite element technique to composite with a periodic microstructure. The implementation enabled the calculate of homogenized material mechanical

properties, these characterized the overall behavior of the composite, as well as the local one because it enables the computation of local stress and strain distribution within the microstructure of the composite. An adaptive finite element method was introduced in order to improve the accuracy of the numerical results. An error measure in suggested for the homogenized material constants, based on the a priori error estimations and the numerical implementation.

Swan [118] presented a computational stress and strain controlled homogenization methods for inelastic periodic composites within the framework of displacement finite element. The implementation of the stress controlled method employs a penalty formulation to insure that the displacement solution satisfies the linear-periodic descompositoin. The methods were assessed on a complete set of homogenization computations for an elasto-plastic composite, the strain-controlled method was easier to implement and was demonstrated that it has more computationally efficient than the other.

Later, Smit et al. [116] presented a homogenization method for large deformations and viscoelastic material behavior on microscopic and macroscopic level. The homogenization method was implemented in a multi-level two dimensional finite element program with meshes on macroscopic level (mesh of entire structure) and microscopic level (meshes of RVEs). The local macroscopic stress is obtained by appliying the local macroscopic deformation on a unique RVE through imposing appropriate boundary conditions and averaging the resulting stress field. To each macroscopic integration point a unique discretized RVE is assigned that provides the local macroscopic stress tensor and the tangential stiffness matric. A separate iterative finite element procedures on the RVE is used in each iteration cycle of each macroscopic increment. The following Figure 2.3 shows the proposed scheme by the authors.

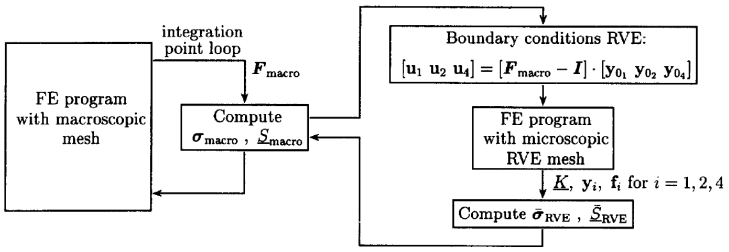

Figure 2.3: Schematic representation of a multi-level finite element program [116].

The computational cost was the main disadvantage of this implementation. The increase in computational time with respecto to a single-level analysis on the same macroscopic mesh was of 160 times for the structure analysed.

Michel et al. [82] presented a review of several problems which are specific of composites with periodic microstructure composed of linear or nonlinear constitutents. The study obtains the estimation of phenomenological macroscopic constitutive models through the analysis of a microscopic representative volume element proposing the concept of "macroscopic degrees of freedom". A general framework permitting either a strain or stress control was proposed. Different type of periodic conditions implementation was presented.

Terada et al. [120] presented a study for multiscale homogenization of the convergence of overall material properties when the unit cell size is increased. For general heterogeneous media that reveal irregular material distribution in a microscale, the study showed that the periodic boundary condition provides the most reasonable estimates among the class of possible boundary conditions for statistical homogeneous media. The work demostrated that it not strictly required the periodicity of RVE geometry in evaluating the effective properties. Moreover, at non-linear range the mechanical behaviors are more sensitive to the size of RVE than those of linear case. The authors concluded that the more accurate geometric modeling of the large RVE region enables the understanding of the acutal phenomena in the microscopic region as well as overall mechanical behaviors.

Haj-Ali and Muliana [38] proposed a three dimensional micromechanical modeling approach for the non-linear viscoelastic behavior of pultruded composites. A sublaminate model is used to provide for a nonlinear equivalent continuum of a layered medium. The system is idealized using a weighted-average response of two simplified micromodels with fiber and matrix. The proposed micromechanical framework was able generate the effective anisotropic non-linear viscoelastic response as a direct outcome of the micromechanical homogenization subcells. The same authors [39] extended the method to an inte-

grated micromechanical and structural framework for the non-linear viscoelastic analysis of laminated composite materials and structures. The micromechanical model is numerically implemented within a shell-based non-linear finite element by imposing a plane stress constraint on its 3D formulation. The micromechanical model provide the effective non-linear constitutive behavior for each Gauss point. The formulation was validated with several experimental creep test available in the literature. Finally, the work presents examples for non-linear viscoelastic structures, like laminated panel and a composite ring. In a latter work, Haj-Ali et al. [37] extend the above described method for the analysis of thick-section fiber reinforced plastic (FRP) composite materials and structures. The proposed modeling framework is applied to a pultruded composite system. Non-linear 3D micromechanical models representing the differente composite layers are used to generate through-thickness composite's effective responses. The nested non-linear micromechanical models are implemented at each integration point in the finite element structural analysis. The results obtained demostrated good prediction capabilities for effective properties and for multi-axial non-linear behavior of pultruded composites.

Matsui et al. [74] made a feasibility study and introduced a parallel algorithm to achieve the computational efficiency. The focus was to the inhomogeneous deformation of the overall structure, which may imply the loss of periodicity assumed in the initial state. The study presented an efficient algorithm for the deconcentration of computational loads by using a PC-cluster system. A simple numerical example for three dimensional heterogeneous structure was made. The authors concluded that the two-scale analysis is still expensive, even if a PC-cluster system for parallel computations is available at non-linear range.

Ladevèze et al. [58, 57] proposed a mixed, multilevel domain decomposition method or more accurately, as a "structure decomposition" method. The multiscale computational strategy consists of describing the structure as an assembly of simple components: substructures and interfaces. Each of these entities has its own variables and equations. The distinction between the micro and macro levels is made only at teh interfaces, where forces and displacements are split into macro contributions and micro complements. A substructure is subjected to the action of its environment (the neighboring interfaces) defined by the force and a velocity distribution on its boundary. An interface between two substructures transfers both the velocity and the force distributions.

Oller et al. [93] extended the work presented by Zalamea [135], two-scale numerical method by homogenization assuming the periodicity of the internal structure of the material, to addressing the problem of the steep gradient in the macroscopic field. To prevent the steep gradient in the macroscopic field variables that is produced by local boundary effects, the authors proposed a local refinement of the finite element mesh. The objective was to maintain the periodic condition on the boundaries of the cells near to the perturbation.

De Souza Neto and Feijòo [21] discussed some equivalence relationships for large strain multiscale solid constitutive models based on the volume averaging of the microscopic stress and deformation gradient fields over a representative volume element. The work established that the volume averaging of the first Piola-Kirchhoff stress over the reference configuration of an RVE is mechanically equivalent to the spatial averaging of Cauchy stress over the deformed RVE configuration. Whenever such conditions are met, multiscale constitutive models resulting from either the reference or spatial stress averaging are identical.

Kouznetsova and Geers proposed what is called second-order homogenization [54, 55], which is an extension of the first-order theory. In this case, the macroscopic deformation gradient tensor and its Lagrangian gradient is used to solve the boundary value problem at the microstructural scale. The second-order approach allows solve problems in the presence of localization phenomena without loss of precision in the solution because the Lagrangian tensor is taken into account. The main drawbacks of this method are its computational cost and complex implementation.

Geers, Coenen and Kouznetsova [31, 14] proposed a computational homogenization technique for thin-structured sheets based on the homogenization for first and second-order continua. The three dimensional heterogeneous sheet is represented by a homogenized shell continuum for which the constitutive response is obtained from the nested analysis of a microstructural representative volume element, incorporating the full thickness of the sheet and an in-plane representative cell of the macroscopic structure. At an in-plane integration point of the macroscopic shell, the generalized strains (the menbrane deformation and the curvature) are used to formulate the boundary conditions for the microscel RVE problem. All microstructural constituents are modeled at the RVE as an ordinary 3D continuum. Upon proper averaging of the RVE response, the macroscopic generalized stress and the moment resultants are obtained.

Chapter 3

Multiscale homogenization formulations

3.1 Introduction

3.2 General considerations

The no lineal transformation between the reference configuration of the body Ω and the current configuration of the same body Ω^c is defined as: $\boldsymbol{\phi}\colon \Omega \rightarrow \Omega^c \mid \mathbf{x} = \boldsymbol{\phi}(\mathbf{X})$, where $\mathbf{x} \in \Omega^c$ and $\mathbf{X} \in \Omega$ are respectively the current and the reference positions of the material point. Therefore, the linear mapping for an infinitesimal material line element is

$$d\mathbf{x} = \mathbf{F} \cdot d\mathbf{X}, \tag{3.1}$$

where the deformation gradient tensor is defined by

$$\mathbf{F} = \frac{\partial \boldsymbol{\phi}}{\partial \mathbf{X}} = \nabla \mathbf{x}. \tag{3.2}$$

Here, the gradient operator ∇ is taken respect to the reference configuration $\mathbf{X}$.

Nevertheless, if now a finite material line within a finite volume is consider, expression given by (3.1) does not apply any more. However, a Taylor series expansion (centered at $\mathbf{X}_o$) can be used to obtain an expression for the finite material line $\triangle\mathbf{x}$ in the current configuration as

$$\triangle\mathbf{x} = \mathbf{F}(\mathbf{X}_o) \cdot \triangle\mathbf{X} + \frac{1}{2}\mathbf{G}(\mathbf{X}_o) : \triangle\mathbf{X} \otimes \triangle\mathbf{X} + \mathcal{O}\left(\triangle\mathbf{X}_o^3\right), \tag{3.3}$$

where the gradient of the deformation gradient tensor is defined as

$$\mathbf{G} = \frac{\partial}{\partial \mathbf{X}}\left(\frac{\partial \boldsymbol{\phi}}{\partial \mathbf{X}}\right) = \nabla \mathbf{F}. \tag{3.4}$$

It can be shown that the third-order tensor $\mathbf{G}$ has the symmetry property $G_{ijk} = G_{ikj}$.

3.3 First-order homogenization approach

Considering a solid domain (or body Ω) with periodic or quasi-periodic microstructure which can be represented by a Represent Volume Element. In this body, besides it is possible to establish two scales level, one macro or structural scale level for the macrostructure and other micro or sub scale level for the microstructure. The microstructural scale level is defined using a RVE which characterizes the microstructure of the body. Moreover, considering now an infinitesimal material point $\mathbf{X}_o$ in the reference configuration of the structure and the RVE around this considered point as Figure 3.1 is showing.

The called principle of separation of scales [32] establishes that: the microstructural length scale l_μ is assumed to be much smaller than the macrostructural characteristic length l, which is the length over the macroscopic loading varies in space. In other words, the principle says that the existing periodical microscopic dimension around of the macrostructural point ($\mathbf{X}_o$) must to be smaller than the characteristic

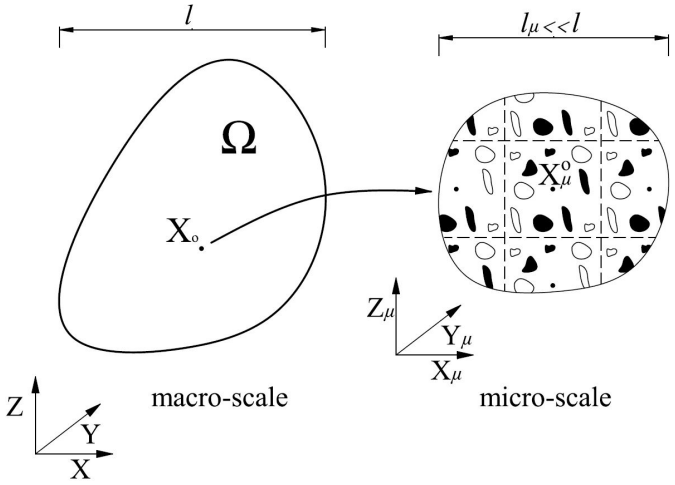

Figure 3.1: Macrostructure and microstructure around of the point $\mathbf{X}_o$.

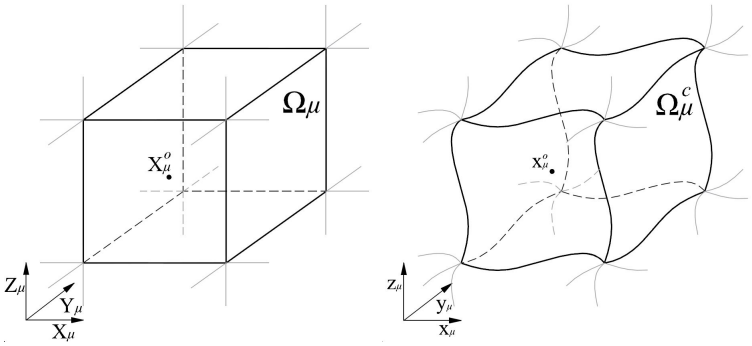

Figure 3.2: Reference and current configuration of the RVE.

macrostructural dimension. If this principle is satisfied, the current configuration or deformed position of a material point in the RVE $\mathbf{x}_\mu \in \Omega^c_\mu$ can be approximated as

$$\mathbf{x}_\mu(\mathbf{X}_o, \mathbf{X}_\mu) \cong \mathbf{x}^o_\mu + \mathbf{F}(\mathbf{X}_o) \cdot \triangle\mathbf{X}_\mu + \mathbf{w}(\mathbf{X}_\mu), \tag{3.5}$$

where $\triangle\mathbf{X}_\mu = \mathbf{X}_\mu - \mathbf{X}^o_\mu$, and $\mathbf{X}_\mu \in \Omega_\mu$ is the reference configuration or non-deformed position of the material point in the RVE and $\mathbf{X}^o_\mu$ and $\mathbf{x}^o_\mu$ are the origin of the reference and the current coordinate system on the RVE, respectively (see Figure 3.2). The extra term $\mathbf{w}$ is a microstructural displacement fluctuation field.

To simplify the symbolic manipulation of the formulation is convenient to set the coordinate system's origin as

$$\mathbf{X}^o_\mu = 0 \qquad \textit{and} \qquad \mathbf{x}^o_\mu = 0. \tag{3.6}$$

Later, it will be observed that taking these values the rigid body motion of the RVE will be avoided. Then, considering these restrictions (3.5) can be rewritten as

$$\mathbf{x}_\mu(\mathbf{X}_o, \mathbf{X}_\mu) \cong \mathbf{F}(\mathbf{X}_o) \cdot \mathbf{X}_\mu + \mathbf{w}(\mathbf{X}_\mu). \tag{3.7}$$

3.3.1 Displacement field on the RVE

The displacement field $\mathbf{u}_\mu$ at the RVE is defined by

$$\mathbf{u}_\mu = \mathbf{x}_\mu - \mathbf{X}_\mu, \tag{3.8}$$

and taking into account (3.7) in the previous equation

$$\mathbf{u}_\mu\left(\mathbf{X}_o,\mathbf{X}_\mu\right)\cong\left[\mathbf{F}\left(\mathbf{X}_o\right)-\mathbf{I}\right]\cdot\mathbf{X}_\mu+\mathbf{w}\left(\mathbf{X}_\mu\right), \tag{3.9}$$

where $\mathbf{I}$ is the second-order unit tensor.

3.3.2 Kinematically admissible displacement fields and boundary conditions in the RVE

The displacement fields in the RVE kinematically admissible are obtained as a result of the coupling between the macrostructure and the microstructure. This linkage is based on the average theorems and they have been initially proposed for infinitesimal deformations by Hill [44]. Later, Hill [46] and Nemat-Nasser [89] extended these to finite deformations.

The first of the averaging relations postulated that the volume average of the microstructural deformation gradient tensor $\mathbf{F}_\mu$ over the RVE must to be equal to the macroscopic deformation gradient tensor $\mathbf{F}$. In the considered point $\mathbf{X}_o$ this is

$$\mathbf{F}\left(\mathbf{X}_o\right)=\frac{1}{V_\mu}\int_{\Omega_\mu}\mathbf{F}_\mu\left(\mathbf{X}_o,\mathbf{X}_\mu\right)dV, \tag{3.10}$$

where V_μ is the volume of the RVE in the reference configuration.

Considering (3.7) it is possible to obtain the deformation gradient tensor in the microstructural scale as

$$\mathbf{F}_\mu\left(\mathbf{X}_o,\mathbf{X}_\mu\right)=\nabla\mathbf{x}_\mu\left(\mathbf{X}_o,\mathbf{X}_\mu\right)\cong\mathbf{F}\left(\mathbf{X}_o\right)+\nabla\mathbf{w}\left(\mathbf{X}_\mu\right), \tag{3.11}$$

and using this relation, the right hand size of (3.10) is

$$\begin{aligned}\frac{1}{V_\mu}\int_{\Omega_\mu}\mathbf{F}_\mu\left(\mathbf{X}_o,\mathbf{X}_\mu\right)dV &= \frac{1}{V_\mu}\int_{\Omega_\mu}\nabla\mathbf{x}_\mu\left(\mathbf{X}_o,\mathbf{X}_\mu\right)dV,\\ &= \mathbf{F}\left(\mathbf{X}_o\right)+\frac{1}{V_\mu}\int_{\Omega_\mu}\nabla\mathbf{w}\left(\mathbf{X}_\mu\right)dV.\end{aligned} \tag{3.12}$$

Equation (3.12) can be rewritten as

$$\mathbf{F}\left(\mathbf{X}_o\right)=\frac{1}{V_\mu}\int_{\Omega_\mu}\mathbf{F}_\mu\left(\mathbf{X}_o,\mathbf{X}_\mu\right)dV-\frac{1}{V_\mu}\int_{\Omega_\mu}\nabla\mathbf{w}\left(\mathbf{X}_\mu\right)dV, \tag{3.13}$$

or

$$\mathbf{F}\left(\mathbf{X}_o\right)=\frac{1}{V_\mu}\int_{\Omega_\mu}\nabla\mathbf{x}_\mu\left(\mathbf{X}_o,\mathbf{X}_\mu\right)dV-\frac{1}{V_\mu}\int_{\Omega_\mu}\nabla\mathbf{w}\left(\mathbf{X}_\mu\right)dV. \tag{3.14}$$

Finally, applying the divergence theorem, in the right hand size of (3.14), this can be also rewritten in term of surface integral as

$$\mathbf{F}\left(\mathbf{X}_o\right)=\frac{1}{V_\mu}\int_{\partial\Omega_\mu}\mathbf{x}_\mu\left(\mathbf{X}_o,\mathbf{X}_\mu\right)\otimes\mathbf{N}dA-\frac{1}{V_\mu}\int_{\partial\Omega_\mu}\mathbf{w}\left(\mathbf{X}_\mu\right)\otimes\mathbf{N}dA, \tag{3.15}$$

where $\partial\Omega_\mu$ is the RVE boundary domain in the reference configuration and $\mathbf{N}$ denotes the outward unit normal on $\partial\Omega_\mu$.

Clearly, to satisfy the first average theorem, the integrals that depend of the displacement fluctuation in both (3.14) and (3.15) must vanish. Therefore,

$$\int_{\Omega_\mu}\nabla\mathbf{w}\left(\mathbf{X}_\mu\right)dV=\mathbf{0} \tag{3.16}$$

and

$$\int_{\partial\Omega_\mu}\mathbf{w}\left(\mathbf{X}_\mu\right)\otimes\mathbf{N}dA=\mathbf{0}. \tag{3.17}$$

Noting Figure 3.2 and considering that the reference geometry configuration of the RVE is originally a cube, as figure is showing, the integral restriction on the RVE boundary can be splitted in the different surfaces of the $\partial\Omega_\mu$ domain. Besides, taking the reference coordinate system that is shown in Figure 3.3,

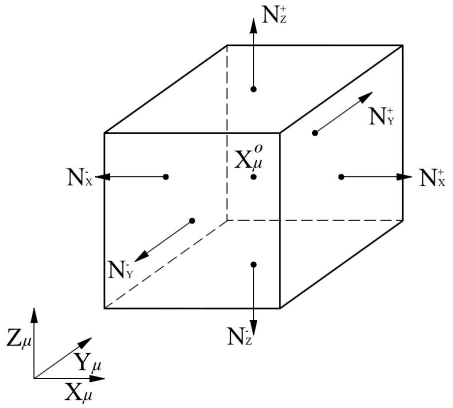

Figure 3.3: Normal vectors to the surfaces in the reference configuration of a Cubic RVE.

the outward unit normal of the cubic faces satisfy: $\mathbf{N}_X^- = -\mathbf{N}_X^+$, $\mathbf{N}_Y^- = -\mathbf{N}_Y^+$ and $\mathbf{N}_Z^- = -\mathbf{N}_Z^+$. Here, the subscript makes reference to the axis which is perpendicular to the considered face and the superscript defines the position of the face on the axis. Therefore, considering the geometry (3.17) may be rewritten as

$$\begin{aligned}
&\left(\int_{\mathbf{N}_X^+} \mathbf{w} dA_{yz} - \int_{\mathbf{N}_X^-} \mathbf{w} dA_{yz}\right) \otimes \mathbf{N}_X^+ \\
&+ \left(\int_{\mathbf{N}_Y^+} \mathbf{w} dA_{xz} - \int_{\mathbf{N}_Y^-} \mathbf{w} dA_{xz}\right) \otimes \mathbf{N}_Y^+ \\
&+ \left(\int_{\mathbf{N}_Z^+} \mathbf{w} dA_{xy} - \int_{\mathbf{N}_Z^-} \mathbf{w} dA_{xy}\right) \otimes \mathbf{N}_Z^+ = \mathbf{0}.
\end{aligned} \tag{3.18}$$

Since previous equation is possible to observe that the boundary restriction on the displacement fluctuation field can be splitted on each surface pair of the RVE boundary.

The previous equations since (3.16) to (3.18) can be used to obtain the different displacement fluctuation fields kinematically admissible in the microstructural level. They are

(i) *Taylor model* (or zero fluctuations): expression given by (3.16) is verified when

$$\mathbf{w},\ \text{sufficiently regular} \mid \mathbf{w}\left(\mathbf{X}_\mu\right) = \mathbf{0},\ \forall\, \mathbf{X}_\mu \in \Omega_\mu. \tag{3.19}$$

This model gives homogeneous deformation in the microstructural scale level (see (3.24)).

(ii) *Linear boundary displacements* (or zero boundary fluctuations): expression given by (3.17) is verified when

$$\mathbf{w},\ \text{sufficiently regular} \mid \mathbf{w}\left(\mathbf{X}_\mu\right) = \mathbf{0},\ \forall\, \mathbf{X}_\mu \in \partial\Omega_\mu. \tag{3.20}$$

The deformation of the RVE boundary domain for this class are fully prescribed.

(iii) *Periodic boundary fluctuations*:

The key kinematical constraint for this class is that the displacement fluctuation must be periodic on the different faces of the RVE. That is, for each pair $\left\{\mathbf{X}_\mu^+, \mathbf{X}_\mu^-\right\}$ of boundary points (3.18) is verified when

$$\mathbf{w},\ \text{sufficiently regular} \mid \mathbf{w}\left(\mathbf{X}_\mu^+\right) = \mathbf{w}\left(\mathbf{X}_\mu^-\right),\ \forall\, \textit{pairs}\ \left\{\mathbf{X}_\mu^+, \mathbf{X}_\mu^-\right\} \in \partial\Omega_\mu. \tag{3.21}$$

(iv) *Minimal constraint* (or uniform boundary traction):

In this constraint the nontrivial solution of (3.17) is obtained.

3.3.3 Microscopic and macroscopic strain tensor

Considering a infinitesimal deformation framework the strain tensor in the microstructural level can be obtained as

$$\begin{aligned}\mathbf{E}_\mu\left(\mathbf{X}_o,\mathbf{X}_\mu\right) &= \tfrac{1}{2}\left(\mathbf{F}_\mu\left(\mathbf{X}_o,\mathbf{X}_\mu\right)+\mathbf{F}_\mu^T\left(\mathbf{X}_o,\mathbf{X}_\mu\right)\right)-\mathbf{I}\\ &= \tfrac{1}{2}\left(\mathbf{F}\left(\mathbf{X}_o\right)+\mathbf{F}^T\left(\mathbf{X}_o\right)\right)-\mathbf{I}\\ &+ \tfrac{1}{2}\left(\nabla\mathbf{w}\left(\mathbf{X}_\mu\right)+\left(\nabla\mathbf{w}\left(\mathbf{X}_\mu\right)\right)^T\right),\end{aligned} \tag{3.22}$$

and, if (3.10) is satisfied it can be proved that taking the volume average of the microscopic strain tensor over the RVE domian the following relationship is obtained

$$\frac{1}{V_\mu}\int_{\Omega_\mu}\mathbf{E}_\mu\left(\mathbf{X}_o,\mathbf{X}_\mu\right)dV=\frac{1}{2}\left(\mathbf{F}\left(\mathbf{X}_o\right)+\mathbf{F}^T\left(\mathbf{X}_o\right)\right)-\mathbf{I}=\mathbf{E}\left(\mathbf{X}_o\right). \tag{3.23}$$

Here, $\mathbf{E}\left(\mathbf{X}_o\right)$ is the macroscopic strain tensor. Therefore, it is possible to rewrite (3.22) as

$$\mathbf{E}_\mu\left(\mathbf{X}_o,\mathbf{X}_\mu\right)=\mathbf{E}\left(\mathbf{X}_o\right)+\mathbf{E}_\mu^w\left(\mathbf{X}_\mu\right), \tag{3.24}$$

where $\mathbf{E}_\mu^w=\frac{1}{2}\left(\nabla\mathbf{w}+\left(\nabla\mathbf{w}\right)^T\right)=\nabla^s\mathbf{w}$ is the contribution of the displacement fluctuation field to the microscopic strain tensor and ∇^s is the symmetric gradient operator. Because (3.10) is verified the volume average of $\mathbf{E}_\mu^w$ over the RVE domain is equal zero.

3.3.4 Hill-Mandel principle and RVE equilibrium

The Hill-Mandel energy condition [45, 68], also referred to as the macro-homogeneity condition, states that the virtual work of the point $\mathbf{X}_o$ considered must be equal to the volume average of the virtual work in the RVE to any kinematically admissible displacement field, this principle can be formulated as

$$\mathbf{S}:\delta\mathbf{E}\left(\mathbf{X}_o\right)=\frac{1}{V_\mu}\int_{\Omega_\mu}\mathbf{S}_\mu:\delta\mathbf{E}_\mu dV, \tag{3.25}$$

where $\mathbf{S}$ and $\mathbf{S}_\mu$ are the macroscopic and microscopic stress tensor, respectively.

Using (3.24), the principle is rewritten as

$$\mathbf{S}:\delta\mathbf{E}\left(\mathbf{X}_o\right)=\frac{1}{V_\mu}\int_{\Omega_\mu}\mathbf{S}_\mu dV:\delta\mathbf{E}\left(\mathbf{X}_o\right)+\frac{1}{V_\mu}\int_{\Omega_\mu}\mathbf{S}_\mu:\delta\mathbf{E}_\mu^w\left(\mathbf{X}_\mu\right)dV. \tag{3.26}$$

Taking the macroscopic stress tensor $\mathbf{S}$ as the volume average of the microstructural stress tensor $\mathbf{S}_\mu$ in the RVE domain, which is similar to the first average relation (see (3.10))

$$\mathbf{S}\left(\mathbf{X}_o,\mathbf{X}_\mu\right)\equiv\frac{1}{V_\mu}\int_{\Omega_\mu}\mathbf{S}_\mu\left(\mathbf{X}_o,\mathbf{X}_\mu\right)dV, \tag{3.27}$$

equation (3.26) will be satisfy is

$$\int_{\Omega_\mu}\mathbf{S}_\mu:\delta\mathbf{E}_\mu^w\left(\mathbf{X}_\mu\right)dV=\int_{\Omega_\mu}\mathbf{S}_\mu:\nabla^s\delta\mathbf{w}dV=0, \tag{3.28}$$

Therefore, the RVE's variational equilibrium equation is

$$\int_{\Omega_\mu}\mathbf{S}_\mu:\nabla^s\delta\mathbf{w}dV=0, \tag{3.29}$$

which must be satisfied for any kinematically admissible displacement fluctuation field $\mathbf{w}$ (see Section 3.3.2).

It is possible to observe that because of the symmetry of the stress tensor $\mathbf{S}_\mu$ it can be proved that $\mathbf{S}_\mu:\left(\nabla\mathbf{a}\right)=\mathbf{S}_\mu:\left(\nabla\mathbf{a}\right)^T$, where $\mathbf{a}$ is a first order tensor, the (3.28) also can be rewritten as

$$\int_{\Omega_\mu}\mathbf{S}_\mu:\delta\mathbf{E}_\mu^w\left(\mathbf{X}_\mu\right)dV=\int_{\Omega_\mu}\mathbf{S}_\mu:\nabla\delta\mathbf{w}\left(\mathbf{X}_\mu\right)dV=0. \tag{3.30}$$

3.3.5 Microscopic and macroscopic stress tensor

The homogenized stress tensor in the macroscopic level is given by (3.27). Besides, taking into account the microscopic stress tensor which can be obtain as

$$\begin{aligned} \mathbf{S}_{\mu}\left(\mathbf{X}_{o},\mathbf{X}_{\mu}\right) &= \mathbf{C}_{\mu}\left(\mathbf{X}_{\mu}\right):\mathbf{E}_{\mu}\left(\mathbf{X}_{o},\mathbf{X}_{\mu}\right), \\ &= \mathbf{C}_{\mu}\left(\mathbf{X}_{\mu}\right):\mathbf{E}\left(\mathbf{X}_{o}\right)+\mathbf{C}_{\mu}\left(\mathbf{X}_{\mu}\right):\mathbf{E}_{\mu}^{w}\left(\mathbf{X}_{\mu}\right), \end{aligned} \tag{3.31}$$

where $\mathbf{C}_{\mu}$ is the material constitutive tensor in the RVE, the macro stress tensor is

$$\mathbf{S}\left(\mathbf{X}_{o},\mathbf{X}_{\mu}\right)=\bar{\mathbf{C}}:\mathbf{E}\left(\mathbf{X}_{o}\right)+\frac{1}{V_{\mu}}\int_{\Omega_{\mu}}\mathbf{C}_{\mu}:\mathbf{E}_{\mu}^{w}\left(\mathbf{X}_{\mu}\right)dV, \tag{3.32}$$

where

$$\bar{\mathbf{C}}\equiv\frac{1}{V_{\mu}}\int_{\Omega_{\mu}}\mathbf{C}_{\mu}dV \tag{3.33}$$

is a constitutive tensor which can be considered as a microsctructural material property.

Since (3.32) is possible to observe that the stress tensor $\mathbf{S}$ depends of the macroscopic strain tensor $\mathbf{E}$ and also, of the microscopic strain tensor $\mathbf{E}_{\mu}^{w}$, which is obtained with the displacement fluctuation field in the RVE. Moreover, the microscopic position vector $\mathbf{X}_{\mu}$ does not appear explicitly in the microstructural strain tensor (see (3.24)). Consequently, this variable does not appear in the microstructural stress tensor either. Then, the periodic microstructure around the point $\mathbf{X}_{o}$ is not necessary to be numerically modeled with its actual dimensions exactly. One non dimensional RVE containing internal distribution and volume fraction of the simple materials is only necessary to obtain the microscopic strain and stress fields. This is one of the principal advantage of this first-order homogenization respect to others multiscale high-order approaches.

On the other hand, it can be observed that the kinematically admissible displacement fluctuation option used to satisfy the boundary condition in the RVE problem affects the final macroscopic stress tensor obtained. For example, in the Taylor model case, which means null displacement fluctuation field in the total RVE domain, the stress tensor $\mathbf{S}$ obtained only depend of the strain tensor $\mathbf{E}$ and the constitutive tensor $\bar{\mathbf{C}}$. In other words, the Taylor model condition returns the classical mixing theory results.

3.4 Enhanced-first-order homogenization approach

The deformed position of a material point in the RVE given by (3.5), using in the first-order approach, can be improved if the second-order term of (3.3) is included. Then, it is possible to propose a new approximation of the current configuration of the RVE as

$$\mathbf{x}_{\mu}\left(\mathbf{X}_{o},\mathbf{X}_{\mu}\right)\cong\mathbf{x}_{\mu}^{c}+\mathbf{F}\left(\mathbf{X}_{o}\right)\cdot\triangle\mathbf{X}_{\mu}+\frac{1}{2}\mathbf{G}\left(\mathbf{X}_{o}\right):\triangle\mathbf{X}_{\mu}\otimes\triangle\mathbf{X}_{\mu}+\mathbf{w}\left(\mathbf{X}_{\mu}\right), \tag{3.34}$$

and setting the coordinate system's origin like (3.6) shows, the proposed deformed position of the RVE is

$$\mathbf{x}_{\mu}\left(\mathbf{X}_{o},\mathbf{X}_{\mu}\right)\cong\mathbf{F}\left(\mathbf{X}_{o}\right)\cdot\mathbf{X}_{\mu}+\frac{1}{2}\mathbf{G}\left(\mathbf{X}_{o}\right):\mathbf{X}_{\mu}\otimes\mathbf{X}_{\mu}+\mathbf{w}\left(\mathbf{X}_{\mu}\right). \tag{3.35}$$

Therefore, the proposed displacement field $\mathbf{u}_{\mu}$ on the RVE (see (3.8)) can be obtained now as

$$\mathbf{u}_{\mu}\left(\mathbf{X}_{o},\mathbf{X}_{\mu}\right)\cong\left[\mathbf{F}\left(\mathbf{X}_{o}\right)-\mathbf{I}\right]\cdot\mathbf{X}_{\mu}+\frac{1}{2}\mathbf{G}\left(\mathbf{X}_{o}\right):\mathbf{X}_{\mu}\otimes\mathbf{X}_{\mu}+\mathbf{w}\left(\mathbf{X}_{\mu}\right). \tag{3.36}$$

Noting that an extra term appears in the proposed microscopic displacement field by include the gradient of the deformation gradient tensor $\mathbf{G}$ in (3.34). This extra second-order term is a new linking term between the macroscopic and microscopic scales. The proposed displacement field in the RVE is enhanced because it reaches more information from the macro scale.

3.4.1 Kinematically admissible displacement fields and boundary conditions in the RVE

The first of the average postulates (see (3.10)) is used again to obtain the admissible displacement fields, the microscopic deformation gradient considering (3.35) is

$$\mathbf{F}_\mu\left(\mathbf{X}_o,\mathbf{X}_\mu\right)=\nabla\mathbf{x}_\mu\left(\mathbf{X}_o,\mathbf{X}_\mu\right)\cong\mathbf{F}\left(\mathbf{X}_o\right)+\mathbf{G}\left(\mathbf{X}_o\right)\cdot\mathbf{X}_\mu+\nabla\mathbf{w}\left(\mathbf{X}_\mu\right). \tag{3.37}$$

And, the volume average of this deformation gradient $\mathbf{F}_\mu$ over the RVE is

$$\begin{aligned}\frac{1}{V_\mu}\int_{\Omega_\mu}\mathbf{F}_\mu\left(\mathbf{X}_o,\mathbf{X}_\mu\right)dV &= \frac{1}{V_\mu}\int_{\Omega_\mu}\nabla\mathbf{x}_\mu\left(\mathbf{X}_o,\mathbf{X}_\mu\right)dV,\\ &= \mathbf{F}\left(\mathbf{X}_o\right)+\mathbf{G}\left(\mathbf{X}_o\right)\cdot\frac{1}{V_\mu}\int_{\Omega_\mu}\mathbf{X}_\mu dV\\ &+ \frac{1}{V_\mu}\int_{\Omega_\mu}\nabla\mathbf{w}\left(\mathbf{X}_\mu\right)dV.\end{aligned} \tag{3.38}$$

It can be shown that if the RVE geometry in the reference configuration is originally a cube, as Figure 3.2 is showing, plus taking the position of the coordinate system's origin on the RVE geometric center the first moment of volume of the RVE is

$$\int_{\Omega_\mu}\mathbf{X}_\mu dV=\mathbf{0}. \tag{3.39}$$

Therefore, (3.38) can be rewritten as

$$\mathbf{F}\left(\mathbf{X}_o\right)=\frac{1}{V_\mu}\int_{\Omega_\mu}\mathbf{F}_\mu\left(\mathbf{X}_o,\mathbf{X}_\mu\right)dV-\frac{1}{V_\mu}\int_{\Omega_\mu}\nabla\mathbf{w}\left(\mathbf{X}_\mu\right)dV, \tag{3.40}$$

or

$$\mathbf{F}\left(\mathbf{X}_o\right)=\frac{1}{V_\mu}\int_{\Omega_\mu}\nabla\mathbf{x}_\mu\left(\mathbf{X}_o,\mathbf{X}_\mu\right)-\frac{1}{V_\mu}\int_{\Omega_\mu}\nabla\mathbf{w}\left(\mathbf{X}_\mu\right)dV. \tag{3.41}$$

Rewriting the expression (3.41) in term of surface integrals applying the divergence theorem

$$\mathbf{F}\left(\mathbf{X}_o\right)=\frac{1}{V_\mu}\int_{\partial\Omega_\mu}\mathbf{x}_\mu\left(\mathbf{X}_o,\mathbf{X}_\mu\right)\otimes\mathbf{N}dA-\frac{1}{V_\mu}\int_{\partial\Omega_\mu}\mathbf{w}\left(\mathbf{X}_\mu\right)\otimes\mathbf{N}dA. \tag{3.42}$$

Equation (3.42) is exactly the same than the one obtained for the first-order approach (see (3.15)) then, it will be obtained the same restrictions on the displacement fluctuation field that showing (3.16)-(3.18) which satisfy its. Therefore, the different displacement fluctuation fields kinematically admissible presented in Section 3.3.2 are still valid for this enhanced first-order approach.

The next step now is obtained the kinematic restrictions due to include the new term $\mathbf{G}$ in the proposed microscopic displacement field $\mathbf{u}_\mu$. In other words, some extension of the first average theorem needs to be proposed in term of the gradient of the deformation gradient. The first natural possibility for this extension could be

$$\mathbf{G}\left(\mathbf{X}_o\right)=\frac{1}{V_\mu}\int_{\Omega_\mu}\mathbf{G}_\mu\left(\mathbf{X}_o,\mathbf{X}_\mu\right)dV. \tag{3.43}$$

Note that (3.43) is similar to (3.10) but in this case, the volume average of the microstructural gradient of the deformation gradient tensor $\mathbf{G}_\mu$ over the RVE must to be equal to the macroscopic gradient of the deformation gradient $\mathbf{G}$ in the considered point $\mathbf{X}_o$.

Considering (3.37) and (3.4) the gradient of the deformation gradient in the microstructural scale level is

$$\mathbf{G}_\mu\left(\mathbf{X}_o,\mathbf{X}_\mu\right)=\nabla\left(\nabla\mathbf{x}_\mu\left(\mathbf{X}_o,\mathbf{X}_\mu\right)\right)\cong\mathbf{G}\left(\mathbf{X}_o\right)+\nabla\left(\nabla\mathbf{w}\left(\mathbf{X}_\mu\right)\right). \tag{3.44}$$

Using (3.44) and taking the volume average over the RVE it is possible to obtain

$$\mathbf{G}\left(\mathbf{X}_o\right)=\frac{1}{V_\mu}\int_{\Omega_\mu}\mathbf{G}_\mu\left(\mathbf{X}_o,\mathbf{X}_\mu\right)dV-\frac{1}{V_\mu}\int_{\Omega_\mu}\nabla\left(\nabla\mathbf{w}\left(\mathbf{X}_\mu\right)\right)dV, \tag{3.45}$$

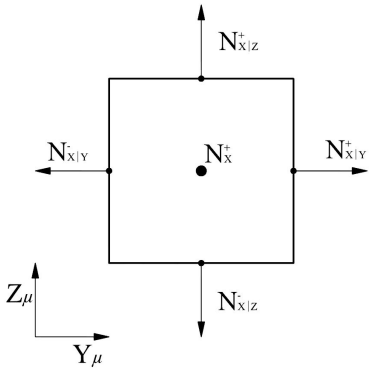

Figure 3.4: Normal vectors to the lines in the YZ surface of the Cubic RVE.

or

$$\mathbf{G}\left(\mathbf{X}_o\right) = \frac{1}{V_\mu}\int_{\Omega_\mu} \nabla\left(\nabla \mathbf{x}_\mu\left(\mathbf{X}_o, \mathbf{X}_\mu\right)\right) dV - \frac{1}{V_\mu}\int_{\Omega_\mu} \nabla\left(\nabla \mathbf{w}\left(\mathbf{X}_\mu\right)\right) dV. \tag{3.46}$$

And, applying the divergence theorem in the last expression

$$\mathbf{G}\left(\mathbf{X}_o\right) = \frac{1}{V_\mu}\int_{\partial\Omega_\mu} \nabla \mathbf{x}_\mu\left(\mathbf{X}_o, \mathbf{X}_\mu\right) \otimes \mathbf{N} dA - \frac{1}{V_\mu}\int_{\partial\Omega_\mu} \nabla \mathbf{w}\left(\mathbf{X}_\mu\right) \otimes \mathbf{N} dA. \tag{3.47}$$

How in the first-order approach, to satisfy the proposed extension of the first average theorem, the integrals that depend of the displacement fluctuation in (3.45) and (3.47) must vanish, then

$$\int_{\Omega_\mu} \nabla\left(\nabla \mathbf{w}\left(\mathbf{X}_\mu\right)\right) dV = \mathbf{0}, \tag{3.48}$$

and

$$\int_{\partial\Omega_\mu} \nabla \mathbf{w}\left(\mathbf{X}_\mu\right) \otimes \mathbf{N} dA = \mathbf{0}. \tag{3.49}$$

The last expressions represent a new extra integral restriction on the derivative displacement fluctuation field. Taking the same consideration than before about the geometry of the RVE (see Figure 3.3), the boundary integration in (3.49) can be splitted in

$$\begin{aligned}
&\left(\int_{\mathbf{N}^+_X} \nabla \mathbf{w} dA_{yz} - \int_{\mathbf{N}^-_X} \nabla \mathbf{w} dA_{yz}\right) \otimes \mathbf{N}^+_X \\
+&\left(\int_{\mathbf{N}^+_Y} \nabla \mathbf{w} dA_{xz} - \int_{\mathbf{N}^-_Y} \nabla \mathbf{w} dA_{xz}\right) \otimes \mathbf{N}^+_Y \\
+&\left(\int_{\mathbf{N}^+_Z} \nabla \mathbf{w} dA_{xy} - \int_{\mathbf{N}^-_Z} \nabla \mathbf{w} dA_{xy}\right) \otimes \mathbf{N}^+_Z = \mathbf{0}.
\end{aligned} \tag{3.50}$$

Some components into of the integrals can also be rewritten in terms of lines boundary integral applying the divergence theorem one more time. For example, if the first left integral in the first term in (3.50) is taken, the lines boundary of this surface integral can be separated in four different lines, two perpendiculars of Y axis, and others two perpendiculars of Z Axis as Figure 3.4 is showing. Because of the RVE geometry taken, these lines boundary have the property of $\mathbf{N}^-_{X|Y} = -\mathbf{N}^+_{X|Y}$ and $\mathbf{N}^-_{X|Z} = -\mathbf{N}^+_{X|Z}$.

Then, with this information the considered integral can be rewritten as

$$\begin{aligned}\int_{\mathbf{N}_X^+} \nabla \mathbf{w} dA_{yz} = & \int_{\mathbf{N}_X^+} \nabla_X \mathbf{w} dA_{yz} \\ & + \left(\int_{\mathbf{N}_{X|Y}^+} \mathbf{w} dL_z - \int_{\mathbf{N}_{X|Y}^-} \mathbf{w} dL_z \right) \otimes \mathbf{N}_{X|Y}^+ \\ & + \left(\int_{\mathbf{N}_{X|Z}^+} \mathbf{w} dL_y - \int_{\mathbf{N}_{X|Z}^-} \mathbf{w} dL_y \right) \otimes \mathbf{N}_{X|Z}^+,\end{aligned} \tag{3.51}$$

where ∇_X represent the derivative with respect to X axis, this component cannot be rewritten as lines integral using the divergence theorem. It can be show that when the *Periodic boundary fluctuations* condition is the kinematically admissible option used for the displacement fluctuation field on the RVE, the two right terms on (3.51) are satisfied directly. The points on the opposing lines are pair boundary points which have the same displacement fluctuation because the kinematic condition imposed. Applying the same procedure in the others integral terms in (3.50), this equation can be rewritten as

$$\begin{aligned}& \left(\int_{\mathbf{N}_X^+} \nabla_X \mathbf{w} dA_{yz} - \int_{\mathbf{N}_X^-} \nabla_X \mathbf{w} dA_{yz} \right) \otimes \mathbf{N}_X^+ \\ & + \left(\int_{\mathbf{N}_Y^+} \nabla_Y \mathbf{w} dA_{xz} - \int_{\mathbf{N}_Y^-} \nabla_Y \mathbf{w} dA_{xz} \right) \otimes \mathbf{N}_Y^+ \\ & + \left(\int_{\mathbf{N}_Z^+} \nabla_Z \mathbf{w} dA_{xy} - \int_{\mathbf{N}_Z^-} \nabla_Z \mathbf{w} dA_{xy} \right) \otimes \mathbf{N}_Z^+ = \mathbf{0}.\end{aligned} \tag{3.52}$$

The previous expression represents a extra restriction on the displacement fluctuation field kinematically admissible in the RVE and for example, one possible boundary conditions which satisfies its is

$$\begin{aligned}\int_{\mathbf{N}_X^+} \nabla_X \mathbf{w} dA_{yz} &= \int_{\mathbf{N}_X^-} \nabla_X \mathbf{w} dA_{yz}, \\ \int_{\mathbf{N}_Y^+} \nabla_Y \mathbf{w} dA_{xz} &= \int_{\mathbf{N}_Y^-} \nabla_Y \mathbf{w} dA_{xz}, \\ \int_{\mathbf{N}_Z^+} \nabla_Z \mathbf{w} dA_{xy} &= \int_{\mathbf{N}_Z^-} \nabla_Z \mathbf{w} dA_{xy}.\end{aligned} \tag{3.53}$$

Equation (3.52) is analogous to (3.18) but it is written in terms of derived displacement fluctuation field, in this case, on the normal direction of the pair surfaces (see Figure 3.3). Therefore, to satisfy any kinematic restriction, as for example (3.53) shows, obtained from (3.52) a high order problem on the microscopic level must to be considered because the restriction of the displacement fluctuation field is written on its derivate.

An alternative of the proposed extension of the averaging theorem given by (3.43) must be found to keep a classical boundary value problem on the microstrucural RVE problem. With this aim Kouznetsova [54] proposed other alternative extension of the first average theorem. The proposed condition imposes that the second moment of area of the deformed RVE given in terms of the microscopic displacements must be equal to the second moment of area of the RVE expressed in terms of macroscopic deformation variables [51]. Considering the above, (3.37) is multiplied by $\mathbf{X}_\mu$ and integrated over the RVE volume to give

$$\begin{aligned}\int_{\Omega_\mu} \nabla_0 \mathbf{x}_\mu \left(\mathbf{X}_o, \mathbf{X}_\mu \right) \otimes \mathbf{X}_\mu dV &= \mathbf{F}\left(\mathbf{X}_o \right) \otimes \int_{\Omega_\mu} \mathbf{X}_\mu dV \\ &+ \mathbf{G}\left(\mathbf{X}_o \right) \cdot \int_{\Omega_\mu} \mathbf{X}_\mu \otimes \mathbf{X}_\mu dV \\ &+ \int_{\Omega_\mu} \nabla \mathbf{w}\left(\mathbf{X}_\mu \right) \otimes \mathbf{X}_\mu dV.\end{aligned} \tag{3.54}$$

Knowing by (3.39) that the first moment of volume of the undeformed RVE is zero and defining the second moment of volume of the undeformed RVE as $\mathbf{J} = \int_{\Omega_\mu} \mathbf{X}_\mu \otimes \mathbf{X}_\mu dV$. Equation (3.54) can be rewritten as

$$\mathbf{G}\left(\mathbf{X}_o\right) \cdot \mathbf{J} = \int_{\Omega_\mu} \nabla \mathbf{x}_\mu \left(\mathbf{X}_o, \mathbf{X}_\mu\right) \otimes \mathbf{X}_\mu dV - \int_{\Omega_\mu} \nabla \mathbf{w}\left(\mathbf{X}_\mu\right) \otimes \mathbf{X}_\mu dV, \tag{3.55}$$

replacing the following relationships

$$\nabla \mathbf{x}_\mu \left(\mathbf{X}_o, \mathbf{X}_\mu\right) \otimes \mathbf{X}_\mu = \nabla \left(\mathbf{x}_\mu \left(\mathbf{X}_o, \mathbf{X}_\mu\right) \otimes \mathbf{X}_\mu\right) - \mathbf{x}_\mu \left(\mathbf{X}_o, \mathbf{X}_\mu\right) \otimes \mathbf{I}, \tag{3.56}$$

and

$$\nabla \mathbf{w}\left(\mathbf{X}_\mu\right) \otimes \mathbf{X}_\mu = \nabla \left(\mathbf{w}\left(\mathbf{X}_\mu\right) \otimes \mathbf{X}_\mu\right) - \mathbf{w}\left(\mathbf{X}_\mu\right) \otimes \mathbf{I}, \tag{3.57}$$

it is obtained

$$\begin{aligned} \mathbf{G}\left(\mathbf{X}_o\right) \cdot \mathbf{J} &= \int_{\Omega_\mu} \nabla \left(\mathbf{x}_\mu \left(\mathbf{X}_o, \mathbf{X}_\mu\right) \otimes \mathbf{X}_\mu\right) dV \\ &- \int_{\Omega_\mu} \nabla \left(\mathbf{w}\left(\mathbf{X}_\mu\right) \otimes \mathbf{X}_\mu\right) dV \\ &- \int_{\Omega_\mu} \mathbf{x}_\mu \left(\mathbf{X}_o, \mathbf{X}_\mu\right) dV \otimes \mathbf{I} + \int_{\Omega_\mu} \mathbf{w}\left(\mathbf{X}_\mu\right) dV \otimes \mathbf{I}. \end{aligned} \tag{3.58}$$

Using (3.35) it can be shown that

$$\int_{\Omega_\mu} \mathbf{x}_\mu \left(\mathbf{X}_o, \mathbf{X}_\mu\right) dV \otimes \mathbf{I} = \frac{1}{2} \mathbf{G}\left(\mathbf{X}_o\right) : \mathbf{J} \otimes \mathbf{I} + \int_{\Omega_\mu} \mathbf{w}\left(\mathbf{X}_\mu\right) dV \otimes \mathbf{I}, \tag{3.59}$$

which is used to obtain the final version of the sought expression

$$\begin{aligned} \mathbf{G}\left(\mathbf{X}_o\right) \cdot \mathbf{J} + \tfrac{1}{2} \mathbf{G}\left(\mathbf{X}_o\right) : \mathbf{J} \otimes \mathbf{I} &= \int_{\Omega_\mu} \nabla \left(\mathbf{x}_\mu \left(\mathbf{X}_o, \mathbf{X}_\mu\right) \otimes \mathbf{X}_\mu\right) dV \\ &- \int_{\Omega_\mu} \nabla \left(\mathbf{w}\left(\mathbf{X}_\mu\right) \otimes \mathbf{X}_\mu\right) dV, \end{aligned} \tag{3.60}$$

and applying the divergence theorem in the right hand size the equation can be rewritten in term of surface integral as

$$\begin{aligned} \mathbf{G}\left(\mathbf{X}_o\right) \cdot \mathbf{J} + \tfrac{1}{2} \mathbf{G}\left(\mathbf{X}_o\right) : \mathbf{J} \otimes \mathbf{I} &= \int_{\partial\Omega_\mu} \mathbf{x}_\mu \left(\mathbf{X}_o, \mathbf{X}_\mu\right) \otimes \mathbf{X}_\mu \otimes \mathbf{N} dA \\ &- \int_{\partial\Omega_\mu} \mathbf{w}\left(\mathbf{X}_\mu\right) \otimes \mathbf{X}_\mu \otimes \mathbf{N} dA. \end{aligned} \tag{3.61}$$

It is possible to make a parallelism between (3.15) and (3.61). The additional condition regarding the second moment of area of the deformed RVE given by (3.54) requires that the influence of the displacement fluctuation field should vanish, then

$$\int_{\partial\Omega_\mu} \mathbf{w}\left(\mathbf{X}_\mu\right) \otimes \mathbf{X}_\mu \otimes \mathbf{N} dA = \mathbf{0} \tag{3.62}$$

Equation (3.62) is a boundary restriction writes for the displacement fluctuation field, then it is not necessary a high-order boundary value problem on the microscopic level to satisfy the new boundary condition deduced from it. Considering again the cubic geometry in the reference configuration taking previously for the RVE (see Figure 3.3) the restriction given by (3.62) can be splitted in the different surfaces of the domain as

$$\begin{aligned} &\left(\int_{\mathbf{N}_X^+} \mathbf{w} \otimes \mathbf{X}_\mu dA_{yz} - \int_{\mathbf{N}_X^-} \mathbf{w} \otimes \mathbf{X}_\mu dA_{yz}\right) \otimes \mathbf{N}_X^+ \\ &+ \left(\int_{\mathbf{N}_Y^+} \mathbf{w} \otimes \mathbf{X}_\mu dA_{xz} - \int_{\mathbf{N}_Y^-} \mathbf{w} \otimes \mathbf{X}_\mu dA_{xz}\right) \otimes \mathbf{N}_Y^+ \\ &+ \left(\int_{\mathbf{N}_Z^+} \mathbf{w} \otimes \mathbf{X}_\mu dA_{xy} - \int_{\mathbf{N}_Z^-} \mathbf{w} \otimes \mathbf{X}_\mu dA_{xy}\right) \otimes \mathbf{N}_Z^+ = \mathbf{0}. \end{aligned} \tag{3.63}$$

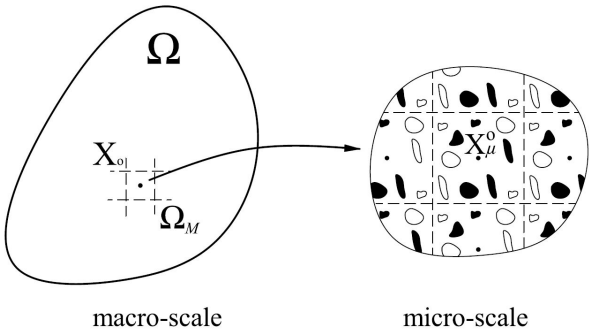

Figure 3.5: Macro volume Ω_M around point $\mathbf{X}_o$ and its micro structure.

In the case of *periodic boundary fluctuations* condition has been considered the last expression is automatically satisfies is

$$\int_{\mathbf{N}_X^-} \mathbf{w} dA_{yz} = \mathbf{0} \quad , \quad \int_{\mathbf{N}_Y^-} \mathbf{w} dA_{xz} = \mathbf{0} \quad \text{and} \quad \int_{\mathbf{N}_Z^-} \mathbf{w} dA_{xy} = \mathbf{0} \tag{3.64}$$

Therefore, the extra boundary condition required in this case is that the integral of the periodic displacement fluctuations on the RVE surfaces must to be zero.

3.4.2 Microscopic and macroscopic strain tensor

In this enhanced first-order homogenization the strain tensor in the microstructural level for infinitesimal deformation approach can be written as

$$\begin{aligned} \mathbf{E}_\mu\left(\mathbf{X}_o, \mathbf{X}_\mu\right) &= \tfrac{1}{2}\left(\mathbf{F}_\mu\left(\mathbf{X}_o, \mathbf{X}_\mu\right) + \mathbf{F}_\mu^T\left(\mathbf{X}_o, \mathbf{X}_\mu\right)\right) - \mathbf{I} \\ &= \tfrac{1}{2}\left(\mathbf{F}\left(\mathbf{X}_o\right) + \mathbf{F}^T\left(\mathbf{X}_o\right)\right) - \mathbf{I} \\ &+ \tfrac{1}{2}\left(\mathbf{G}\left(\mathbf{X}_o\right)\cdot\mathbf{X}_\mu + \left(\mathbf{G}\left(\mathbf{X}_o\right)\cdot\mathbf{X}_\mu\right)^T\right) \\ &+ \tfrac{1}{2}\left(\nabla\mathbf{w}\left(\mathbf{X}_\mu\right) + \left(\nabla\mathbf{w}\left(\mathbf{X}_\mu\right)\right)^T\right), \end{aligned} \tag{3.65}$$

and because (3.10) is satisfied and by (3.39) the obtained expression of the volume average of the microscopic strain tensor over the RVE domain is the same than (3.23) which was obtained previously in Section 3.3.3. Therefore, the microscopic strain tensor can be rewrtten as

$$\mathbf{E}_\mu\left(\mathbf{X}_o, \mathbf{X}_\mu\right) = \mathbf{E}\left(\mathbf{X}_o\right) + \mathbf{E}_\mu^G\left(\mathbf{X}_o, \mathbf{X}_\mu\right) + \mathbf{E}_\mu^w\left(\mathbf{X}_\mu\right), \tag{3.66}$$

where $\mathbf{E}_\mu^G = \frac{1}{2}\left(\mathbf{G}\cdot\mathbf{X}_\mu + \left(\mathbf{G}\cdot\mathbf{X}_\mu\right)^T\right)$ is a new term in the microscopic strain tensor because the second-order term $\mathbf{G}$ is included in the formulation. It can be proved that the volume average of this new term $\mathbf{E}_\mu^G$ over the RVE domain is equal zero because (3.39).

3.4.3 Hill-Mandel principle and RVE equilibrium

When the second-order of the Taylor series expansion given by (3.3) is used to improve the approximation of the deformed position of a material point in the RVE (see (3.34)) is assumed that a macroscopic finite volume Ω_M around the considered point $\mathbf{X}_o$ exists as Figure 3.5 is showing. This finite volume must to be smaller than the characteristic macroscopic dimension, this volume is just the RVE. Therefore, the Hill-Mandel principle should be applied now not only taking into account the virtual work of the point $\mathbf{X}_o$, if not the volume average of the virtual work in the macro volume Ω_M must be considered. It can be stated as

$$\frac{1}{V_M}\int_{\Omega_M} \mathbf{S} : \delta\mathbf{E} dV = \frac{1}{V_\mu}\int_{\Omega_\mu} \mathbf{S}_\mu : \delta\mathbf{E}_\mu dV \tag{3.67}$$

The macroscopic deformed position of a material point in Ω_M around the point $\mathbf{X}_o$ can be approximated until a second-order approach using (3.3) as

$$\triangle \mathbf{x} \cong \mathbf{F}\left(\mathbf{X}_o\right) \cdot \triangle \mathbf{X} + \frac{1}{2}\mathbf{G}\left(\mathbf{X}_o\right) : \triangle \mathbf{X} \otimes \triangle \mathbf{X}, \tag{3.68}$$

and the approximated macroscopic deformation gradient is

$$\mathbf{F} \cong \mathbf{F}\left(\mathbf{X}_o\right) + \mathbf{G}\left(\mathbf{X}_o\right) \cdot \triangle \mathbf{X}. \tag{3.69}$$

The macroscopic strain tensor in the Ω_M domain for infinitesimal deformation approach can be approximated as

$$\mathbf{E} \cong \frac{1}{2}\left(\mathbf{F}\left(\mathbf{X}_o\right) + \mathbf{F}^T\left(\mathbf{X}_o\right)\right) - \mathbf{I} + \frac{1}{2}\left(\mathbf{G}\left(\mathbf{X}_o\right) \cdot \triangle \mathbf{X} + \left(\mathbf{G}\left(\mathbf{X}_o\right) \cdot \triangle \mathbf{X}\right)^T\right) \tag{3.70}$$

or

$$\mathbf{E} \cong \mathbf{E}\left(\mathbf{X}_o\right) + \mathbf{E}^G\left(\mathbf{X}_o, \mathbf{X}\right), \tag{3.71}$$

where $\mathbf{E}^G = \frac{1}{2}\left(\mathbf{G} \cdot \triangle \mathbf{X} + \left(\mathbf{G} \cdot \triangle \mathbf{X}\right)^T\right)$.

Taking into account (3.66) and (3.71) it can be rewritten (3.67) as

$$\begin{aligned} \frac{1}{V_M}\int_{\Omega_M} \mathbf{S}dV : \delta\mathbf{E} + \frac{1}{V_M}\int_{\Omega_M} \mathbf{S} : \delta\mathbf{E}^G dV = \frac{1}{V_\mu}\int_{\Omega_\mu} \mathbf{S}_\mu dV : \delta\mathbf{E} \\ + \frac{1}{V_\mu}\int_{\Omega_\mu} \mathbf{S}_\mu : \delta\mathbf{E}_\mu^G dV + \frac{1}{V_\mu}\int_{\Omega_\mu} \mathbf{S}_\mu : \delta\mathbf{E}_\mu^w dV \end{aligned} \tag{3.72}$$

and because of the symmetry property of the stress tensor can be shown that $\mathbf{S} : (\nabla\mathbf{a}) = \mathbf{S} : (\nabla\mathbf{a})^T$ and $\mathbf{S} : (\mathbf{G}.\mathbf{a}) = \mathbf{S} : (\mathbf{G}.\mathbf{a})^T$, where $\mathbf{a}$ is a first order tensor. Then, (3.72) is finally

$$\begin{aligned} \frac{1}{V_M}\int_{\Omega_M} \mathbf{S}dV : \delta\mathbf{E} + \frac{1}{V_M}\int_{\Omega_M} \mathbf{S} \otimes \triangle\mathbf{X}dV \vdots \delta\mathbf{G} = \frac{1}{V_\mu}\int_{\Omega_\mu} \mathbf{S}_\mu dV : \delta\mathbf{E} \\ + \frac{1}{V_\mu}\int_{\Omega_\mu} \mathbf{S}_\mu \otimes \mathbf{X}_\mu dV \vdots \delta\mathbf{G} + \frac{1}{V_\mu}\int_{\Omega_\mu} \mathbf{S}_\mu : \nabla^s\delta\mathbf{w}dV. \end{aligned} \tag{3.73}$$

Following the same procedure that in Section 3.3.4 to satisfy the above expression

$$\hat{\mathbf{S}} \equiv \frac{1}{V_M}\int_{\Omega_M} \mathbf{S}dV \equiv \frac{1}{V_\mu}\int_{\Omega_\mu} \mathbf{S}_\mu dV, \tag{3.74}$$

where $\hat{\mathbf{S}}$ is the homogenized stress tenor, which is obtained as the volume average of the stress tensor around the point $\mathbf{X}_o$, and

$$\hat{\mathbf{Q}} \equiv \frac{1}{V_M}\int_{\Omega_M} \mathbf{S} \otimes \triangle\mathbf{X}dV \equiv \frac{1}{V_\mu}\int_{\Omega_\mu} \mathbf{S}_\mu \otimes \mathbf{X}_\mu dV. \tag{3.75}$$

where $\hat{\mathbf{Q}}$ is the homogenized second-order stress tensor in the point $\mathbf{X}_o$, which is a the three-order tensor. Finally, the RVE's variational equilibrium equation is

$$\int_{\Omega_\mu} \mathbf{S}_\mu : \nabla^s\delta\mathbf{w}dV = 0, \tag{3.76}$$

that must be satisfied for any kinematically admissible displacement fluctuation field $\mathbf{w}$ showing in Section 3.4.1.

3.4.4 Homogenized stress and second-order stress tensor

The microscopic stress tensor can be obtained as

$$\mathbf{S}_\mu = \mathbf{C}_\mu : \mathbf{E}\left(\mathbf{X}_o\right) + \mathbf{C}_\mu : \mathbf{E}_\mu^G\left(\mathbf{X}_o, \mathbf{X}_\mu\right) + \mathbf{C}_\mu : \mathbf{E}_\mu^w\left(\mathbf{X}_\mu\right), \tag{3.77}$$

then, the homogenized stress tensor in the macroscopic level given by (3.74) is

$$\hat{\mathbf{S}} = \frac{1}{V_\mu}\int_{\Omega_\mu} \mathbf{C}_\mu dV : \mathbf{E}\left(\mathbf{X}_o\right) + \frac{1}{V_\mu}\int_{\Omega_\mu} \mathbf{C}_\mu : \mathbf{E}_\mu^G\left(\mathbf{X}_o, \mathbf{X}_\mu\right) dV + \frac{1}{V_\mu}\int_{\Omega_\mu} \mathbf{C}_\mu : \mathbf{E}_\mu^w\left(\mathbf{X}_\mu\right) dV \tag{3.78}$$

or

$$\hat{\mathbf{S}} = \bar{\mathbf{C}} : \mathbf{E}\left(\mathbf{X}_o\right) + \bar{\mathbf{B}} \vdots \mathbf{G}\left(\mathbf{X}_o\right) + \frac{1}{V_\mu}\int_{\Omega_\mu} \mathbf{C}_\mu : \mathbf{E}_\mu^w\left(\mathbf{X}_\mu\right) dV, \tag{3.79}$$

where

$$\bar{\mathbf{B}} \equiv \frac{1}{V_\mu}\int_{\Omega_\mu} \mathbf{C}_\mu \otimes \mathbf{X}_\mu dV. \tag{3.80}$$

The tensor $\bar{\mathbf{B}}$ can be also considered as a microscopic material property. This constitutive tensor relates gradient of the deformation gradient tensor $\mathbf{G}$ to homogenized stress tensor $\hat{\mathbf{S}}$ and generates a coupling effect. This tensor $\bar{\mathbf{B}}$ is analogous to the called *bending-extension coupling matrix* used in plates or shells theories [4].

Equation (3.79) shows that the homogenized stress tensor $\hat{\mathbf{S}}$ in the point $\mathbf{X}_o$ depends of the macroscopic tensor $\mathbf{E}$ and $\mathbf{G}$, of the microscopic displacement fluctuation field $\mathbf{w}$ and also, of the vector position $\mathbf{X}_\mu$ of the RVE. Considering now a particular case where the simple materials within the RVE are symmetrically located respect to the coordinate system's origin, which has been placed on the RVE geometric center (see Section 3.4.1). It can be proved that taking this symmetric distribution of the simple materials the value obtains for the constitutive tensor $\bar{\mathbf{B}}$ is zero. Therefore, the homogenized stress tensor for this case can be rewritten as

$$\hat{\mathbf{S}} = \bar{\mathbf{C}} : \mathbf{E}\left(\mathbf{X}_o\right) + \frac{1}{V_\mu}\int_{\Omega_\mu} \mathbf{C}_\mu : \mathbf{E}_\mu^w\left(\mathbf{X}_\mu\right) dV. \tag{3.81}$$

The macroscopic second-order term $\mathbf{G}$ and of the vector position $\mathbf{X}_\mu$ do not affect the homogenized stress tensor. The expression given by (3.81) is the same than the one obtained for first-order homogenization given by (3.32).

On the other hand, the homogenized second-order stress tensor can be obtained using (3.75) and the microscopic stress tensor given by (3.77) as

$$\begin{aligned} \hat{\mathbf{Q}} &= \frac{1}{V_\mu}\int_{\Omega_\mu} \mathbf{C}_\mu \otimes \mathbf{X}_\mu dV : \mathbf{E}\left(\mathbf{X}_o\right) \\ &+ \frac{1}{V_\mu}\int_{\Omega_\mu} \left(\mathbf{C}_\mu \otimes \mathbf{X}_\mu\right) : \mathbf{E}_\mu^G\left(\mathbf{X}_o, \mathbf{X}_\mu\right) dV \\ &+ \frac{1}{V_\mu}\int_{\Omega_\mu} \mathbf{C}_\mu : \mathbf{E}_\mu^w\left(\mathbf{X}_\mu\right) \otimes \mathbf{X}_\mu dV, \end{aligned} \tag{3.82}$$

or

$$\hat{\mathbf{Q}} = \bar{\mathbf{B}} : \mathbf{E}\left(\mathbf{X}_o\right) + \bar{\mathbf{D}} \vdots \mathbf{G}\left(\mathbf{X}_o\right) + \frac{1}{V_\mu}\int_{\Omega_\mu} \mathbf{C}_\mu : \mathbf{E}_\mu^w\left(\mathbf{X}_\mu\right) \otimes \mathbf{X}_\mu dV, \tag{3.83}$$

where

$$\bar{\mathbf{D}} = \frac{1}{V_\mu}\int_{\Omega_\mu} \left(\mathbf{C}_\mu \otimes \mathbf{X}_\mu\right) \otimes \mathbf{X}_\mu dV. \tag{3.84}$$

The tensor $\bar{\mathbf{D}}$ is also considered as a microscopic material property which is obtained through the RVE how the constitutive tensors $\bar{\mathbf{C}}$ and $\bar{\mathbf{B}}$. Taking into account the symmetric distribution of the simple materials within the RVE above considered the expression for the homogenized second-order stress can be obtained as

$$\hat{\mathbf{Q}} = \bar{\mathbf{D}} \vdots \mathbf{G}\left(\mathbf{X}_o\right) + \frac{1}{V_\mu}\int_{\Omega_\mu} \mathbf{C}_\mu : \mathbf{E}_\mu^w\left(\mathbf{X}_\mu\right) \otimes \mathbf{X}_\mu dV, \tag{3.85}$$

Equation (3.85) shows that the second-order stress tensor $\hat{\mathbf{Q}}$ of the macroscopic tensor $\mathbf{G}$ and of the microscopic displacement fluctuation field $\mathbf{w}$ but also, of the vector position $\mathbf{X}_\mu$ of material point in the RVE. In addition, the tensor $\bar{\mathbf{D}}$ does not vanish because of the symmetric simple materials distribution.

3.5 Final remarks of the formulations

In the enhanced-first-order approach is lost the benefit showing in the first-order approach about the non dimensional RVE. The microscopic strain (3.66) and stress (3.77) tensor now have an explicit dependence with the material vector position $\mathbf{X}_\mu$ in the RVE. This dependence has been observed also in the homogenized second-order stress tensor (3.85). While the homogenized stress tensor (3.81) is not dependent of $\mathbf{X}_\mu$ when a symmetric internal distribution of the simple materials is taken. Besides, to satisfy (3.72), which is obtained from the Hill-Mandel condition extended to the enhanced-first-order approach, must be imposed $\Omega_\mu \equiv \Omega_M$. Thus the RVE's dimension used to characterize the microstructure should be equal than the size of the finite volume around the considered point $\mathbf{X}_o$. Then, the improved first-order homogenization procedure can be understand as a domain decomposition where the sub-domains have a periodic microstructure.

However, the enhanced-first-order homogenization is better than the first-order homogenization from a microscopic viewpoint. Although the homogenized stress tensor for both theories is the same, the microscopic displacement field, the microscopic strain and stress tensors are not equal. The improved first-order approach gets a better approximation of the microscopic behavior because the extra term $\mathbf{G}$ is considered in the formulation. Therefore, in a non-linear analysis the beginning and the evolution of the non-linear behavior since the microscopic analysis are better approximates using the enriched first-order formulation.

On the other hand, from the formulation is possible to observe that the enhanced-first-order homogenization contains to the first-order homogenization. Therefore, when the principle of separation of scales is verified the results obtained using the enriched formulation will be the same than the ones obtained using the first-order homogenization. In other words, if the periodic microstructural length scale l_μ is much smaller than the structure characteristic length l (see Figure 3.1), the contribution of include the extra term consider in (3.35) to improved the first-order approach is negligible.

The landed variational equilibrium equation in the microstructure for both homogenization formulations is the same (3.29) and (3.76). However, in the enriched first-order homogenization formulation extra boundary condition should be satisfied. High-order boundary conditions (3.53) are obtained if the natural extension of the first average theorem is proposed (3.43). In consequence, this kind of extra boundary conditions require a high-order microscopic equilibrium equation. To avoid this situation an alternative extension (3.60) of the average theorem shown is used to conserve a first-order microscopic variational problem. The new boundary conditions using the alternative proposed when the case of *Periodic boundary fluctuations* are obtained and showing in (3.64). Finally, for the enhanced-first-order approach a macroscopic second-order stress tensor is obtained from the RVE solution. Therefore, this high-order stress tensor should be considered in the macroscopic scale theory.

3.6 Macroscopic and microscopic formulation

In the following, the boundary value problem (BVP) in the macroscopic and in the microscopic scale levels are presented.

3.6.1 Macroscopic BVP

A BVP is considered for the macrostructural scale level of a domain Ω with a periodic internal microstructure. The kinematics of the problem is related to a displacements field on the macroscopic scale, which expresses the displacement of each material point of the domain Ω. From continuum mechanics the macroscopic BVP is

$$\begin{aligned} \frac{\partial \sigma_{ij}}{\partial x_j} + f_i = 0 \quad & in \quad \Omega, \\ u_i = \bar{u}_i \quad & in \quad \partial\Omega_u, \\ \sigma_{ij} n_j = \bar{t}_i \quad & in \quad \partial\Omega_t, \end{aligned} \tag{3.86}$$

where σ_{ij} is the macroscopic stress tensor and f_i is the internal body force associated to the mass forces of the composite. The boundary of Ω ($\partial\Omega$) is disjointly defined by the surfaces $\partial\Omega_u$ where the macroscopic displacement is known $\bar{u}_i$ (Dirichlet's condition) and $\partial\Omega_t$ where the macroscopic surface load $\bar{t}_i$ are known

(Neumann's condition) with $\partial\Omega_u \cup \partial\Omega_t = \partial\Omega$ and $\partial\Omega_u \cap \partial\Omega_t = \emptyset$. Finally, n_j are the components of an outward versor normal to the surface $\partial\Omega_t$.

Therefore, the resolution of the BVP given by (3.86) consists on the determination of the macroscopic displacement field corresponding to the solution $\mathbf{u} \in \mathrm{V}_\Omega$, where V_Ω is the set of continuous and sufficiently regular functions with zero-valued in $\partial\Omega_u$ The partial differential equation in the macroscopic BVP above presented can be rewritten in a weak form (or variational form) as

$$\int_\Omega \frac{\partial \sigma_{ij}}{\partial x_j} v_i \, dV + \int_\Omega f_i v_i \, dV = 0 \qquad \forall \, v \in \mathrm{V}_\Omega, \tag{3.87}$$

where v_i are the called test functions. Equation (3.87) can be rewritten, applying the divergence theorem, as

$$\int_\Omega \sigma_{ij} \frac{\partial v_i}{\partial x_j} \, dV = \int_\Omega f_i v_i \, dV + \int_{\partial\Omega} \bar{t}_i v_i \, dA \qquad \forall \, v \in V_\Omega. \tag{3.88}$$

Considering infinitesimal deformation the macroscopic strain and stress tensor are

$$\begin{aligned} E_{ij} &= \frac{1}{2}\left(F_{ij} + F_{ij}^T\right) - I_{ij} = \frac{1}{2}\left(\frac{\partial u_i}{\partial x_j} + \frac{\partial u_j}{\partial x_i}\right) \quad in \quad \Omega, \\ \sigma_{ij} &= S_{ij} = \frac{1}{V_\mu}\int_{\Omega_\mu} \mathbf{S}_\mu \, dV \qquad\qquad in \quad \Omega. \end{aligned} \tag{3.89}$$

3.6.2 Microscopic BVP

The obtained variational equilibrium statement (or the virtual work equation) in the microstructure (see (3.29) and (3.76)) can be written as

$$\int_{\Omega_\mu} \mathbf{S}_\mu : \nabla^s \mathbf{w} \, dV = 0 \qquad \forall \, \mathbf{w} \in \mathrm{V}_{\Omega_\mu}. \tag{3.90}$$

Taking into account again infinitesimal deformation, the microscopic strain tensor is

$$\mathbf{E}_\mu = \frac{1}{2}\left(\mathbf{F}_\mu + \mathbf{F}_\mu^T\right) - \mathbf{I} = \nabla^s \mathbf{u}_\mu \quad in \quad \Omega_\mu, \tag{3.91}$$

where $\nabla^s \mathbf{u}_\mu$ is the symmetric gradient of the microscopic displacement field in the RVE and V_{Ω_μ} is the set of continuous and sufficiently regular kinematically admissible RVE displacement fields. Further, it is assumed that in the microstructure the constitutive behavior is described by conventional internal dissipative constitutive theories. Therefore, the microscopic stress tensor is obtained by integrating the constitutive equations, knowing a set of internal variables $\boldsymbol{\alpha}$, for the given strain tensor history. Then, it is

$$\mathbf{S}_\mu = \mathbf{S}_\mu(\mathbf{E}_\mu, \boldsymbol{\alpha}) = \mathbf{S}_\mu(\nabla^s \mathbf{u}_\mu, \boldsymbol{\alpha}). \tag{3.92}$$

With the above at hand, the resolution of the microstucture problem consists on the determination of the microscopic displacement field $\mathbf{u}_\mu \in \mathrm{V}_{\Omega_\mu}$ of the variational problem for a given macroscopic deformation gradient tensor $\mathbf{F}$ and its gradient $\mathbf{G}$ in enhanced-first-order approach case. Therefore, to complete the BVP in the microscopic scale is necessary to define the boundary condition used to obtain kinematically admissible displacement fields since the solution of (3.90).

First-order approach

In the Section 3.3.2, the different displacement fluctuation fields kinematically admissible were obtained. Using (3.9) is possible to obtain the boundary condition for each case in term of the displacement field as

(i) *Taylor model* (or zero fluctuations):

$$\mathbf{u}_\mu = (\mathbf{F} - \mathbf{I}) \cdot \mathbf{X}_\mu, \quad in \quad \forall \, \mathbf{X}_\mu \in \Omega_\mu.$$

In this model is not necessary to solve (3.90).

(ii) *Linear boundary displacements* (or zero boundary fluctuations):

$$\mathbf{u}_\mu = (\mathbf{F} - \mathbf{I}) \cdot \mathbf{X}_\mu, \quad in \quad \forall\, \mathbf{X}_\mu \in \partial\Omega_\mu.$$

In this case a classical BVP with only Dirichlet condition is obtained.

(iii) *Periodic boundary fluctuations*:

$$\mathbf{u}_\mu(\mathbf{X}_\mu^+) - \mathbf{u}_\mu(\mathbf{X}_\mu^-) = D_1(\mathbf{F} - \mathbf{I}) \cdot \mathbf{N}_X^+, \quad in \quad \forall\, pairs\ \left\{\mathbf{X}_\mu^+, \mathbf{X}_\mu^-\right\} \in \partial\Omega_{\mu|\mathbf{N}_X}.$$

$$\mathbf{u}_\mu(\mathbf{X}_\mu^+) - \mathbf{u}_\mu(\mathbf{X}_\mu^-) = D_2(\mathbf{F} - \mathbf{I}) \cdot \mathbf{N}_Y^+, \quad in \quad \forall\, pairs\ \left\{\mathbf{X}_\mu^+, \mathbf{X}_\mu^-\right\} \in \partial\Omega_{\mu|\mathbf{N}_Y}.$$

$$\mathbf{u}_\mu(\mathbf{X}_\mu^+) - \mathbf{u}_\mu(\mathbf{X}_\mu^-) = D_3(\mathbf{F} - \mathbf{I}) \cdot \mathbf{N}_Z^+, \quad in \quad \forall\, pairs\ \left\{\mathbf{X}_\mu^+, \mathbf{X}_\mu^-\right\} \in \partial\Omega_{\mu|\mathbf{N}_Z}.$$

In this case, the boundary condition is a constraint boundary condition.

(iv) *Minimal constraint* (or uniform boundary traction):

$$\int_{\mathbf{N}_X^+} \mathbf{u}_\mu dA_{yz} - \int_{\mathbf{N}_X^-} \mathbf{u}_\mu dA_{yz} = D_1(\mathbf{F} - \mathbf{I}) \cdot \mathbf{N}_X^+, \quad in \quad \forall\, \mathbf{X}_\mu \in \partial\Omega_{\mu|\mathbf{N}_X}.$$

$$\int_{\mathbf{N}_Y^+} \mathbf{u}_\mu dA_{xz} - \int_{\mathbf{N}_Y^-} \mathbf{u}_\mu dA_{xz} = D_2(\mathbf{F} - \mathbf{I}) \cdot \mathbf{N}_Y^+, \quad in \quad \forall\, \mathbf{X}_\mu \in \partial\Omega_{\mu|\mathbf{N}_Y}.$$

$$\int_{\mathbf{N}_Z^+} \mathbf{u}_\mu dA_{xy} - \int_{\mathbf{N}_Z^-} \mathbf{u}_\mu dA_{xy} = D_3(\mathbf{F} - \mathbf{I}) \cdot \mathbf{N}_Z^+, \quad in \quad \forall\, \mathbf{X}_\mu \in \partial\Omega_{\mu|\mathbf{N}_Z}.$$

And for this case, the boundary condition is an integral constraint boundary condition.

Enhanced-first-order approach

In the Section 3.4.1, the different displacement fluctuation fields kinematically admissible were obtained for the enriched first-order approach. Besides, in this approach extra restriction on the displacement fluctuation field exists because the term $\mathbf{G}$ is introduced in the microscopic displacement field. Using (3.36) is possible to obtain the boundary condition for each case in term of the displacement field as

(i) *Taylor model* (or zero fluctuations):

$$\mathbf{u}_\mu = (\mathbf{F} - \mathbf{I}) \cdot \mathbf{X}_\mu + \frac{1}{2}\mathbf{G} : \mathbf{X}_\mu \otimes \mathbf{X}_\mu, \quad in \quad \forall\, \mathbf{X}_\mu \in \Omega_\mu.$$

In this model is not necessary to solve (3.90).

(ii) *Linear boundary displacements* (or zero boundary fluctuations):

$$\mathbf{u}_\mu = (\mathbf{F} - \mathbf{I}) \cdot \mathbf{X}_\mu + \frac{1}{2}\mathbf{G} : \mathbf{X}_\mu \otimes \mathbf{X}_\mu, \quad in \quad \forall\, \mathbf{X}_\mu \in \partial\Omega_\mu.$$

A classical BVP with only Dirichlet condition is obtained because the extra boundary restriction (3.62) is automatically verified.

(iii) *Periodic boundary fluctuations*:

$$\begin{aligned}
\mathbf{u}_\mu(\mathbf{X}_\mu^+) - \mathbf{u}_\mu(\mathbf{X}_\mu^-) &= D_1(\mathbf{F}-\mathbf{I})\cdot\mathbf{N}_X^+ + \frac{(D_1)^2}{2}\mathbf{N}_X^+\cdot\mathbf{G}\cdot\mathbf{N}_X^+ \\
&+ D_1\mathbf{G}:\mathbf{N}_X^+\otimes\mathbf{X}_\mu^-,\ in\ \forall\ pairs\ \left\{\mathbf{X}_\mu^+,\mathbf{X}_\mu^-\right\}\in\partial\Omega_{\mu|\mathbf{N}_X}. \\
\mathbf{u}_\mu(\mathbf{X}_\mu^+) - \mathbf{u}_\mu(\mathbf{X}_\mu^-) &= D_2(\mathbf{F}-\mathbf{I})\cdot\mathbf{N}_Y^+ + \frac{(D_2)^2}{2}\mathbf{N}_Y^+\cdot\mathbf{G}\cdot\mathbf{N}_Y^+ \\
&+ D_2\mathbf{G}:\mathbf{N}_Y^+\otimes\mathbf{X}_\mu^-,\ in\ \forall\ pairs\ \left\{\mathbf{X}_\mu^+,\mathbf{X}_\mu^-\right\}\in\partial\Omega_{\mu|\mathbf{N}_Y}. \\
\mathbf{u}_\mu(\mathbf{X}_\mu^+) - \mathbf{u}_\mu(\mathbf{X}_\mu^-) &= D_3(\mathbf{F}-\mathbf{I})\cdot\mathbf{N}_Z^+ + \frac{(D_3)^2}{2}\mathbf{N}_Z^+\cdot\mathbf{G}\cdot\mathbf{N}_Z^+ \\
&+ D_3\mathbf{G}:\mathbf{N}_Z^+\otimes\mathbf{X}_\mu^-,\ in\ \forall\ pairs\ \left\{\mathbf{X}_\mu^+,\mathbf{X}_\mu^-\right\}\in\partial\Omega_{\mu|\mathbf{N}_Z}.
\end{aligned}$$

And to satisfy the extra boundary restriction given by (3.64) extra boundary conditions are:

$$\begin{aligned}
\int_{\mathbf{N}_X^-}\mathbf{u}_\mu dA_{yz} &= -\frac{1}{2}D_1D_2D_3(\mathbf{F}-\mathbf{I})\cdot\mathbf{N}_X^+ + \frac{1}{8}(D_1)^2D_2D_3\mathbf{G}:\mathbf{N}_X^+\otimes\mathbf{N}_X^+ \\
&+ \frac{1}{24}(D_2)^3D_3\mathbf{G}:\mathbf{N}_Y^+\otimes\mathbf{N}_Y^+ \\
&+ \frac{1}{24}D_2(D_3)^3\mathbf{G}:\mathbf{N}_Z^+\otimes\mathbf{N}_Z^+,\quad in\ \ \forall\,\mathbf{X}_\mu\in\partial\Omega_{\mu|\mathbf{N}_X^-}. \\
\int_{\mathbf{N}_Y^-}\mathbf{u}_\mu dA_{xz} &= -\frac{1}{2}D_1D_2D_3(\mathbf{F}-\mathbf{I})\cdot\mathbf{N}_Y^+ + \frac{1}{8}D_1(D_2)^2D_3\mathbf{G}:\mathbf{N}_Y^+\otimes\mathbf{N}_Y^+ \\
&+ \frac{1}{24}(D_1)^3D_3\mathbf{G}:\mathbf{N}_X^+\otimes\mathbf{N}_X^+ \\
&+ \frac{1}{24}D_1(D_3)^3\mathbf{G}:\mathbf{N}_Z^+\otimes\mathbf{N}_Z^+,\quad in\ \ \forall\,\mathbf{X}_\mu\in\partial\Omega_{\mu|\mathbf{N}_Y^-}. \\
\int_{\mathbf{N}_Z^-}\mathbf{u}_\mu dA_{xy} &= -\frac{1}{2}D_1D_2D_3(\mathbf{F}-\mathbf{I})\cdot\mathbf{N}_Z^+ + \frac{1}{8}D_1D_2(D_3)^2\mathbf{G}:\mathbf{N}_Z^+\otimes\mathbf{N}_Z^+ \\
&+ \frac{1}{24}(D_1)^3D_2\mathbf{G}:\mathbf{N}_X^+\otimes\mathbf{N}_X^+ \\
&+ \frac{1}{24}D_1(D_2)^3\mathbf{G}:\mathbf{N}_Y^+\otimes\mathbf{N}_Y^+,\quad in\ \ \forall\,\mathbf{X}_\mu\in\partial\Omega_{\mu|\mathbf{N}_Z^-}.
\end{aligned}$$

In this case, one boundary condition is a constraint boundary condition and the extra boundary condition is an integral constraint boundary condition.

Consequence of the boundary condition considered

The RVE has finite dimension, then this is opposed to the theoretically infinite microstructure considered which create the intrinsic problem of the non-physical RVE edges. Therefore, the election of the boundary condition in the RVE problem is essential to characterize the real behavior of the microstructure. The boundary conditions shown in the above sections are obtained since the restriction on the microscopic displacement fields by the first average postulate (3.10) and they are used to impose the driving macroscopic deformation gradient tensor $\mathbf{F}$ (or strain tensor) on the RVE. Besides, these boundary restrictions should incorporate the presence of the surrounding material of the RVE without (or minimizing) the introduction of spurious effects.

It has been shown in Section 3.3.5 that the boundary condition used in the RVE problem affects the macroscopic stress tensor obtained and therefore also to the homogenized constitutive tensor. Since

(3.32) was concluded that *Taylor model* condition, which in fact is not a real boundary condition in the more pure sense, resulting in an upper bound of the estimated homogenized microscopic stiffness. The effective constitutive tensor estimated is the same that the one predicted by the classical mixing theory.

On the other hand, the *Minimal constraint* provides the lower bound of the estimated effective microstructural stiffness. This boundary condition imposes the macroscopic strain tensor on the RVE in the weakest sense. It has been shown that the resulting boundary distribution of the microscopic stress tensor in the RVE is uniform and equal to the macroscopic stress tensor in this boundary restriction [83, 22]. The *Linear boundary displacements* condition is a too restrictive constraint and it overestimate the homogenized microscopic stiffness [13]. A conventional BVP with full Dirichlet's condition is obtained for the microstructure when this condition is addressed.

It has been shown in the literature that in general the *Periodic boundary fluctuations* provide a better apparent stiffness estimate for both periodic as well as random microstructures [120, 125, 83, 52, 53, 84, 102]. This condition makes that the RVE self adjoint by point to point (pairs of points) coupling of boundary displacements, thereby it naturally incorporates the mechanical response of the surrounding material. Moreover, an anti-periodic condition of the boundary forces is automatically fulfilled in the microscopic problem because the boundary points of the RVE are really made as internal points of the structure.

Because all of this, the *Periodic boundary fluctuations* condition will be used in the computational implementation of the microscopic BVP.

3.7 Finite element implementation

The numerical implementation of the developed homogenization approaches is made through the FEM. This method splits the total domain of the problem in finite n sub-domains known as finite element where the unknown displacement field is approximated using known displacements of some points (called nodal points) and shape functions.

When the FEM is used to solve the weak formulation of a BVP the total integration domain of the problem is separated in the n sub-domains which are the FE domains. The value of the definite integral in the FE domain is obtained using some numerical integration procedure. In general, the numerical integration methods approximate the integral value as the weighted sum of the evaluated integrand in a finite set of points called integration points. These integration points and weights depend of the accuracy required and of course, of the integration method. In the following, the selected method will be the Gaussian quadrature rule which uses n-points (x_i) called Gauss points and n-weights (w_i) to obtain the numerical approximate value of the integral.

To solve the BVP at the macroscopic scale level a classical implementation of FEM is used. Therefore, it will be necessary to know the macroscopic stress tensor on the integration points of the FEs in the macro domain. To achieve the stress tensor in the FE domain a constitutive model which describes the composite behavior must be considered. The multiscale homogenization approaches above described are the chosen constitutive models. Consequently, the macroscopic stress tensor is obtained through the analysis of the microscopic scale. The macroscopic deformation gradient tensor ($\mathbf{F}$), for the first-order homogenization, and its gradient tensor ($\mathbf{G}$), for the enhanced-first-order homogenization, are used to solve the microscopic BVP. The microscopic solution is used to obtain the homogenized stress tensor required to solve the macroscopic BVP through the FEM.

The considered macrostructural point $\mathbf{X}_o$ in the formulation represents physically the Gauss points on the FE. Therefore, the macroscopic values of the deformation gradient tensor $\mathbf{F}(\mathbf{X}_o)$ and the gradient of the deformation gradient tensor $\mathbf{G}(\mathbf{X}_o)$ using in the microscopic BVP are obtained in these Gauss points when the macroscopic BVP is solved.

3.7.1 Microscopic numerical implementation

One more time, to solve the BVP at the microscopic scale level now the FEM has been used again. Therefore, the unknown displacement field in the BVP is reduced to a finite degrees of freedom, which are the nodal displacements at the nodal points of the FEs. However, the microscopic displacement field obtained of the solution of the RVE must satisfy the boundary conditions too.

When the *Taylor model* condition is considered there is not BVP to solve because of the displacement field on the total microscopic domain is constrained by the condition. However, for the case of

Linear boundary displacements condition a conventional BVP is obtained with a Dirichlet's condition on the whole boundary domain. For the cases of *Periodic boundary fluctuations* and *Minimal constraint* conditions the BVP to be solved have constraint boundary conditions.

The restrictions of degrees of freedom on the boundary domain can be accounted through several methods such as elimination of redundant unknowns, penalty methods and Lagrange multipliers [82]. The last two methods have the disadvantage that ill-conditioned stiffness matrix or increase the number of degrees of freedom of the problem.

To avoid these two disadvantages, it is proposed solving the RVE by an elimination of redundant unknowns [34]. The constraint condition for the *Periodic boundary fluctuations* is shown in Section 3.6.2 and it is possible to observe the redundant boundary unknowns of the BVP. In these boundary constraint expressions it is possible identify master unknowns (the unknowns to resolve) and slave unknowns. In the Appendix B.1 the master-slave kinematic relationships are derived the considered *Periodic boundary fluctuations* condition.

Linear implementation

Following a conventional notation, the FE approximation of the variational problem (3.90) for a given discretization h consists in the determination of the unknown vector $\bar{\mathbf{u}}_\mu \in \mathrm{V}^h_{\Omega_\mu}$ of the microscopic global nodal displacement such as

$$\int_{\Omega^h_\mu} \mathbf{B}^T : \mathbf{S}_\mu(\mathbf{B}\cdot\bar{\mathbf{u}}_\mu, \boldsymbol{\alpha})\; dV \cdot \bar{\mathbf{w}} = 0 \qquad \forall\; \bar{\mathbf{w}} \in \mathrm{V}^h_{\Omega_\mu}, \tag{3.93}$$

where Ω^h_μ denotes the discretized domain of the RVE, $\mathbf{B}$ is the global strain-displacement matrix (see Appendices B.3 and B.4), $\bar{\mathbf{w}}$ is the global vectors of nodal displacement fluctuation and $\mathrm{V}^h_{\Omega_\mu}$ is the set of finite-dimensional nodal displacement vectors associated with the FE discretization h of the RVE domain Ω_μ. For the linear case considered, the microscopic stress tensor is

$$\mathbf{S}_\mu = \mathbf{C}_\mu : \mathbf{E}_\mu = \mathbf{C}_\mu : \mathbf{B}\cdot\bar{\mathbf{u}}_\mu, \tag{3.94}$$

therefore, (3.93) can be written as

$$\left[\int_{\Omega^h_\mu} \mathbf{B}^T : \mathbf{C}_\mu : \mathbf{B}\; dV \cdot \bar{\mathbf{u}}_\mu\right] \cdot \bar{\mathbf{w}} = 0 \qquad \forall\; \bar{\mathbf{w}} \in \mathrm{V}^h_{\Omega_\mu}, \tag{3.95}$$

or

$$[\mathbf{K}\cdot\bar{\mathbf{u}}_\mu]\cdot\bar{\mathbf{w}} = 0 \qquad \forall\; \bar{\mathbf{w}} \in \mathrm{V}^h_{\Omega_\mu}, \tag{3.96}$$

where,

$$\mathbf{K} \equiv \int_{\Omega^h_\mu} \mathbf{B}^T : \mathbf{C}_\mu : \mathbf{B}\; dV. \tag{3.97}$$

Here, $\mathbf{K}$ is the global stiffness matrix.

However, (3.96) does not include the boundary constraint on the unknown nodal displacement field because of the *Periodic boundary fluctuations* condition as explained in the preceding section. The Section B.2.1 of the Appendix B.2 shows how the elimination of the redundant unknowns have been addressed in (3.96) to find the following system equation

$$\mathbf{K}_r \cdot \bar{\mathbf{u}}_r = -\mathbf{F}_r, \tag{3.98}$$

where, $\mathbf{K}_r$ is the reduced global stiffness matrix, $\bar{\mathbf{u}}_r$ the reduced global nodal displacements vector and $\mathbf{F}_r$ is a reduced global forces vector which is obtained as a result of the applied boundary restriction.

Non-linear implementation

The solution of the FE approximation of the microscopic variational problem given by (3.90) in the non-linear case is addressed by a Newton-Raphson iterative scheme. Therefore, the microscopic displacement field for a typical iteration (k) in the micro-scale is obtained according to the following update expression

$$\mathbf{u}^{(k)}_\mu = \mathbf{u}^{(k-1)}_\mu + \mathbf{d}^{(k)}_\mu, \tag{3.99}$$

where $\mathbf{d}^{(k)} \in \mathrm{V}_{\Omega_\mu}$ is the unknown iterative displacement field. Considering that the microscopic stress tensor can be obtained as

$$\mathbf{S}_\mu^{(k)} = \mathbf{S}_\mu^{(k-1)}(\mathbf{E}_\mu^{(k-1)}, \boldsymbol{\alpha}^{(k-1)}) + \delta\mathbf{S}^{(k)}, \tag{3.100}$$

and taking the following approximation

$$\delta\mathbf{S}^{(k)} \cong \mathbf{T}_\mu^{(k-1)} : \nabla^s \mathbf{d}_\mu^{(k)}, \tag{3.101}$$

with

$$\mathbf{T}_\mu^{(k-1)} \equiv \left.\frac{\mathrm{d}\mathbf{S}_\mu}{\mathrm{d}\mathbf{E}_\mu}\right|_{\mathbf{u}^{(k-1)},\ \boldsymbol{\alpha}^{(k-1)}} \tag{3.102}$$

denoting the microscopic tangent constitutive tensor. With the above at hand, and for the given discretization h the FE approximation of the microscopic problem consists in solving the unknown iterative (k) of the global nodal displacement vector $\bar{\mathbf{d}}^{(k)} \in \mathrm{V}_{\Omega_\mu}^h$ of the following equation

$$\begin{aligned}\Bigg[&\int_{\Omega_\mu^h} \mathbf{B}^T : \mathbf{S}_\mu^{(k-1)}(\mathbf{B}\cdot\bar{\mathbf{u}}_\mu^{(k-1)}, \boldsymbol{\alpha}^{(k-1)})\ dV \\ &+ \int_{\Omega_\mu^h} \mathbf{B}^T : \mathbf{T}_\mu^{(k-1)} : \mathbf{B}\ dV \cdot \bar{\mathbf{d}}_\mu^{(k)}\Bigg] \cdot \bar{\mathbf{w}} = 0 \qquad \forall\ \bar{\mathbf{w}} \in \mathrm{V}_{\Omega_\mu}^h,\end{aligned} \tag{3.103}$$

or

$$[\mathbf{F}^{(k-1)} + \mathbf{K}^{(k-1)} \cdot \bar{\mathbf{d}}_\mu^k] \cdot \bar{\mathbf{w}} = 0 \qquad \forall\ \bar{\mathbf{w}} \in \mathrm{V}_{\Omega_\mu}^h, \tag{3.104}$$

where,

$$\mathbf{F}^{(k-1)} \equiv \int_{\Omega_\mu^h} \mathbf{B}^T : \mathbf{S}_\mu^{(k-1)}(\mathbf{B}\cdot\bar{\mathbf{u}}_\mu^{(k-1)}, \boldsymbol{\alpha}^{(k-1)})\ dV, \tag{3.105}$$

and

$$\mathbf{K}^{(k-1)} \equiv \int_{\Omega_\mu^h} \mathbf{B}^T : \mathbf{T}_\mu^{(k-1)} : \mathbf{B}\ dV \tag{3.106}$$

is the global tangent stiffness matrix of the RVE.

Like in the linear case, (3.104) does not include the boundary constraint over the RVE boundary because of the *Periodic boundary fluctuations* condition. In the Section B.2.2 of the Appendix B.2 is shown how the following reduced system equation is obtained applying an elimination of redundant unknowns method in (3.104)

$$\mathbf{K}_r^{(k-1)} \cdot \bar{\mathbf{d}}_r^{(k)} = -\mathbf{F}_r^{(k-1)}, \tag{3.107}$$

where, $\mathbf{K}_r^{(k-1)}$ is the reduced global tangent stiffness matrix, $\bar{\mathbf{d}}_r^{(k)}$ the reduced iteration (k) of the global nodal displacements vector and $\mathbf{F}_r^{(k-1)}$ is the reduced global forces vector of the previous iteration.

3.7.2 Final remarks

In the following description is considered that the FE used in the macroscopic mesh has one integration point. The macroscopic finite volume Ω_M around the point $\mathbf{X}_o$ considered in the formulation is related now with the FE domain, then $\Omega_e = \Omega_M$, where Ω_e is the FE domain. Therefore, taking into account the exposed considerations in Section 3.5 can be conclude $\Omega_e = \Omega_\mu$ which means that, for one Gauss point FE, the RVE domain must be geometrically equal to the FE domain. Consequently, for an enhanced-first-order approach the RVE dimension is related with the discretization mesh used in the macroscopic BVP.

The macroscopic BVP presented in Section 3.6.1 does not take into account the homogenized second-order stress tensor $\hat{\mathbf{Q}}$ obtained in the enhanced-first-order homogenization. Besides, if a symmetric distribution of the simple materials within the RVE is taken, the estimated homogenized stress tensor is the same with both homogenization approaches. The change of the homogenization method does not improve the macroscopic results obtained since the proposed BVP. To improve the macroscopic results high-order FE or enhanced FE mesh must be considered. To consider the homogenized second-order stress tensor $\hat{\mathbf{Q}}$ in the macroscopic scale level a second-order macroscopic formulation must be used [54, 55, 31].

Linear FE in the macroscopic mesh

In first-order (or linear) finite element the interpolation functions (shape functions) are polynomials of first-order and consequently, the displacement field in the domain of the FE is a first-order function. The strain tensor (or the deformation gradient) is obtained by differentiating the displacement field, and then the strain tensor in the FE will be a constant function for this kind of element. Therefore, a good or fine FE mesh on the macroscopic BVP should be used to obtain an accurate approximation of the strains and stresses.

When linear finite elements with a first-order homogenization are used to solve the macroscopic problem the RVE is just a representative sub-domain of the periodic microstructure without special consideration about the real microscopic dimension. The constant valued of the macroscopic gradient tensor $\mathbf{F}$ in the integration point of the macroscopic FE is used to obtain BVP in the RVE. From the solution of the microscopic problem the macroscopic stress tensor is obtained for the considered integration point.

However, use the enhanced-first-order homogenization with linear finite elements in the macroscopic mesh is an inefficient procedure because the value of the numerical approximate of $\mathbf{G}$ in the integration point for this kind of element has partial or even zero information.

High-order FE in the macroscopic mesh

To improve the FEM approach high-order elements are used. The second-order (or quadratic) finite element uses second-order polynomials as interpolation functions to approximate the displacement field within the FE's domain. For this element, the deformation gradient tensor $\mathbf{F}$ obtained is a first-order function while gradient of the deformation gradient tensor $\mathbf{G}$ which is obtained deriving twice the displacement is a constant function on the FE domain.

The used of the enhanced-first-order homogenization needs at least quadratic elements in the macroscopic mesh because the approximated functions $\mathbf{F}$ and $\mathbf{G}$ have not zero value in the FE domain. Quadratic elements need more than one Gauss point to obtain the best integration approximation. As mentioned before, the RVE dimension must be related with the FE dimension in this enriched first-order homogenization. For quadratic elements the RVE must represent the sub-domain within the FE associated to the Gauss point. Because of the deformation gradient $\mathbf{F}$ is not a constant function on the Gauss point domain the RVE cannot be modeling with another periodic sub-domain of the microstructure. The microscopic results depend of the dimension of the RVE. Therefore, to obtain the best reachable approximation of the strain and stress fields using the enhanced-first-order approach (and high-order finite elements in the macroscopic mesh) the RVE geometry should represent the real volume of the surrounding domain in the Gauss point.

Chapter 4

Numerical comparison with other formulations

This chapter compares the results provides by these three numerical models (Micro models, Mixing and Homogenization approaches), looking into the strengths and weaknesses of each one of them. First, in the next section a brief description of Micro models and the Serial-Parallel theory, is done.

4.1 Numerical models used to simulate the microstructural's behavior

This section briefly describes the numerical models that will be compared with the homogenization framework.

4.1.1 Micro models

In these models, the constituent materials forming the composite are modeled explicitly. Therefore, the response of the composite arises naturally. Each single material is modeled with its own constitutive law. These models are very powerful because they do not need to take any hypothesis on the microstructural behavior. However, their biggest limitation is its computational cost and in most cases their use is not practical.

4.1.2 Serial-parallel mixing theory

The serial-parallel mixing theory could be defined as a phenomenological homogenization, where the behavior of the composite is obtained from the constitutive response of their materials components. This theory has been developed by Rastellini et al. [106], and is a natural evolution of the parallel mixing theory developed by Car et al. [11, 92]. The theory is based on the compatibility conditions defined by Trusdell and Toupin [123], but introduces a modification in the iso-strain hypothesis. The iso-strain condition is imposed in the reinforcement direction (normally fiber) and a new iso-stress condition is imposed in the transversal directions. The theory is based on the following hypotheses:

1. The constituent materials of the composite are subjected to the same strain in the parallel (fiber) direction.

2. Constituent materials are subjected to the same stress in the serial direction.

3. The response of the composite material is directly related to the volume fractions of its constituent materials.

4. The phases in the composite are considered to be homogeneously ditributed.

5. The constituent materials are considered to be perfectly bonded.

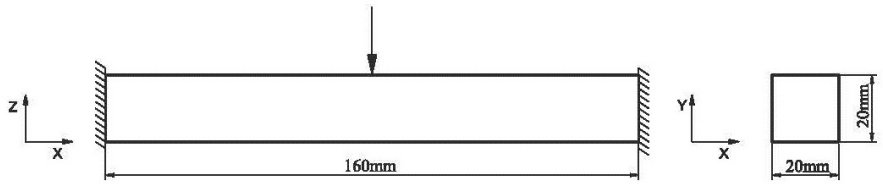

Figure 4.1: Geometric of the beam studied.

Taking only two composite components, the equations that define the stress (σ) equilibrium and setting up the strain (ε) compatibility between the individual components follow the hypothesis previously described are:

Parallel behavior:

$$\begin{aligned} {}^{c}\varepsilon_p &= {}^{m}\varepsilon_p = {}^{f}\varepsilon_p \\ {}^{c}\sigma_p &= {}^{m}k^{m}\sigma_p + {}^{f}k^{f}\sigma_p \end{aligned} \tag{4.1}$$

Serial behavior:

$$\begin{aligned} {}^{c}\varepsilon_s &= {}^{m}k^{m}\varepsilon_s + {}^{f}k^{f}\varepsilon_s \\ {}^{c}\sigma_s &= {}^{m}\sigma_s = {}^{f}\sigma_s \end{aligned} \tag{4.2}$$

where the superscripts c, m and f stand for composite, matrix and fiber, respectively and ${}^{i}k$ is the volume-fraction coeffiecient of each constituent in the composite.

This theory can predict the linear and non linear behavior of structural elements made of composite materials. Composite materials that can be modelled are those formed of long fibers embedded in a matrix. The theory predicts the different behavior of the composite, depending on the load direction. The potential of this theory is to predict accurately the response of composites in the linear and non linear range (i.e. delamination failure) as has been proved in several papers [73, 106, 71, 70, 69, 100, 72, 101]. On the other hand, The theory of seriel-parallel mixtures is able to simulate the delamination problem naturally, without having to define specific elements or predefine the path of fracture.

4.2 Model description

A clamped beam with a vertical load at mid-span is the structure used to compare the theories presented previously: micro model, serial-parallel mixing theory and homogenization. Figure 4.1 shows the beam's geometry, supports and loads. A macro numerical model will be used to simutale the behavior of the structure with the diffrent theories. In the special case of the homogenization theory another micro numerical model it is necessary. The micro numerical model will have the internal composite's structure.

4.2.1 Macro and micro numerical model

The macro FEM model used is the half of the beam because the symmetry of the structure (see Figure 4.1). Figure 4.2 shows the macro numerical model with one of the meshes used. The finite element used is a first order hexahedra element. In order to obtain the real behaviour of the structure with the FE model it is necessary to impose symmetric boundary conditions. The symmetry plane, the right face of Figure 4.2, normal to X-axis, and the X displacement is set to zero in this face. To simulate the fixed support, the nodes' movements in the left cross section are also restricted. The applied load is a Z direction fixed displacement of -0.1 mm in the rigth cross section nodes (symmetry plane).

As said before, to simulate the RVE in the homogenization theory a micro numerical model is used. The RVE's geometry chosen is a cube with unit length sides. The finite element used is the same than the macro numerical model. The different RVE models that will be used are shown in the Figs. 4.3 and 4.6.

4.2.2 Simple materials and composite description

The simple materials in all studied cases are isotropic elastic materials. The composite material is a laminate. And, the laminate consists of several layers of material 1, called lamina 1 henceforth, and a

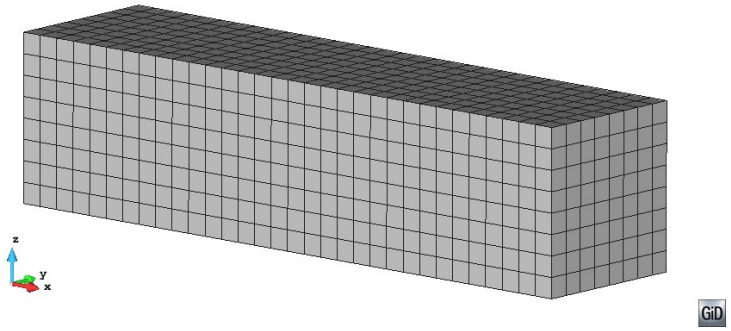

Figure 4.2: Beam numerical model

Simple mat.	Color ref.	E (GPa)	G (GPa)	ν
Lamina 1	Black	210	80.76	0.3
Lamina 2	Grey	3.5	1.46	0.2
Lamina 3	White	3.5	0.146	0.2

Table 4.1: Mechanical properties of the simple materials

conbination of layers of material 2 (lamina 2) or material 3 (lamina 3). The volumetric participation of lamina 1 is always a 50%.

Table 4.1 contains the mechanical properties of all the materials considered in the composite. In this table, E is the Young's modulus, G is the Shear modulus and ν is the poisson's ratio. The "Color ref." is the color used to represent the material in the RVEs, as it is shown in Figs. 4.3 and 4.6. The lamina 3 has the same properties as lamina 2, with the only difference of the shear moduluss, which is reduced by 10. This is done to emulate the effect of a degradated lamina 2.

4.3 Comparison for several material configurations

In this section, several examples are presented to compare the behavior of the different theories. The result used to compare them is the reaction force, in Z direction, at the fixed support obtained for a fixed Z displacement applied at the symmetry plane (See Figure 4.1) .

4.3.1 Undamaged case

The undamaged case is the first one used to compare all theories. In this case the laminate contains 50% of lamina 1 and 50% of lamina 2, which properties are defined in Table 4.1.

The model using the SP mixing theory defines the composite material assuming that the parallel behavior is obtained in X and Y direction, while the rest of directions have a serial behavior. The homogenization theory uses a RVE made with 8 elements that also contains 50% of lamina 1 and 50% of lamina 2. The RVE is shown in the following Figure 4.3. Finally, the micro-model is defined discretizing the different layers in which the laminate is divided.

A convergence analysis of SP and Homogenization theories has been made. The quantity of finite elements in the macro-model FE mesh has increased until the difference, between two consecutive results, is negligible. Figure 4.4 presents the results obtained for the different meshes analysed. The micro-model used to compare the results obtained with the different theories has been made with 196608 hexahedron elements, which results in 648999 degrees of freedom.

The reaction force obtained with the SP theory is 905.9 N, with the homogenization is 908.3 N and with the micro-model is 919.0 N. It can be concluded that the three theories provide almost the same result, as the difference between the reaction force value is lower than a 1% which is really good result. Besides, all theories allow knowing not only the global performance of the beam analyzed, but also the specific response of each lamina to the loads applied.

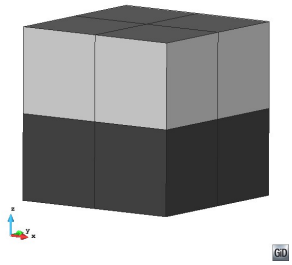

Figure 4.3: RVE used for the undamaged case.

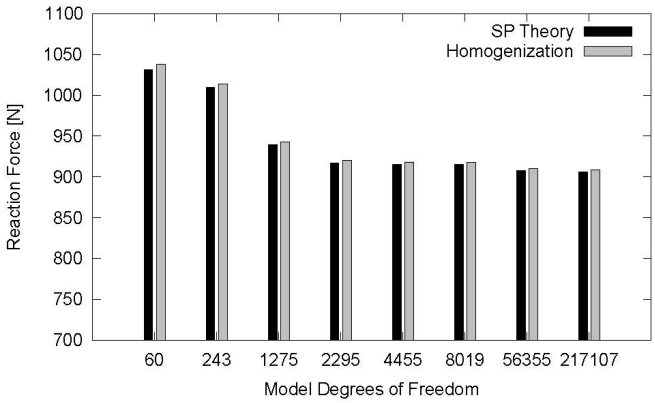

Figure 4.4: Convergence analysis results.

4.3.2 Global damage case

The objective for this example is to compare the responses obtained when one of the laminate materials suffers some sort of degradation. To analyze this problem, five different simulations have been performed in which the mechanical properties of one of the laminates is reduced. More specifically, the degradation is applied on the shear strength of lamina 2, which is reduced progressively until reaching the value of lamina 3 (see Table 4.1). Therefore, the new laminate consists 50% of lamina 1 and 50% of a new lamina that can be completely undamaged (properties of lamina 2) or with properties corresponding to 12.5%, 25%, 50% and 100% of damage (this last case, corresponds to lamina 3). The specific mechanical values considered are shown in Table 4.2.

The composite is simulated with the SP mixing theory and with the homogenization theory, using the same material characterization and RVE that were used in the undamaged case. Figure 4.5 shows the results obtained for the conducted simulations. This figure shows that, as it is expected, the results obtained for both theories are again exactly the same. The results obtained also show that as the shear stiffness of one of the layers is reduced, the global stiffness of the beam decreases. This effect can be understood as a delamination failure, as has been previously shown by Martinez et al. [70, 72]. Results also show that the reduction of global stiffness of the beam is not linear with the reduction of the shear strength of one of the laminas, being larger as the layer stiffness gets smaller.

Property	12.5%	25%	50%	100%
G (GPa)	1.295	1.131	0.803	0.146
E (GPa)	3.5	3.5	3.5	3.5

Table 4.2: Mechanical properties of the degradated Lamina 2

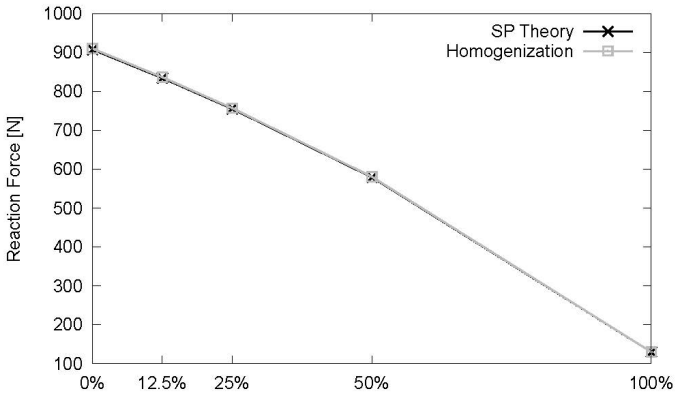

Figure 4.5: Reaction force obtained in the global damage case.

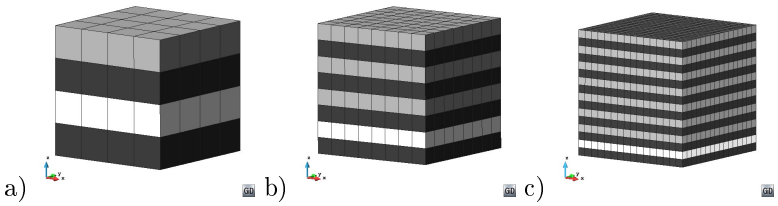

Figure 4.6: RVEs containing 50%, 25% and 12.5% of damaged layers.

4.3.3 Local damage case

In this example, the objective is to compare the responses obtained when material damage takes place, not in all layers, but just in some of them. The composite considered has always 50% of lamina 1, and a 50% of lamina 2 (undamaged and damaged). It is assumed, like in the previous case, that a totally damaged lamina 2 is numerally represented by the lamina 3. The comparison is made for the cases in which there are 0%, 12.5%, 25%, 50% and 100% of layers damaged. The simulation corresponding to 0% and 100% damaged have been already conducted in two previous simulations. The simulations corresponding to intermediate cases have been studied with the three methods being compared in this work: homogenization, SP and a micro-model.

For SP theory, the composite is obtained combining two different laminates with the SP formulation. One laminate has 50% of lamina 1 and 50% of lamina 2 and the other laminate has 50% of lamina 1 and 50% of lamina 3. The volume fraction of these laminates in the composite depend in the amount of layers assumed to be damaged. For the homogenization theory, the amount of layers damaged is represented with the RVE. Figure 4.6 shows the RVEs considered to account for 50%, 25% and 12.5% of damaged layers, respectively. In this figure, the darker elements correspond to lamina 1, the light-grey elements correspond to lamina 2 (undamaged) and the white elements correspond to lamina 3 (damaged). Finally, the micro-model has been simulated discretizing each one of the lamina of the beam.

Figure 4.7 presents the results obtained with different simulations performed. This figure shows that for the extreme cases, this is for 0% or 100% of lamina 3, the results obtained with differents theories are almost equal. However, the results obtained when there are some layers damaged do not have the same agreement, especially when comparing the results obtained with the SP theory with the ones obtained with the homogenization method or the micro-model. While the decrease in the resultant reaction force with the SP theory is equal to the one obtained in the case of considering global damage (see Figure 4.5), this decrease is substantially larger when considering the homogenization method or a micro-model. These two theories provide nearly the same results.

The explanation for the difference in the response obtained for the different models is obtained from the models themselves. The serial-parallel theory obtains the response of the composite assuming certain iso-stress and iso-strain boundary conditions that regularizes the response of the material if it is defined with several laminates. Therefore, the response of the structure and the result obtained is similar to

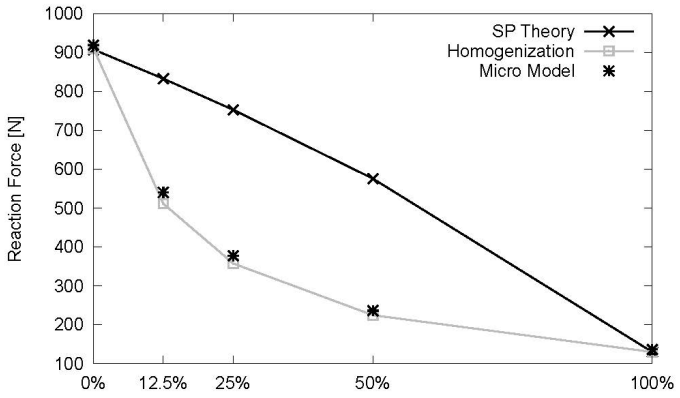

Figure 4.7: Reaction force obtained in the local damage case.

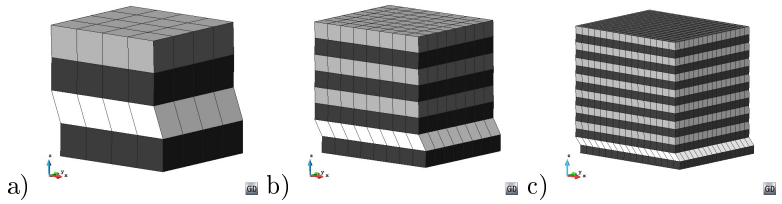

Figure 4.8: RVEs with 50%, 25% and 12.5% of damaged layers under load.

the one obtained when this damage was present in the whole structure. On the other hand, with the homogenization and the micro-model theories, the damaged layer is discretized specifically and it is possible for the simulation to capture the dislocation that takes place, as it is shown in Figure 4.8 for the three cases considered. This dislocation is the responsible for the drop of the stiffness and the fast decrement on the value of the reaction obtained.

4.3.4 Local damage case in a localized region of the beam

At the light of previous results one may think that the SP theory is not capable of representing delamination processes. In this example it is shown that under some circumstances this simulation is possible. Here, the beam has been simulated with two diffent laminates. The central band contains 50% of lamina 1 and 50% of lamina 3 (damaged); while the rest of the beam is simulated with 50% of lamina 1 and 50% of lamina 2. Figure 4.9 shows the FE mesh of the beam macro-model. This example is simulated with the SP and the homogenization theory. The homogenization theory uses the RVE shown in Figure 4.3.

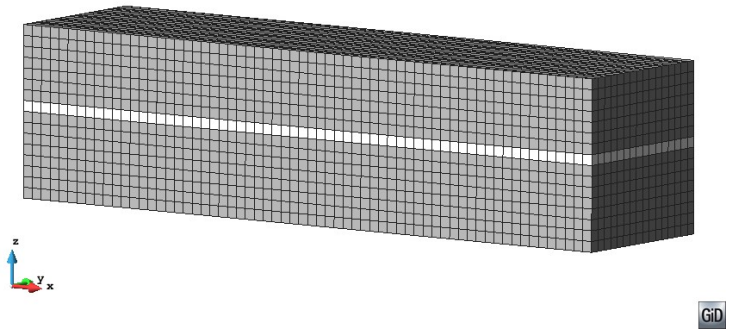

Figure 4.9: FE mesh of the macro-model of the beam with two laminates.

Item	Micro Model	H-OneRVE	H-AllRVE	SP Theory
Real Time [Min:Seg]	6:46	0:01	2:27	0:02
CPU Time [Min:Seg]	8:44	0:03	9:31	0:17
Memory [Mbytes]	2690,00	7,45	7,45	15,82
Reaction Force [N]	236,09	224,69	224,69	576,68

Table 4.3: Times and memory used to 50% located damage case.

In this case, the reaction force obtained is exactly the same for both, the SP and the homogenization models: 663.9 N and 666.4 N, respectively. This example shows that the SP theory is capable of providing the same results as the homogenization theory when the response of the RVE fulfills the parameters in which is based the SP theory: iso-strain and iso-stress behavior. On the other hand, if the RVE does not fulfill this behavior (i.e. there is a dislocation in it), the SP theory is not capable of predicting accurately the material response, as it was shown in previous example.

4.4 Run times and memory used

One of the main drawbacks that has a homogenization formulation nowadays is its computational cost. Therefore, in order to know the performance of this formulation it is necessary not only to compare the results obtained with it, but also to compare the computational cost in terms of time and memory requirements.

To do these comparisons, in the case of the homogenization theory, two different strategies have been considered. In the first one, the mechanical properties of the composite (stiffness matrix) are calculated at the beginning of the analysis, and these porperties are used afterwards during the complete of the simulation. This case is named H-OneRVE. The other case corresponds to analyze the RVE each time that it is necessary to know the stress provided by the RVE for a given strain value. This case is named H-AllRVE. If the problem is linear, the results obtained in both cases are the same. However, in a non linear case, it is necessary to simulate the problem with an H-AllRVE strategy in order to capture properly the non linear response of the material.

Table 4.3 shows the computational times and memory required to conduct the simulations with a localized damage of a 50%. The real time and cpu time are discriminated because part of the FE code used is in parallel. The results show that the CPU time in the Micro model and H-AllRVE are comparable. But, the CPU time of the H-OneRVE and SP theory are significantly better. Therefore, in terms of computational time, it is feasible to conduct a simulation with a homogenization theory, as well as with the SP theory. However, this simulation must be kept in the linear range. If the simulation is non linear, the H-AllRVE strategy must be used, which makes the SP theory the only feasible option in terms of computational time.

The main difference between the micro-model and the homogenized model is found in the memory requirements. While the computational time of the H-AllRVE and the micro-model are equivalent, the amount of memory required by this last one is substantially larger (360 times larger). This difference is found because the memory used is proportional to the FE mesh size of the numerical model and, while the micro-model has to solve a problem with a very small discretization, the homogenization theory only requires memory for the macro-problem and the RVE that is being solved. This difference makes unbearable solving large problems with micro-models and makes feasible using homogenization methods, even if the problem is in non linear range.

Chapter 5

Non-linear extension proposed for multiscale methods

Most of the work on FE^2 multiscale procedures are done on analyzing the numerical performance of RVE [129, 105] or on connecting different scales [32]. In general, in this kind of homogenization methods the elastic properties of the microstructure are obtained solving the microstructural problem at the beginning of the structure problem. However, the problem with these methods is their computational cost for a non-linear analysis because it is required solving the RVE in every integration point at the macrostructural problem and for every time step to know the non-linear limit and then the behavior of the microstructure in non-linear range. Non-linear performance has also the problem that the dissipated energy of both scales is not always related [5].

In order to improve the computational cost of the multiscale homogenization some strategies use model-order reduction techniques [134, 86, 43]. These methods use the Proper Orthogonal Decomposition (POD) to obtain the reduced set of empirical shape functions. Besides, [43] proved that the common approach of replacing the non-affine term by an interpolant constructed taking only POD modes arrives to ill-posed formulations. An enriched approximation space with the span of the gradient of the empirical shape functions is proposed to avoid this ill-posedness. However, these kind of procedures do not solve the complete structure.

Because of this, in the following a new procedure to reduce computational cost of multiscale simulation. The chapter looks also into the problem of localization and energy dissipation across the scales, as the proposed method must be consistent [1]. In the following the formulation and algorithm schemes of the proposed procedure is described.

5.1 Introduction

The main advantage of the FE^2 method related to a micro model is the reduced computer memory requirements. To solve the same problem, the amount of memory required by the classical FE micro model method is substantially larger than FE^2 procedure. This difference is found because the memory used is proportional to the FE mesh size and, while the FE micro model has to solve a problem with a very small discretization, the FE^2 procedure only requires memory for the macrostructural problem and the RVE that is being solved. However, if the material reaches non-linear behavior, the computational cost of FE^2 method becomes as large as the one required by the micro model case, as the RVE has to be solved for each integration point when a real structure is solved. Because of this, a new Non-Linear Strategy (NLS) is proposed in this work.

Continuum mechanics establishes the limit between linear and non-linear performance of materials using comparison criterion that compares a given combination of stresses with a threshold value (Von-Mises, Mohr-Coulomb, etc.). This approach cannot be used in an homogenization double scale solution directly as different strain-stress states may lead to different failure modes of the composite.

A possible solution is to analyze the RVE at every time step. However, this is extremely expensive and very ineffective, because the structural non-linear behavior often occurs in a small part of its domain.

5.2 General concepts of the proposed approach

Here is proposed to develop a comparison function that looks a maximum level of an elastic energy density that can be applied to the RVE before its failure. This is done with the definition of an activation function for each single integration point at the structural scale. It is important to remark that the proposed approach does not use a model reduction strategy, instead it is solving the actual structure, but only when it is strictly necessary.

The NLS is composed of two different procedures, a non-linear activation function and a smart first step calculation. In the following are defined both of them.

5.2.1 Non-linear activation function

The definition of a Non-Linear Activation Function (NLAF) is based on the fact that any given material begins its non-linear performance when a single particle of the material reaches its stress threshold. The objective of the NLAF is to know whether any material point of the RVE has reached its non-linear limit using homogenized variables.

To do so, it is defines a function f that relates the elastic energy density (Ψ^e) of an integration point of the RVE with the maximum elastic energy (Ψ^e_{Limit}) that can be applied to this material point, before reaching the non-linear range. Therefore, f is defined as

$$f = \frac{\Psi^e}{\Psi^e_{Limit}} \quad , \quad 0 < f < 1. \tag{5.1}$$

In other words, f provides a value of how far is a material point in the microstructure to reach the non-linear state.

In order to know how far is the whole RVE to reach the non-linear performance, it is necessary to use the information obtained for all the integration points of the RVE and transform it into a single representative number. This is done with the assumption stated before that the failure of the macrostructure will start when the first integration point of the microstructure fails. Therefore, the $\bar{f}$ parameter of the RVE corresponds to the maximum f value of all integration points of the RVE. Then

$$max\{f_1, ..., f_n\} = \bar{f}, \tag{5.2}$$

where the overline at the variables refers to the structure scale or homogenized variables. Finally, the limit elastic energy density at the macrostructure scale is obtained with the following expression

$$\bar{\Psi}^e_{Limit} = \frac{\bar{\Psi}^e_1}{\bar{f}}, \tag{5.3}$$

where $\bar{\Psi}^e_1$ is the elastic energy density for the strain state used to calculate $\bar{f}$. The process described can be schematized as it is shown in Figure 5.1.

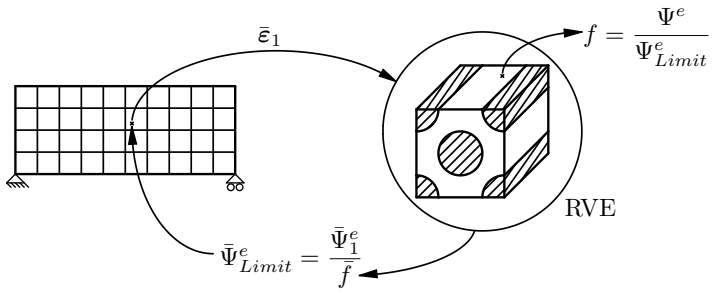

Figure 5.1: Non-linear activation function scheme.

The NLAF is defined as

$$\bar{\Psi}^e - \bar{\Psi}^e_{Limit} \leq 0, \tag{5.4}$$

where $\bar{\Psi}^e$ is the elastic energy density of the macro structural integration point, which is calculated in each load step of the simulation.

The NLAF is valid only for the strain state used to calculate $\bar{\Psi}^e_{Limit}$ (see (5.3)). If the strain state varies, it may also change the non-linear mode and, therefore, the limit elastic energy density calculated may be no longer valid. Therefore, (5.4) is valid while the strain state in the material remains proportional to the one used to obtain $\bar{\Psi}^e_{Limit}$. To quantify this proportionality the next expression is proposed

$$\frac{\bar{\boldsymbol{\varepsilon}}_1 : \bar{\boldsymbol{\varepsilon}}_i}{\| \bar{\boldsymbol{\varepsilon}}_1 \| \| \bar{\boldsymbol{\varepsilon}}_i \|} = 1 \quad \Longleftrightarrow \textit{Comparable States}, \tag{5.5}$$

where the subscript i refers to the current i-nth deformation state and $\| \, . \, \|$ is the norm's mathematical symbol. In case this proportionality is lost, it will be required to calculate again the new limit elastic energy density of the RVE. This is summarized in the following flow diagram (see Figure 5.2).

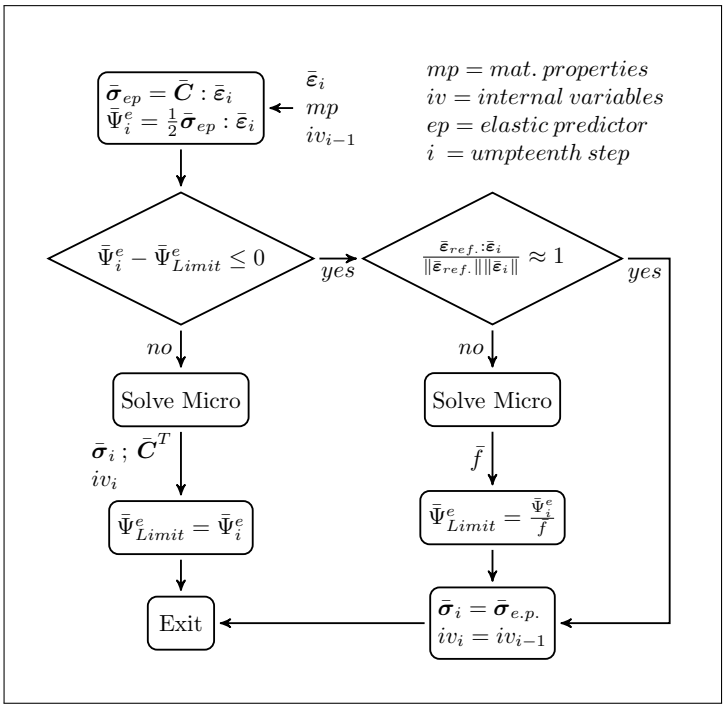

Figure 5.2: Non-linear strategy algorithm scheme.

It can be easily seen that with the proposed procedure the RVE must be solved for each macro integration point on the first time step, in order to calculate the elastic energy density limit using (5.3). Afterwards, it only will be necessary to solve the RVE again if the strain state of the integration point becomes non proportional to the calculated originally or if the NLAF is not satisfied, which means that the RVE becomes non-linear. Therefore, if only few elements of the structure reach the non-linear state, only these elements will have to be solved in the non-linear analysis.

5.2.2 Smart first step

As said before, at the beginning of the analysis it is required to solve the RVE for every single integration point of the macrostructure to obtain its $\bar{\Psi}^e_{Limit}$. This calculation process can be extremely expensive in terms of computational cost.

In order to reduce this computational cost, it is proposed a Smart First Step (SFS) strategy. This strategy consist in solving the RVE only if the deformation applied to it is different to all other deformation states considered previously. Therefore before calculating the $\bar{\Psi}^e_{Limit}$ of the RVE, the SFS procedure compares the deformation between the current and the all previous integration points already calculated (see (5.5)). If the SFS finds one comparable strain state, the current RVE takes the values of the RVE already solved. If none of the previous microstructures solved have a comparable state, the actual RVE is calculated. Figure 5.3 shows the scheme of the described algorithm.

It will be shown, in the validation examples, that this procedure reduces significantly the computational cost of the first step load in the simulation.

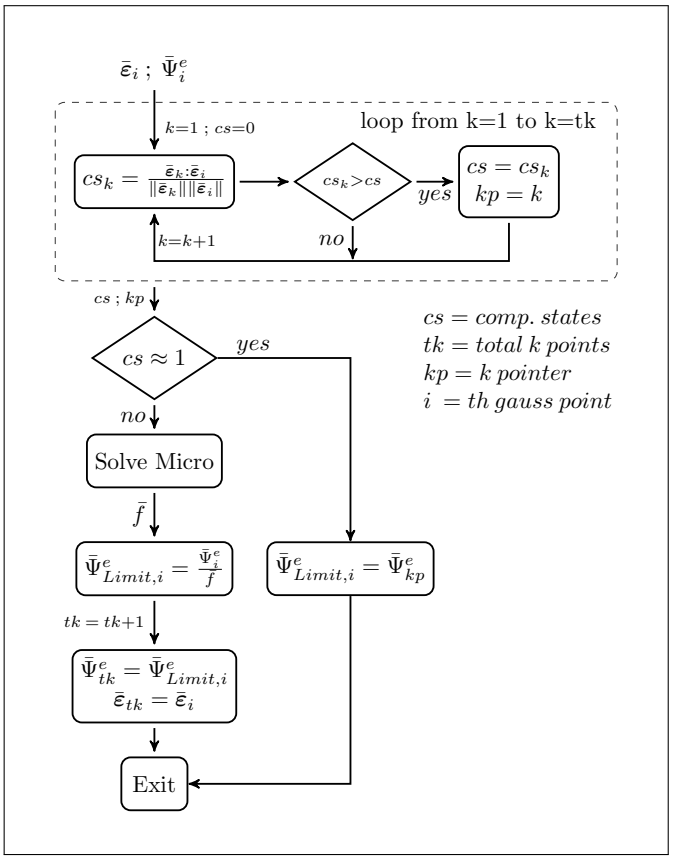

Figure 5.3: Smart first step algorithm scheme.

5.2.3 Numerical homogenized tangent constitutive tensor

The proposed NLS has been implemented in PLCd [103], a parallel finite element code that works with 3D solid geometries. In the code, a Newton-Raphson scheme is adopted to solve the non-linear problem. To facilitate the convergence of the whole problem, the tangent constitutive tensor at the integration point is necessary to obtain the global tangent stiffness matrix.

A perturbation method is used to obtain a numerical approximation of the homogenized tangent constitutive tensor of the RVE in the integration point. The method implemented is analogous to the one proposed by Martinez et al. in [71] (see B.5). Being the only difference that in current procedure the perturbations must be applied on the RVE instead of applying them to a constitutive equation. The n small perturbations ($\delta\bar{\boldsymbol{\varepsilon}}_j$) are applied to the homogenized or structural strain vector. The RVE is solved n times and as result gives the n stress vector $\delta^j\bar{\boldsymbol{\sigma}}$. Therefore, the j columns of the tangent constitutive tensor for the RVE can be obtained as

$$\bar{\boldsymbol{C}}^t_j \equiv \frac{\delta^j\bar{\boldsymbol{\sigma}}}{\delta\bar{\boldsymbol{\varepsilon}}_j}. \tag{5.6}$$

The calculation of the tangent stiffness tensor is necessary to obtain a good convergence of the problem but it is computationally expensive. This shows again the necessity to reduce the number of times in which this calculation is performed, and proves the necessity of having a non-linear strategy to conduct the simulation.

5.3 Energy dissipation in a multiscale analysis

The solution of material non-linear problems with a numerical double scale homogenization procedure not only should be affordable computationally, but the results obtained in the non-linear process must be also correct. Therefore, the procedure must dissipate the same energy in both scales. In order to conserve the dissipated energy through the scales, the following methodology is proposed.

5.3.1 Fracture energy

Fracture mechanics presents the fracture energy per unit of area, G_f, as a property of the material. This energy can be calculated as

$$G_f = \frac{W_f}{A_f}, \tag{5.7}$$

where, W_f is the energy dissipated by the fracture at the end of a quasi-static process, and A_f is the total fractured area. This fracture energy is the link between the fracture mechanics and the constitutive model based on classical solid mechanics. The constitutive model must satisfy:

The good representation of behavior of a set of points inside of a finite domain.

The same energy dissipated by the total volume as the one dissipated by the solid in the real fracture process.

Considering a simple tensile test, the constitutive model must verify the following condition of dissipation

$$\underbrace{W_f = G_f A_f}_{Fracture\ Mechanics} \quad \equiv \quad \underbrace{\Pi^d = \int_v g_f dV}_{Solid\ Mechanics} \tag{5.8}$$

where g_f is the maximum specific energy dissipated by the constitutive model. Equation (5.8) states that the energy delivered to the tensile test must be equal to the energy dissipated by the constitutive model. In solid mechanics, the dissipation phenomena is located in a volume that can be represented as $V_d = A_f L_f$, where L_f is a fracture length. For FE method the localization phenomena in one strip of finite elements is sought, therefore L_f is commonly approximated by some reference length of the finite element. This length is a parameter that accounts for the amount of energy dissipated by the fractured material. Replacing the volume V_d in (5.8) the following expression is obtained

$$W_f = G_f A_f = g_f A_f L_f. \tag{5.9}$$

From (5.9) the relation between the material parameter G_f and the specific energy dissipated g_f is found

$$g_f = \frac{G_f}{L_f}. \tag{5.10}$$

5.3.2 Localization at the microstructural scale

In multiscale procedure, the specific energy at the macro structural scale is obtained as

$$g_f = \frac{1}{V_m} \int_{\Omega_m} g_f^m dV_m, \tag{5.11}$$

where the index m is used to reference the microstructural scale variables.

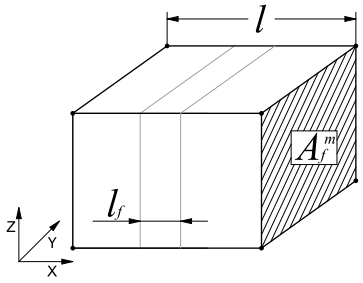

Figure 5.4: Representative volume of the subscale.

Taking the same consideration than macroscale solid behavior, now the dissipation phenomena is located at microstructural level (see Figure 5.4). In such case, we have the following dissipated equation

$$g_f = \frac{1}{A_f^m l} g_f^m A_f^m l_f, \tag{5.12}$$

where, A_f^m is the RVE cross section area, l is the length in normal direction of A_f^m and l_f is the fracture length at the microstructure (RVE). With (5.12) is possible to obtain the specific energy g_f^m dissipated at the microstructural scale level as

$$g_f^m = \frac{g_f l}{l_f} = \frac{G_f l}{L_f l_f}. \tag{5.13}$$

Equation (5.13) shows the relationship between the g_f^m and G_f which ensures to dissipate the same energy by the solid mechanics, using a multiscale method, than the one obtains with a tensile test. The validity of this relation is proved in the following example.

5.3.3 Validation example

A simple tensile numerical test over a material sample is simulated. The objective of this example is to analyze the objectivity of the response obtained using the proposed FE^2 method. The same test using a classical one scale FE method is also solved for comparison purposes. The geometry, the supports and the displacements scheme of the simulated structure is presented in Figure 5.5. The applied fixed displacement is represented by the arrows in the figure.

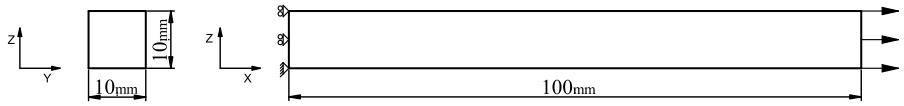

Figure 5.5: Structure simulated in the tensile test.

Material

The simple material used in the tensile test takes the properties shown in Table 5.1. The constitutive model chosen is an explicit scalar damage model with exponential softening [115, 90]. For this particular case, where the stress state is uniform and there is only one simple material, and in order to help the localization of the softening problem, the elastic limit is increased in some elements (drawn with gray color in Figure 5.6) up to a value of $\sigma_{Limit} = 102$MPa.

Properties	E [GPa]	ν [−]	σ_{Limit} [MPa]	G_f [kJ/m^2]
Values	100	0	100	20

Table 5.1: Simple material properties used in the tensile test.

FE meshes

The finite element employed to solve the problem is a first order hexahedra element. The example is solved for different combinations of finite element meshes. Figure 5.6 shows the different mesh sizes used in the simulation. The left side of Figure 5.6 shows the three different meshes used for the structural scale. The mesh Macro1 has 10 finite elements, the mesh Macro2 has 84 elements and finally the mesh Macro3 has 656 elements. On the other hand, the right side of Figure 5.6 shows the two different meshes used for the microstructural scale. The mesh Micro1 has 125 finite elements and the mesh Micro2 has 729 elements.

Results

The results obtained with the different mesh combinations are shown graphically in the Figure 5.7. As can be observed from the figure, the results are equal for all combinations, and for both methods.

For the case considered, it is possible to validate the numerical results with analytical calculations, knowing the area of the specimen, the Young's modulus and the maximum tensile stress that can be applied, the maximum load and displacement in the beam is

$$F_{max} = \sigma_{Limit}.A = 10\text{kPa},$$
$$d_{F_{max}} = \frac{L.\sigma_{Limit}}{E} = 0.1\text{mm}.$$

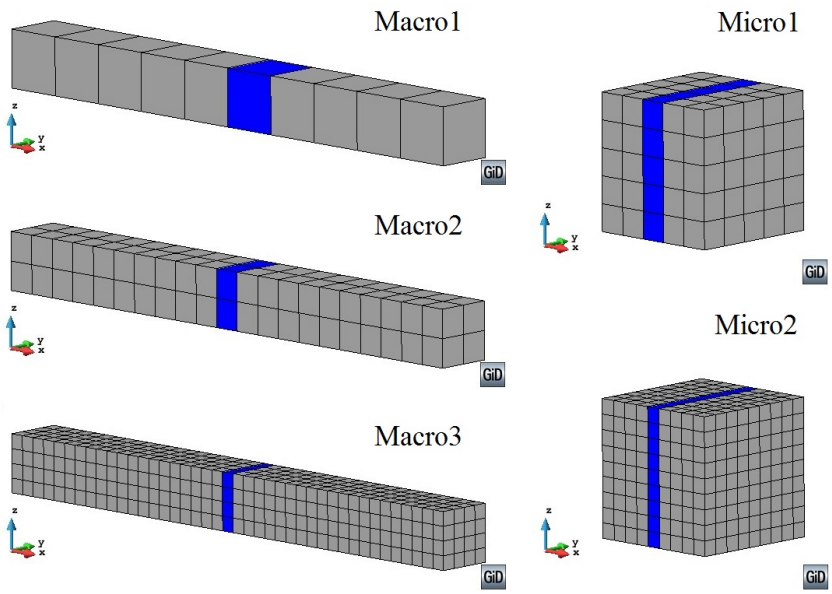

Figure 5.6: Different meshes used in the tensile test.

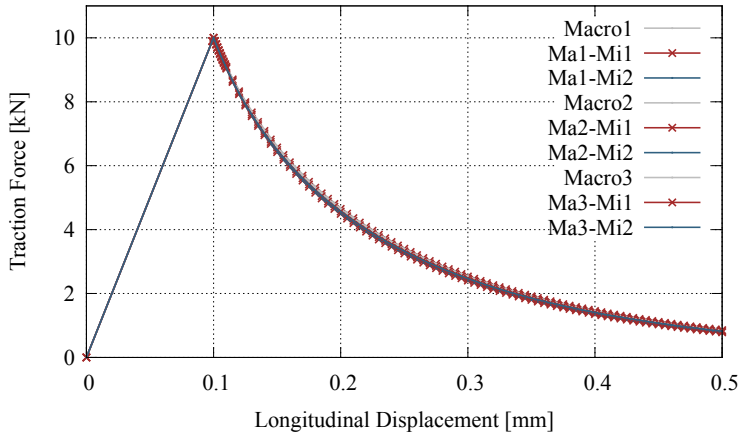

Figure 5.7: Traction force vs displacement curves obtained in the tensile test.

It is also possible to calculate analytically the dissipated energy at the end of the test as

$$W_f = G_f.A = 2\text{J}.$$

If this energy is calculated from the numerical models, the following table is obtained:

The difference between the estimated value and the ones show in Table 5.2 is because at the numerical analysis the simulation has been stopped at 0.5mm. It has to be noted also that the dissipation obtained with all mesh configurations is practically the same. Which proves the consistency of the formulation proposed.

The localization of non-linear phenomena in one strip of finite elements at the structural scale is shown in the Figure 5.8, for the analysis made with Macro2 mesh. This figure shows that damage is concentrated in the central zone of the material sample, and therefore, the displacement too. In the proposed multiscale method the localization phenomena must be observed also at the microstructural scale. As an example, Figure 5.9 shows the microstructural displacement and damage obtained at the end of one tensile numerical test. In the figure can be observed that both results are localized in one strip of finite elements in the RVE meshes.

Energy [J]	Macro1	Macro2	Macro3
One scale	1.728	1.737	1.748
Micro1	1.752	1.741	1.777
Micro2	1.713	1.761	1.812

Table 5.2: Dissipated energies obtained in the tensile test.

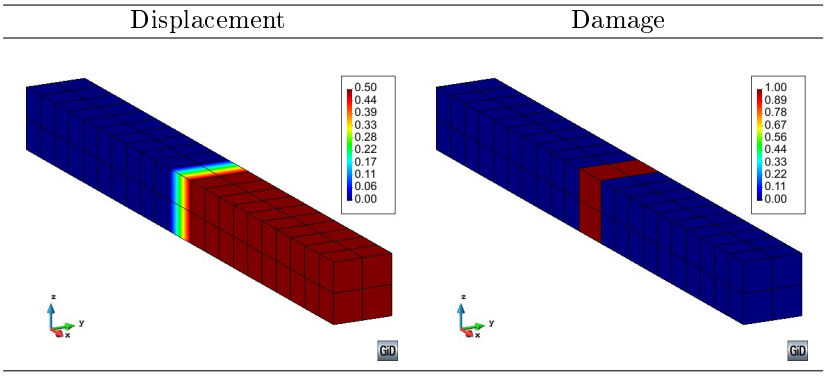

Figure 5.8: Macrostructural results obtained at the end of the tensile test.

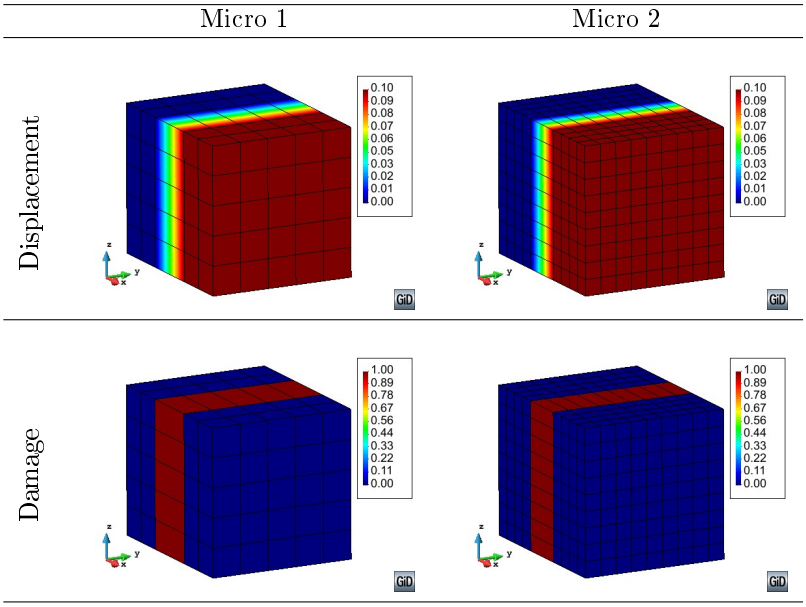

Figure 5.9: Microstructural results obtained at the end of the tensile test.

5.4 Numerical examples of non-linear analyses

5.4.1 Tensile test of a plate with a hole.

The objective of this example is to show the performance of the NLS developed, as well as to analyze the failure of the structure localizes in a strip of elements. The test is a tensile test made on a plate with a hole in its center. Due to the symmetry of the geometry and of the load applied, only a quart of the real structure is simulated. Figure 5.10 shows the modeled geometry, the supports and the displacements scheme in the numerical model. The applied fixed displacement is represented by the arrows in Figure 5.10.

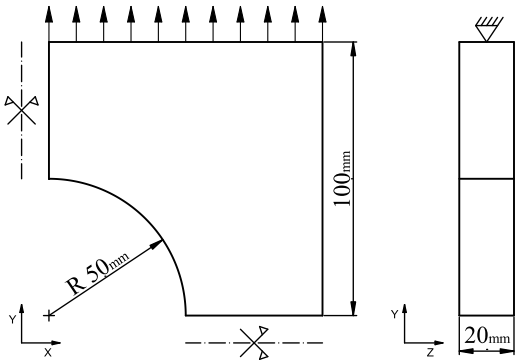

Figure 5.10: Simulated structure of the plate with a hole.

Material

Table 5.3 shows the properties of the simple material used. The constitutive model of the material is the same (explicit scalar damage) that has been used in the previous validation example 5.3.3.

Properties	E [GPa]	ν [−]	σ_{Limit} [MPa]	G_f [kJ/m^2]
Values	100	0.15	100	10

Table 5.3: Simple material properties used in the plate with a hole.

FE meshes

To analyze the response's objectivity in the test, two finite element meshes have been used for the macroscopic model. Figure 5.11 shows the mesh sizes employed. Mesh1 has 360 finite elements while Mesh2 is more dense and has 2880 elements. The microstructural model and finite element meshes are the same than the ones used in previous validation example 5.3.3.

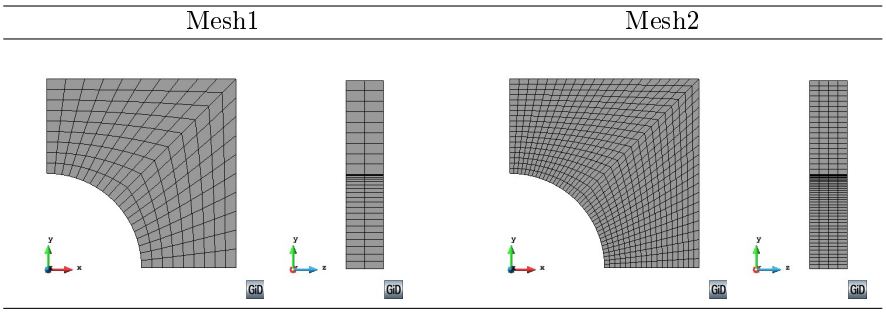

Figure 5.11: Different meshes used in the plate with a hole.

Results

Figure 5.12 shows the traction force vs displacement curves obtained for the different mesh combinations. This figure shows that the results are almost equal. Therefore, the result obtained with the proposal method is mesh independent. The curves show than the maximum force does not pass of 80kPa and it is obtained for an applied displacement of 0.08mm.

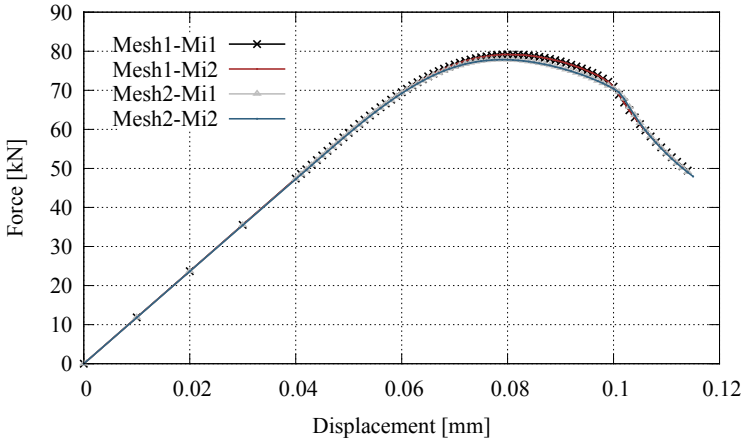

Figure 5.12: Forve vs Displacement for the plate with a hole.

The dissipated energy for the different mesh configurations used in this example is shown in Table 5.4. From the Table 5.4 can be observed than the worst difference between two results is less than 2%.

Energy [J]	Mesh1	Mesh2
Micro1	3.152	3.135
Micro2	3.192	3.169

Table 5.4: Dissipated energy in the plate with a hole.

To fully understand the behavior of the structure under the applied load several figures for different load state are presented. Figure 5.13 and Figure 5.14 show the results obtained for Mesh1 and Mesh2, respectively. In the figures, strain and stress in Y direction and scalar damage are presented for four different fixed displacement steps.

The figures show how at the beginning of the test (label a) d=0.05mm), the maximum strain and stress are located at the inner border of the hole. Then, the non-linear process starts there and, as a consequence, the damage increases in that zone. Due to constitutive model used, when the damage increases in the material the stress decreases. As the applied displacement continues increasing, the structure transfers the load to non damaged zones. Therefore, the zone with maximum stress moves from the inner border to the central part and the strain and damage move on as a constitutive response. At the end of the test (label d) d=0.11mm in the figures), the maximum stress is located in the right external border of the plate. It is important to mention that during the test, the stress in the structure never takes values over the limit imposed (see Table 5.3) as can be observed in Figures 5.13 and 5.14. Finally, the figures show how the model is capable of localizing all damage in a single strip of finite elements.

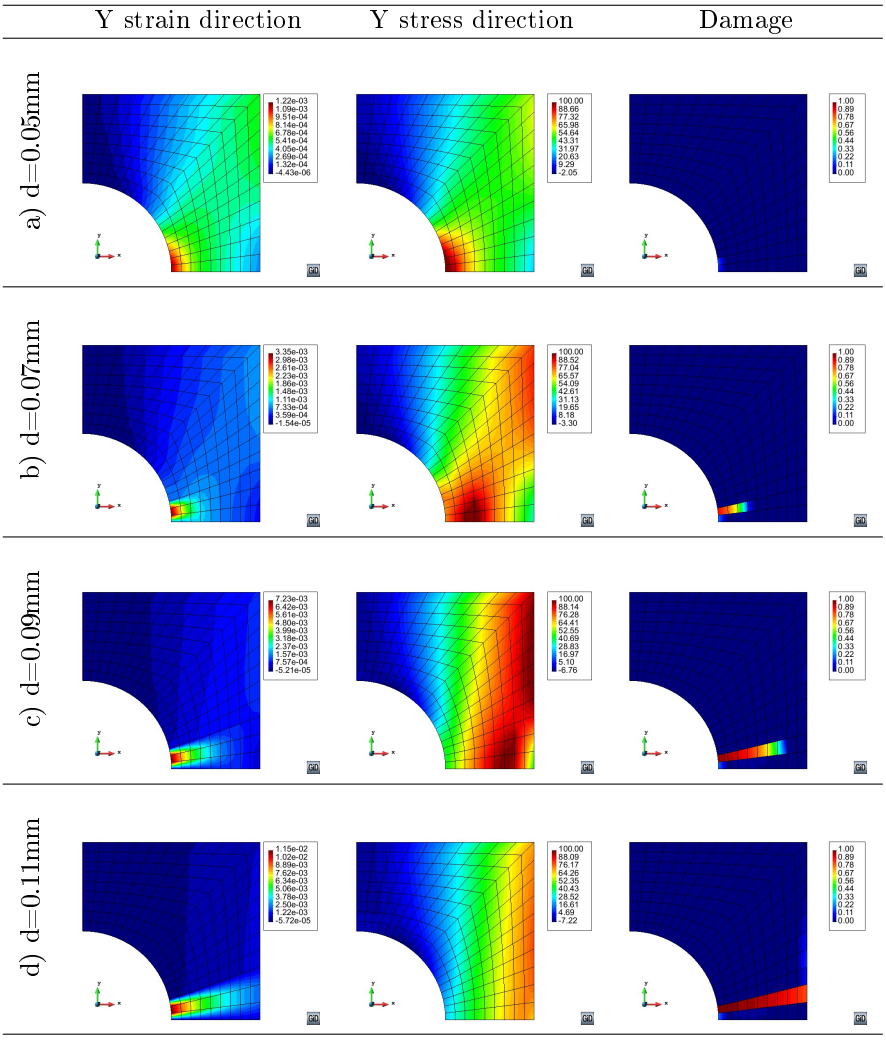

Figure 5.13: Results obtained in the plate with a hole to Mesh1.

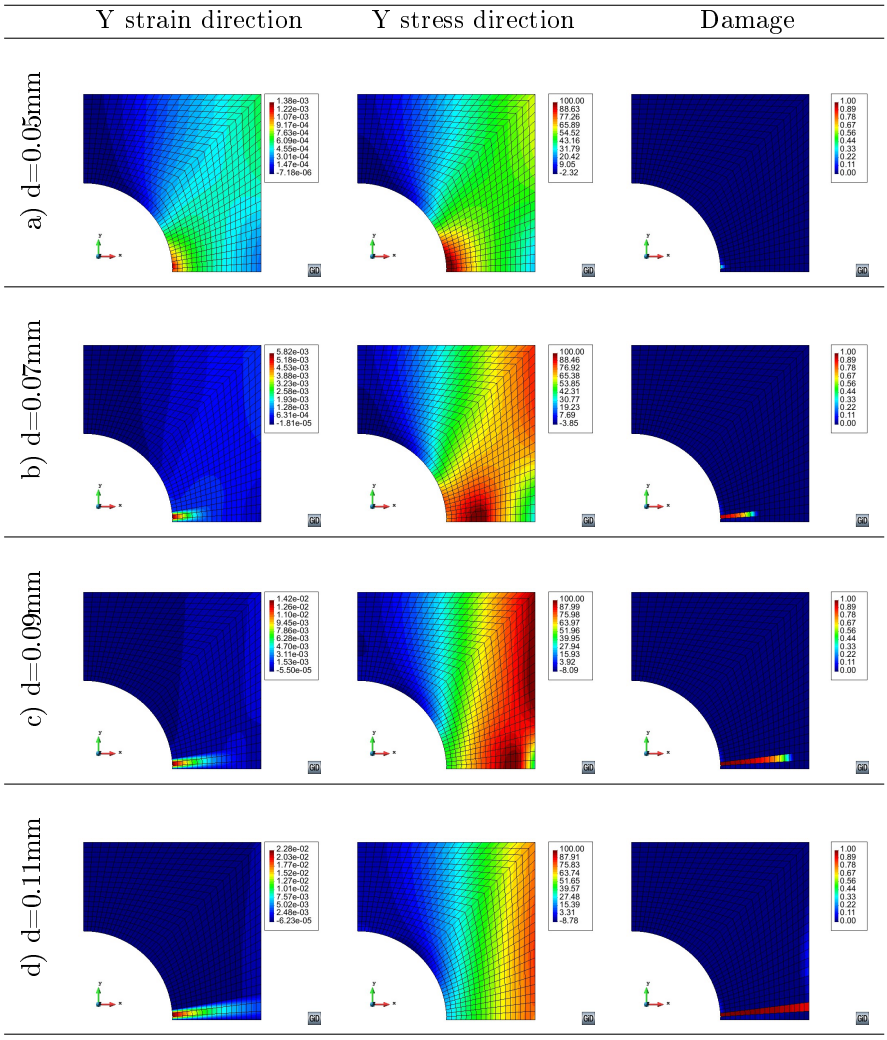

Figure 5.14: Results obtained in the plate with a hole to Mesh2.

Computational times

To show the advantage of using the NLS proposed, in comparison with a full classical FE^2, the calculation times are presented herein. A full FE^2 solves the microstructural problem for every integration point of the structure, and for every time step. This procedure does not distinguish between linear range and non-linear range.

Tables 5.5 and 5.6 present the calculation times required to solve the shown example in the same desktop computer, an Intel® Core™ i7-2600 CPU @ 3.40GHz with 8GB of RAM. The tables show the times used by the FE^2 and by the FE^2 with the NLS incorporated. The speed ratio column has the relation times between both methodologies.

Table 5.5 has the total real times necessary to complete the numerical test, up to d = 0.115mm, for all mesh configurations. The speed ratio variable shows that the advantage of using the developed strategies increases specially when the size of the macrostructure's mesh increases. This is an expected result because, in larger meshes, the proportion between linear and non-linear elements becomes also larger.

Model	FE^2	FE^2+NLS	Speed ratio
Mesh1-Micro1	1:21:53	0:28:19	2.89
Mesh1-Micro2	8:41:19	3:10:44	2.73
Mesh2-Micro1	11:19:49	2:29:28	4.55
Mesh2-Micro2	76:40:33	18:39:33	4.11

Table 5.5: Computation times requested to solve the plate with a hole [hs:min:seg].

On the other hand, it is important to mention that when a RVE becomes non-linear, its computational cost is more expensive than when it is linear. This is because, besides the possible iteration required by the RVE to obtain the correct non-linear solution, the estimation of the tangent constitutive tensor by perturbation method requires to solve the RVE six more times (see Subsection 5.2.3).

Consequently, when the number of non-linear elements in a problem increase, the efficiency of the proposed method decreases. For the analyzed example, if the simulation is stopped at the maximum admissible force in the structure (around d=0.08mm in Figure 5.12) which probably the most interesting value for an engineer, the speed ratio would be better. To prove this, let's consider the Mesh2-Micro2 simulation. In this case, when the maximum load is applied (d=0.08mm) there are only 392 elements in non-linear range, instead of 576 elements for d=0.115mm, and therefore at this load step the speed ratio is of 7 instead of 4.11.

This simulation is also used to validate the effect of the Smart First Step procedure. To do so, Table 5.6 shows the computational times consumed for the first step in each one of the simulations conducted. The times shown prove that using SFS strategy improves highly the computational efficiency also for small mesh sizes, as speed ratio variable shows. The table also shows that the number of RVE solved by the SFS is independent of the mesh used in the microstructural problem.

Model	without SFS		with SFS		Speed
	Time	RVE solved	Time	RVE solved	ratio
Mesh1-Micro1	0:17.9	2880	0:01.0	151	17.9
Mesh1-Micro2	1:48.3	2880	0:06.5	151	16.7
Mesh2-Micro1	2:12.0	23040	0:02.6	303	50.8
Mesh2-Micro2	14:05.9	23040	0:12.5	303	67.7

Table 5.6: First step computation times in the plate with a hole [min:seg].

5.4.2 Industrial Component

In order to validate the efficiency obtained with the NLS when it is applied to the solution of a real structure, in the following is included the non-linear simulation of an structural component. In this case, the structure selected for analysis is the industrial component show in Figure 5.15. The geometry of this engine stiffener has been proposed in the framework of M-RECT Project. The stiffener is linked on one side to the gearbox, and on the other side to the engine. This component has the objective of improving

the connection between engine and gearbox, as well as changing the dynamic properties of the overall structure.

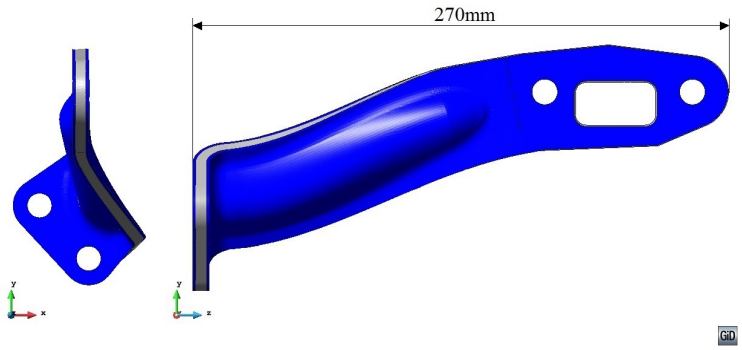

Figure 5.15: Engine stiffener part.

Materials

The material that will be used for the stiffener, different from the one used in M-RECT, is a laminated thermoplastic composite. Therefore, the material properties vary through the laminate thickness and respect to the laminate's reference direction. The composite is made with three orthotropic sheets (see Figure 5.15). The two external sheets (drawn in blue) have a thickness of 1.5mm each one and, the core sheet (drawn in gray) has a thickness of 5.5mm.

The external laminae is composed by carbon fibers in an epoxy matrix. The periodic microstructure of the external sheets can be represented by the RVE shown in the Figure 5.16. The laminate has a 40% of cylindrical long fiber volume.

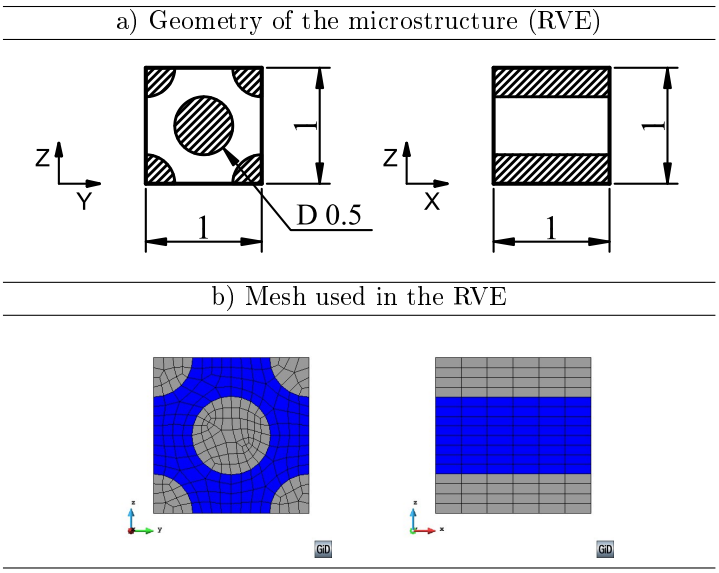

Figure 5.16: Geometry and mesh of the RVE used in the external sheets.

The matrix is an isotropic material, simulated with an explicit scalar damage constitutive model with exponential softening (resin epoxy HSC Epikote 4652). The long fiber is modeled with an elastic constitutive model (Grafil TR30S 3K carbon fiber). The properties of these simple materials are shown in Table 5.7 [101].

Finally, the FE mesh employed to analyze the RVE is shown in Figure 5.16. The mesh uses 1464 first order hexahedra finite elements.

On the other hand, the core sheet of the engine stiffener is a TenCate commercial product, Cetex TC1200 PEEK 5HS LAMINATE. The properties of this material have been obtained from TenCate

Material	E [GPa]	ν [−]	σ_{Limit} [MPa]	G_f [J/m^2]
Epoxy matrix	4.52	0.36	68	780
Carbon fiber	235	0.21	4410	-

Table 5.7: Simple material properties from Perez et al. (2013).

website [119] and are shown in Table 5.8. For the simulation, the core material is modeled using an elastic constitutive model.

Propertie [GPa]	$E(0^o)$	$E(90^o)$	G(In plane)
TenCate lamina	56.1	55.6	4.5

Table 5.8: TenCate Lamina properties.

Mesh and boundary conditions

Figure 5.17 label a) shows the mesh used to simulate the engine stiffener. The mesh has 355.302 first order tetrahedra finite elements. The external laminae requires 108.041 elements while the core lamina has 247.261 elements.

a) Mesh used in the engine stiffener

b) Nodes restricted and laminate's reference direction

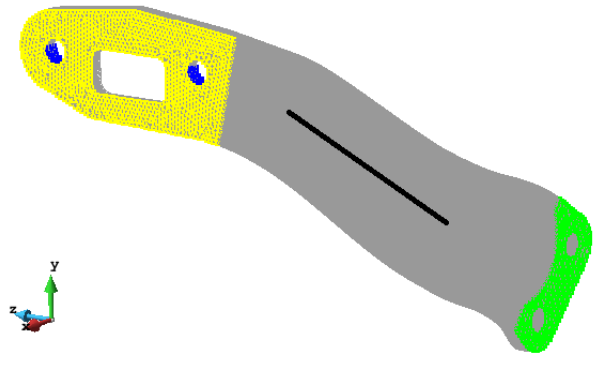

Figure 5.17: Mesh and boundary conditions used in the engine stiffener.

The nodes that will be restricted and the laminate's reference direction are shown in Figure 5.17 label b). The nodes with green color are over the face in contact with the gearbox. These nodes have a zero movement restriction in all directions. On the other hand, the nodes drawn in yellow are on the face in contact with the engine. In this case, the restriction on these nodes is a fixed displacement in X direction. The laminate's reference direction is the long fiber longitudinal direction in the external laminae.

Results

The analysis conducted on the first step to evaluate the elastic energy density available in each integration point allows defining a "possible damage" map of the structure, as it is shown in Figure 5.18 label a), where $\bar{f}$ is presented. The blue zones in the external sheets have a $\bar{f}$ near to zero and then, these zones will have a $\bar{\Psi}^{e}_{Limit}$ high while the zone with a $\bar{f}$ near to 1 (critical zones) will have a smaller elastic energy density available. Therefore, these zones are the regions where non-linear process has more possibilities to start. In this example, the SFS has required analyzing 6.514 RVEs to determine the threshold functions of the whole structure. This quantity represents only the 6% of the elements on the external laminae.

The numerical simulation has been stopped to a fixed X displacement of 1.36mm. The homogenized stress at the end of the analysis in the laminate's reference direction is shown in Figure 5.18 label b). From the figure it is observed that the maximum absolute stress is a compressive stress and it is located near to the face in contact with the gearbox. The maximum tensile stress is located in the same region but in the opposite external sheet.

a) Parameter $\bar{f}$ at the first step

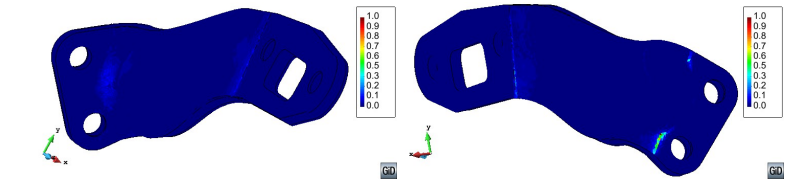

b) Homogenized stress on the reference direction

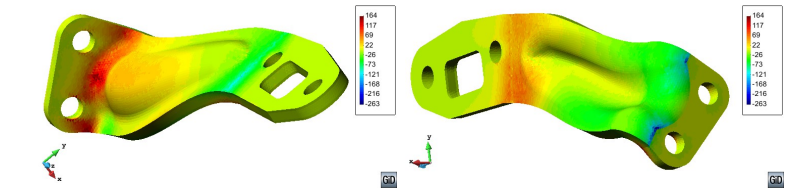

c) Scalar homogenized damage at external sheet

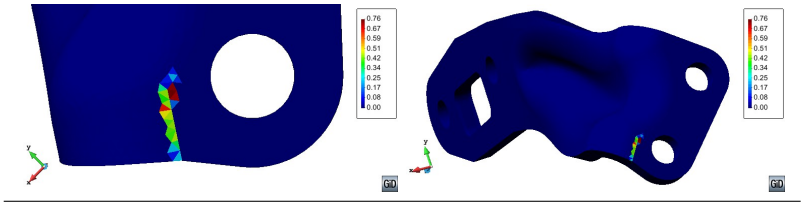

Figure 5.18: Results obtained in the engine stiffener.

Figure 5.18 label c) shows the scalar homogenized damage at the end of the test. The damaged area shown in figure has a relation with the previous results presented. It is on the maximum compressive stress zone (see label b)) and it is a critical zone in Figure 5.18 label a).

To understand the internal structure behavior in the damaged zone it is necessary to observe the mechanical performance of the most damaged RVE. In current simulation the RVE selected is the one with the maximum homogenized damage, in the engine stiffener mesh (see Figure 5.18 label c)). Figure 5.19 shows the results obtained for this RVE. This shows the stress in the RVE's local X axis at the beginning (label a) at first step) and at the end (label b) at last step) of the test. The shear stress in XY and YZ direction is also shown in the figure for the first step of the analysis. Finally, the matrix scalar damage variable in the RVE is shown for the last step.

From Figure 5.19 can be observed that X compression stress is the dominant state in the RVE but, its failure is produced by shear in the matrix material. On the other hand, the carbon fiber has an extremely high strength threshold (see Table 5.7), and because of this, this has been modeling with an elastic constitutive model. Figure shows that the maximum fiber stress reached in the analysis (label b) at last step) is far away of its strength threshold as it was expected.

Methods	FE^2	FE^2+NLS	Speed ratio
Time [hs:min]	782:46	11:36	67.4

Table 5.9: Computation times requested by the simulation.

The Figure 5.19 shows that the external sheet has interlaminar delamination in the damaged zone (see Figure 5.18 label c)). It is important to stand out that although the damage in the matrix is located in a small zone its global effect is meaningful. Figure 5.18 label c) shows that some elements have lost about 75% of its original load capacity.

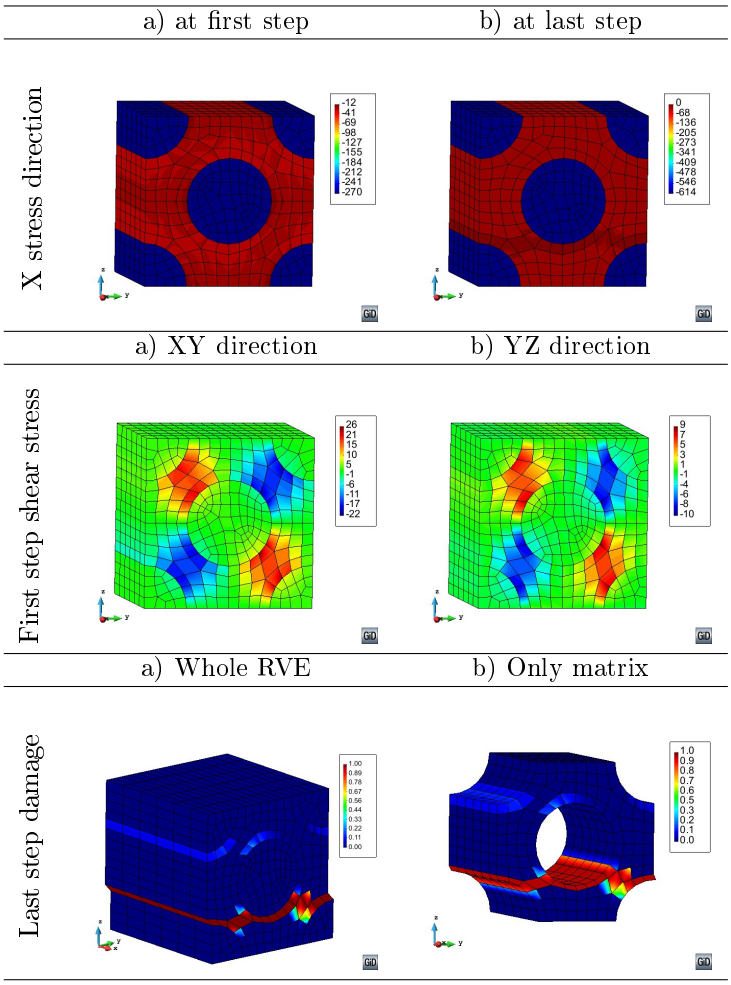

Figure 5.19: Results obtained in the RVE with maximum homogenized damage.

This example has shown that it is possible to solve real problems with a non-linear homogenization scheme. However, to see the advantages of the proposed NLS procedure, it is necessary to analyze the computational times required by the simulation, these are shown in Table 5.9. The FE^2 computational time has been evaluated based on the time required to solve one RVE and the number of steps and iterations required by the simulation. Table 5.9 shows that a FE^2 has a computational cost that makes unfeasible these sort of simulations. In current case, the simulation requires more than 32 days and 14 hours to be completed. The proposed method has a really good computational time (less than 12 hours) and it is capable of speeding up the process at a speed ratio of 67.4.

Chapter 6

Conclusions

The two-scale homogenization framework proposed in Part II of the dissertation which is described in detail in Chapter 3, has been proved a competitive alternative to model three-dimensional composite structures. The elimination of redundant unknowns implemented to solve the microscopic BVP through a cubic RVE has proven to be an efficient option to satisfy the boundary conditions. In addition, from the convergence analysis showing in Section 4.3.1, it has been shown that the method implemented has a good convergence behavior. For linear analysis, the comparison presented in the Chapter 4 proves that the multiscale homogenization has many advantages over other theories, such as micro-models or the SP theory, as it is capable of capturing complex responses of the material (such as dislocations) with an affordable computational cost.

The multiscale method can represent accurately effects such as a local damaged lamina because the internal structure of the composite is physically modeled in the RVE. The SP theory cannot account automatically for such effects, unless they are present in the whole finite element, as has been shown in the examples presented in Sections 4.3.2 and 4.3.4. However, the main advantage of the SP theory is that it is capable of conducting non-linear analysis without increasing substantially the computational cost of the simulation.

The comparison of the computational cost presented in Section 4.4 by the different formulations has shown that, in terms of computational time, the cost of the H-OneRVE and the SP Theory is comparable, and it is substantially lower than the one required by a Micro Model or the H-AllRVE. The main difference between the H-AllRVE model and the micro-model is found in the memory required by the simulation, being the cost of this last one 360 times larger.

A proposed extension to non-linear range of the two-scale homogenization methodology is proposed and presented in Chapter 5. The developed method uses a non-linear activation function defined in the structural scale which it is obtained by solving the micro-structural scale. The activation function predicts if a material point (or integration point) in the structure is in linear or non-linear range. Therefore, the method only analyzes the non-linear integration points by solving the microscopic BVP using the RVE. Section 5.2 shows the formulation developed to obtain the non-linear strategy proposed in this study. Besides, a smart first step had to be also developed to obtain in an efficient way the activation function.

The purpose of the non-linear procedure developed is to solve non-linear problems, and the first requirement to meet is conserve the dissipated energy through the scales. Section 5.3 describes in detail how the fracture length concept applied to one scale continuum mechanics is extended to multiscale homogenization approach. It is shown that the method presented is energy consistent and macro-micro mesh independent.

The main objective of the proposed non-linear strategy is to reduce significantly the computational times requested by a multi-scale approach. The plate with a hole example presented in Section 5.4.1 shows how the computational times are reduced around four times. Besides, the mesh independency and energy consistency of the proposed methodology is proved again. The example also shows how the localization phenomena in the structural scale, in this case the plate with a hole, appears naturally from the micro-structural scale. Finally, an engine stiffener has been solved in Section 5.4.2 to prove the large computational advantage of the proposed procedure when a real industrial component is simulated. The computational time is less than 12 hours comparing to 32 days and almost 15 hours required by a classical FE^2 approach. In addition, the method predicted the failure zone naturally and the mode failure of the internal structure.

Conclusions

In this final chapter the main points of the dissertation are presented in terms of an achievements attained and in terms of concluding remarks. Future improvements and future lines of developments based on the experience and on the main difficulties found while developing this research are suggested at the end.

Achievements

The main aim of the present dissertation is to develop a comprehensive constitutive formulation for the analysis of three-dimensional composite structures in linear and non-linear range. In this context, a phenomenological homogenization method for composites using carbon nanotubes as reinforcement was developed in the first stage of this study. Then, with the objective to extend the reinforcement used a multiscale homogenization procedure was proposed. An efficient and consistent methodology was developed to address non-linear analysis for realistic composite structures. Besides, an enhanced-first-order homogenization was proposed to consider higher-order effect in the internal structure of the composite.

In Part I, the composite constitutive model proposed, based on the mixing theory, for reinforced composites with carbon nanotubes has been presented. The developed formulation relates the reinforcement and the matrix through an interface material. Therefore, it is possible to consider non-linear phenomenons by using non-linear constitutive laws to characterize the interface material.

It has been shown that the elastic properties estimated with the proposed formulation are in good agreement with experimental values obtained from the literature data. The validation of the non-linear response provided by the presented composite model has been performed using the experimental data of two different composites made with MWCNTs randomly distributed.

Then, the developed formulation has been used to predict and compare the mechanical properties of a straight beam subjected to four-point bending, with different material configurations. In addition, a non-linear analysis has also been made using the same structure and composites showing the capacity of the proposed methodology.

In Part II, the proposed two-scale homogenization method and its extension to non-linear range have been presented. The developed formulation has shown to be a competitive alternative to model three-dimensional composite structures. For linear analysis, the presented methodology has proved to have many advantages over other theories, as it is capable of capturing complex responses of the material with an affordable computational cost. However, for non-linear analysis of structures the computational time of the multiscale approach is strongly expensive, but not the memory required by the simulation.

Therefore, a novel extension for multiscale homogenization to non-linear range is developed. The proposed formulation uses a non-linear activation function in the structural scale and its task is predict if a material point on the structure is in linear or non-linear range. Because of this, the developed strategy only solves the microscopic BVP using the RVE for the non-linear integration points found. The fracture length concept has been extended to multiscale homogenization approach so it has allowed that the developed approach is energy consistent and presents a macro-micro mesh independent. In addition, a smart first step had to be also developed to obtain in an efficient way the activation function.

The example of the plate with a hole shows how the localization phenomenon on the structural scale appears naturally from the micro-structural scale. The presented examples also show the significantly reduction of the computational times of the developed non-linear strategy. For the engine stiffener example, the computational time is less than 12 hours comparing to 32 days and almost 15 hours required by a classical FE^2 approach. In addition, in the examples the method predicted the failure zone naturally and the mode failure of the internal structure.

Concluding remarks

The phenomenological constitutive model developed for reinforced composite using CNTs is based on the classical mixing theory. The presented formulation is an "Ad-hoc" homogenization procedure which can be considered as a constitutive equation manager as the theory of mixtures it is. Therefore, the developed methodology could be easily extended to other composites which using reinforcements with similar behavior such as nanofiber or short fiber.

Besides that the non-linear performance of the composite is provided by each constitutive model, the load transfer capacity of the interface region is also affected if the interface is damaged. The formulation has included this effect through affecting the parallel length with the damage level of the interface. Therefore, if the interface is fully damaged the contribution of the CNTs to the composite is null.

However, as every phenomenological method, the developed constitutive model requires some parameters to be calibrated such as the geometric parameters and mechanical properties of the interface component. These altogether with the intrinsic problems of the mixing theory are the main drawbacks of the proposed procedure.

The decision of following a first-order homogenization approach and then improve it to obtain a enhanced-first-order formulation over using a full second-order computational approximation was based on the fact that the computational implementation of the high-order formulation generally involve elements which uses larger number of nodes, degrees of freedom and boundary conditions.

The solution of the microstructural problem has been addressed using a *Periodic boundary fluctuations* condition. The other boundary conditions have been shown that overestimate and underestimate the characterization of the microstructure. However, the periodic boundary condition has been proved that good estimate the effective microstructural stiffness. This condition also allows an strain localization band in the RVE without introducing spurious effects for non-linear case.

The effect of the two-scale softening problem and the strain localization bands for both scales were addressed through the fracture length concept. The conventional method used in FEM to approximate the fracture length by some reference length of the finite element is extended to FE^2 homogenization. Therefore, the specific energy at the micro-scale level is related to the fracture energy through both reference lengths now. The developed procedure has shown to be a good and simple computationally way to conserve the energy through the scales and ensures the objectivity of the FE^2 response.

Future work

The future work and future and future possible lines of study are given in this section as a list of brief paragraphs which describe each one of them.

In general, the carbon nanotubes tend to agglomerate, also they have the undulation and misalignment problems during the manufacture of the composite. The effect of these issues on the final properties and response of the composite some time is meaningful. Therefore, the introduction of some corrector parameters to control these phenomenons would be a significant improved for the phenomenological homogenization proposed.

General extension of the phenomenological homogenization develop in Part I to consider any kind of short reinforcement and thereby extend its application to short fiber reinforced composites and to the new generation of concrete materials reinforced with steel short fiber.

Implementation of other constitutive laws for the simulation of simple materials such as plasticity in the micro-scale. Therefore, other failure phenomena may be studied in the macro-scale.

Investigate the extension of the develop multiscale approach to consider finite strain.

Perform examples using the non-linear strategy together to the enhanced-first-order homogenization proposed.

In many composites can be observed two or more reinforcement level. For example, a composite of long fiber reinforced matrix where the matrix also is reinforced with nanotubes, it is possible to think in a multiscale/multi-method approach to analyze this kind of materials. Therefore, the CNTs reinforced the plain matrix could be simulated in a sub-scale with the phenomenological homogenization proposed

and then simulate this sub-composite as a homogenized material in the RVE of the meso-scale together with the long fiber using a multiscale homogenization.

Improve the efficiency of the parallelization process in order to get a fully optimized approach. In the current parallel implementation the calculation process on the macro problem is subdivided in an efficient dynamic way using the *OpenMP* philosophy. The calculation process on the micro problem is addressed in a serial process. A new parallel implementation using a *MPI* philosophy in the macro problem and then a *OpenMP* philosophy in the micro problem will reduce the computational times of the simulations.

Extension of the multiscale homogenization implemented to different theories for the simulation of the structure scale such as shell and plates formulations. The simulation of the composite behavior with its real dimensions through of a micro-scale using the three-dimensional formulation presented.

Appendix A

Constitutive models

The formulation developed is Section 4.2 require all composite components must fulfill the expression given by (4.1). Therefore, it is possible to use any constitutive law to describe the mechanical performance of the different components. However, for the sake of simplicity, in this appendix are defined the three specific models that will be used for each composite component.

A.1 Elasto-plastic constitutive model

Matrix material is defined with an elastoplastic law. The specific Helmholtz free energy for this material, considering uncoupled elasticity is

$$\Psi\left(\varepsilon^e, p, \theta\right) = \Psi^e\left(\varepsilon^e\right) + \Psi^p\left(p\right) + \Psi^t\left(\theta\right) = \frac{1}{2}\varepsilon^e : C : \varepsilon^e + \Psi^p\left(p\right) + \Psi^t\left(\theta\right), \tag{A.1}$$

where Ψ^e is the specific elastic free energy, Ψ^p is the specific plastic free energy, Ψ^t is the specific temperature free energy, p is a internal variable tensor associated with plastic behavior. The total deformation of the material tensor is split into its elastic, ε^e and plastic, ε^p parts. This is

$$\varepsilon = \varepsilon^e + \varepsilon^p \tag{A.2}$$

The local form of the Clausius-Duhem inequality for this material can be expressed as

$$\Xi = \sigma : \dot{\varepsilon} - \eta\dot{\theta} - \dot{\Psi} - \frac{1}{\theta} q . \frac{\partial \theta}{\partial x} \geq 0, \tag{A.3}$$

and using the above expression it can rewritten as

$$\sigma : (\dot{\varepsilon}^e + \dot{\varepsilon}^p) - \eta\dot{\theta} - \left[\frac{\partial \Psi^e}{\partial \varepsilon^e} : \dot{\varepsilon}^e + \frac{\partial \Psi^p}{\partial p} . \dot{p} + \frac{\partial \Psi^t}{\partial \theta}\dot{\theta}\right] - \frac{1}{\theta} q . \frac{\partial \theta}{\partial x} \geq 0 \tag{A.4}$$

or

$$\left(\sigma - \frac{\partial \Psi^e}{\partial \varepsilon^e}\right) : \dot{\varepsilon}^e - \left(\eta + \frac{\partial \Psi^t}{\partial \theta}\right)\dot{\theta} + \sigma : \dot{\varepsilon}^p - \frac{\partial \Psi^p}{\partial p} . \dot{p} - \frac{1}{\theta} q . \frac{\partial \theta}{\partial x} \geq 0. \tag{A.5}$$

being σ the stress tensor, η the entropy, and q the vector field of heat flow. To ensure compliance with the second thermodynamic law it must be defined

$$\sigma \doteq \frac{\partial \Psi^e}{\partial \varepsilon^e} \qquad \eta \doteq -\frac{\partial \Psi^t}{\partial \theta} \qquad P \doteq -\frac{\partial \Psi^p}{\partial p} \tag{A.6}$$

where P is the thermodynamic tensor associated with the internal variable tensor p. Finally, the mechanical dissipation for a material point is

$$\Xi_m = \Xi_p = \sigma : \dot{\varepsilon}^p + P . \dot{p} \geq 0. \tag{A.7}$$

A.2 Elasto-damage constitutive model

The interface region is simulated with a damage material. In this case, the expression of the Helmholtz free energy is

$$\begin{aligned}\Psi(\varepsilon, d, \theta) = \Psi^e(\varepsilon, d) + \Psi^t(\theta) &= (1-d)\,\Psi_o^e(\varepsilon) + \Psi^t(\theta) \\ &= (1-d)\,\frac{1}{2}\varepsilon : C : \varepsilon + \Psi^t(\theta),\end{aligned} \tag{A.8}$$

where d is a internal variable associated with the damage. The local form of the Clausius-Duhem inequality Eq.A.3 for this material can be expressed as

$$\sigma : \dot{\varepsilon} - \eta\dot{\theta} - \left[\frac{\partial \Psi^e}{\partial \varepsilon} : \dot{\varepsilon} + \frac{\partial \Psi^e}{\partial d}\dot{d} + \frac{\partial \Psi^t}{\partial \theta}\dot{\theta}\right] - \frac{1}{\theta} q.\frac{\partial \theta}{\partial x} \geq 0 \tag{A.9}$$

or

$$\left(\sigma - \frac{\partial \Psi^e}{\partial \varepsilon}\right) : \dot{\varepsilon} - \left(\eta + \frac{\partial \Psi^t}{\partial \theta}\right)\dot{\theta} - \frac{\partial \Psi^e}{\partial d}\dot{d} - \frac{1}{\theta} q.\frac{\partial \theta}{\partial x} \geq 0. \tag{A.10}$$

To ensure compliance with the second thermodynamic law it must be defined

$$\sigma \doteq \frac{\partial \Psi^e}{\partial \varepsilon} \qquad \eta \doteq -\frac{\partial \Psi^t}{\partial \theta} \qquad D \doteq -\frac{\partial \Psi^e}{\partial d}, \tag{A.11}$$

being D the thermodynamic scalar associated with the internal scalar variable d. And, the mechanical dissipation for a material point is

$$\Xi_m = \Xi_d = D.\dot{d} \geq 0. \tag{A.12}$$

A.3 Elastic constitutive model

Nanotubes are considered elastic. In this case the Helmholtz free energy can be written as

$$\Psi(\varepsilon, \theta) = \Psi^e(\varepsilon) + \Psi^t(\theta) = \frac{1}{2}\varepsilon : C : \varepsilon + \Psi^t(\theta). \tag{A.13}$$

And the local form of the Clausius-Duhem inequality Eq.A.3 can be expressed in this case as

$$\sigma : \dot{\varepsilon} - \eta\dot{\theta} - \left[\frac{\partial \Psi^e}{\partial \varepsilon} : \dot{\varepsilon} + \frac{\partial \Psi^t}{\partial \theta}\dot{\theta}\right] - \frac{1}{\theta} q.\frac{\partial \theta}{\partial x} \geq 0 \tag{A.14}$$

or

$$\left(\sigma - \frac{\partial \Psi^e}{\partial \varepsilon}\right) : \dot{\varepsilon} - \left(\eta + \frac{\partial \Psi^t}{\partial \theta}\right)\dot{\theta} - \frac{1}{\theta} q.\frac{\partial \theta}{\partial x} \geq 0. \tag{A.15}$$

Therefore, to ensure compliance with the second thermodynamic law

$$\sigma \doteq \frac{\partial \Psi^e}{\partial \varepsilon} \qquad \eta \doteq -\frac{\partial \Psi^t}{\partial \theta}. \tag{A.16}$$

Appendix B

Computational implementation

B.1 Microscopic Kinematic relationships

Taking a structured finite element mesh on the boundary of the RVE showing in Figure B.1, it is possible identify easily master and slave nodes. The right part of figure shows the chosen master nodes (named with a letter) and the slave nodes (named with a letter and number). The quantity of periodic nodes depends on the FE Mesh. Table B.1 shows master nodes and the slave nodes located on the edges and surfaces of the RVE shown in Figure B.1. Moreover, Table B.2 shows the eight periodic vertices nodes in the RVE (see left part of Figure B.1). In these vertices nodes, also it is possible to identify a master node and seven slave nodes. In the following, the vertice node "a" will be the master vertice node and the others seven vertices nodes ("b" ,"c" , ... and "h") are the slaves nodes.

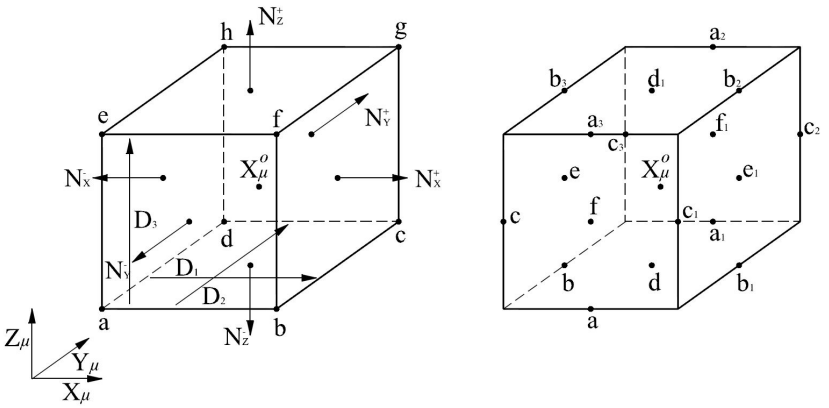

Figure B.1: Master and slaves nodes in a general hexagonal RVE.

Master nodes	a	b	c	d	e	f
Slave nodes	a_1, a_2, a_3	b_1, b_2, b_3	c_1, c_2, c_3	d_1	e_1	f_1

Table B.1: Master and slave periodic nodes denomination.

Nodes	a	b	c	d	e	f	g	h

Table B.2: Periodic vertices nodes in the RVE.

Considering a generic master node "a" on the axis X and its slave nodes "a_1", "a_2" and "a_3" the position

vector difference between their in the reference configuration is

$$\mathbf{X}_{a_1}-\mathbf{X}_a=\left\{\begin{array}{c}X_\mu\\ D_2/2\\ -D_3/2\end{array}\right\}-\left\{\begin{array}{c}X_\mu\\ -D_2/2\\ -D_3/2\end{array}\right\}=\left\{\begin{array}{c}0\\ D_2\\ 0\end{array}\right\}=D_2\mathbf{N}_Y^+$$

$$\mathbf{X}_{a_2}-\mathbf{X}_a=\left\{\begin{array}{c}X_\mu\\ D_2/2\\ D_3/2\end{array}\right\}-\left\{\begin{array}{c}X_\mu\\ -D_2/2\\ -D_3/2\end{array}\right\}=\left\{\begin{array}{c}0\\ D_2\\ D_3\end{array}\right\}=D_2\mathbf{N}_Y^+ + D_3\mathbf{N}_Z^+ \tag{B.1}$$

$$\mathbf{X}_{a_3}-\mathbf{X}_a=\left\{\begin{array}{c}X_\mu\\ -D_2/2\\ D_3/2\end{array}\right\}-\left\{\begin{array}{c}X_\mu\\ -D_2/2\\ -D_3/2\end{array}\right\}=\left\{\begin{array}{c}0\\ 0\\ D_3\end{array}\right\}=D_3\mathbf{N}_Z^+$$

Following the same procedure is possible to obtain the position vector difference for the other master and slave nodes as

$$\mathbf{X}_{b_1}-\mathbf{X}_b=D_1\mathbf{N}_X^+,\quad \mathbf{X}_{b_2}-\mathbf{X}_b=D_1\mathbf{N}_X^+ + D_3\mathbf{N}_Z^+,\quad \mathbf{X}_{b_3}-\mathbf{X}_b=D_3\mathbf{N}_Z^+, \tag{B.2}$$

$$\mathbf{X}_{c_1}-\mathbf{X}_c=D_1\mathbf{N}_X^+,\quad \mathbf{X}_{c_2}-\mathbf{X}_c=D_1\mathbf{N}_X^+ + D_2\mathbf{N}_Y^+,\quad \mathbf{X}_{c_3}-\mathbf{X}_c=D_2\mathbf{N}_Y^+, \tag{B.3}$$

$$\mathbf{X}_{d_1}-\mathbf{X}_d=D_3\mathbf{N}_Z^+,\quad \mathbf{X}_{e_1}-\mathbf{X}_e=D_1\mathbf{N}_X^+,\quad \mathbf{X}_{f_1}-\mathbf{X}_f=D_2\mathbf{N}_Y^+. \tag{B.4}$$

And, for the vertices nodes are

$$\mathbf{X}_b-\mathbf{X}_a=D_1\mathbf{N}_X^+,\quad \mathbf{X}_c-\mathbf{X}_a=D_1\mathbf{N}_X^+ + D_2\mathbf{N}_Y^+,\quad \mathbf{X}_d-\mathbf{X}_a=D_2\mathbf{N}_Y^+, \tag{B.5}$$

$$\mathbf{X}_e-\mathbf{X}_a=D_3\mathbf{N}_Z^+,\quad \mathbf{X}_f-\mathbf{X}_a=D_1\mathbf{N}_X^+ + D_3\mathbf{N}_Z^+, \tag{B.6}$$

$$\mathbf{X}_g-\mathbf{X}_a=D_1\mathbf{N}_X^+ + D_2\mathbf{N}_Y^+ + D_3\mathbf{N}_Z^+,\quad \mathbf{X}_h-\mathbf{X}_a=D_2\mathbf{N}_Y^+ + D_3\mathbf{N}_Z^+. \tag{B.7}$$

where D_1, D_2 and D_3 are the X, Y and Z direction size of the RVE.

B.1.1 Master-slave kinematic relationships

In the following sections the kinematic master-slave relationships will be obtained in the first-order and enhanced-first-order homogenization approaches.

First-order approach

Taking into account that *Periodic boundary fluctuations* condition are considered in the microscopic BVP and the proposed displacement field given by (3.9) is possible to write the displacement of the slave node "a_1" as a function of the displacement of the master node "a" as

$$\mathbf{u}_{a_1}=\mathbf{u}_a+(\mathbf{F}-\mathbf{I})\cdot(\mathbf{X}_{a_1}-\mathbf{X}_a), \tag{B.8}$$

and using the above expression

$$\mathbf{u}_{a_1}=\mathbf{u}_a+D_2(\mathbf{F}-\mathbf{I})\cdot\mathbf{N}_Y^+. \tag{B.9}$$

To simplify the final expressions is defined: $\mathbf{sm}_1=D_1(\mathbf{F}-\mathbf{I})\cdot\mathbf{N}_X^+$, $\mathbf{sm}_2=D_2(\mathbf{F}-\mathbf{I})\cdot\mathbf{N}_Y^+$ and $\mathbf{sm}_3=D_3(\mathbf{F}-\mathbf{I})\cdot\mathbf{N}_Z^+$. Therefore, it can be shown that

$$\begin{array}{lll}\mathbf{u}_{a_1}=\mathbf{u}_a+\mathbf{sm}_2, & \mathbf{u}_{a_2}=\mathbf{u}_a+\mathbf{sm}_2+\mathbf{sm}_3, & \mathbf{u}_{a_3}=\mathbf{u}_a+\mathbf{sm}_3,\\ \mathbf{u}_{b_1}=\mathbf{u}_b+\mathbf{sm}_1, & \mathbf{u}_{b_2}=\mathbf{u}_b+\mathbf{sm}_1+\mathbf{sm}_3, & \mathbf{u}_{b_3}=\mathbf{u}_b+\mathbf{sm}_3,\\ \mathbf{u}_{c_1}=\mathbf{u}_c+\mathbf{sm}_1, & \mathbf{u}_{c_2}=\mathbf{u}_c+\mathbf{sm}_1+\mathbf{sm}_2, & \mathbf{u}_{c_3}=\mathbf{u}_c+\mathbf{sm}_2,\\ \mathbf{u}_{d_1}=\mathbf{u}_d+\mathbf{sm}_3, & \mathbf{u}_{e_1}=\mathbf{u}_e+\mathbf{sm}_1, & \mathbf{u}_{f_1}=\mathbf{u}_f+\mathbf{sm}_2.\end{array} \tag{B.10}$$

And, for the vertices nodes

$$\begin{array}{lll}\mathbf{u}_b=\mathbf{u}_a+\mathbf{sm}_1, & \mathbf{u}_c=\mathbf{u}_a+\mathbf{sm}_1+\mathbf{sm}_2, & \mathbf{u}_d=\mathbf{u}_a+\mathbf{sm}_2,\\ \mathbf{u}_e=\mathbf{u}_a+\mathbf{sm}_3, & \mathbf{u}_f=\mathbf{u}_a+\mathbf{sm}_1+\mathbf{sm}_3, & \\ \mathbf{u}_g=\mathbf{u}_a+\mathbf{sm}_1+\mathbf{sm}_2+\mathbf{sm}_3, & \mathbf{u}_h=\mathbf{u}_a+\mathbf{sm}_2+\mathbf{sm}_3 & \end{array} \tag{B.11}$$

Enhanced first-order approach

Considering again that *Periodic boundary fluctuations* condition are considered in the microscopic BVP and the proposed displacement field given by (3.36) is possible to rewrite the displacement of the slave node "a_1" as a function of the displacement of the master node "a" for the enriched approach as

$$\mathbf{u}_{a_1} = \mathbf{u}_a + (\mathbf{F}-\mathbf{I})\cdot(\mathbf{X}_{a_1}-\mathbf{X}_a) + \frac{1}{2}\left(\mathbf{X}_{a_1}\cdot\mathbf{G}\cdot\mathbf{X}_{a_1} - \mathbf{X}_a\cdot\mathbf{G}\cdot\mathbf{X}_a\right) \tag{B.12}$$

and using (B.1) can be rewritten as

$$\mathbf{u}_{a_1} = \mathbf{u}_a + D_2(\mathbf{F}-\mathbf{I})\cdot\mathbf{N}_Y^+ + \frac{(D_2)^2}{2}\mathbf{N}_Y^+\cdot\mathbf{G}\cdot\mathbf{N}_Y^+ + D_2\mathbf{X}_a\cdot\mathbf{G}\cdot\mathbf{N}_Y^+. \tag{B.13}$$

To simplify the final expressions is defined

$$\begin{gathered}
\mathbf{sm}_1^G = \tfrac{(D_1)^2}{2}\mathbf{N}_X^+\cdot\mathbf{G}\cdot\mathbf{N}_X^+, \quad \mathbf{sm}_2^G = \tfrac{(D_2)^2}{2}\mathbf{N}_Y^+\cdot\mathbf{G}\cdot\mathbf{N}_Y^+, \quad \mathbf{sm}_3^G = \tfrac{(D_3)^2}{2}\mathbf{N}_Z^+\cdot\mathbf{G}\cdot\mathbf{N}_Z^+,\\
\mathbf{sm}_{12}^G = D_1D_2\mathbf{N}_X^+\cdot\mathbf{G}\cdot\mathbf{N}_Y^+, \quad \mathbf{sm}_{13}^G = D_1D_3\mathbf{N}_X^+\cdot\mathbf{G}\cdot\mathbf{N}_Z^+, \quad \mathbf{sm}_{23}^G = D_2D_3\mathbf{N}_Y^+\cdot\mathbf{G}\cdot\mathbf{N}_Z^+,\\
\mathbf{SM}_1^G = D_1\mathbf{N}_X^+\cdot\mathbf{G}, \quad \mathbf{SM}_2^G = D_2\mathbf{N}_Y^+\cdot\mathbf{G}, \quad \mathbf{SM}_3^G = D_3\mathbf{N}_Z^+\cdot\mathbf{G}.
\end{gathered}$$

Therefore, it can be shown that the slaves nodes are

$$\begin{aligned}
\mathbf{u}_{a_1} &= \mathbf{u}_a + \mathbf{sm}_2 + \mathbf{sm}_2^G + \mathbf{SM}_2^G\cdot\mathbf{X}_a,\\
\mathbf{u}_{a_2} &= \mathbf{u}_a + \mathbf{sm}_2 + \mathbf{sm}_3 + \mathbf{sm}_2^G + \mathbf{sm}_3^G + \mathbf{sm}_{23}^G + (\mathbf{SM}_2^G + \mathbf{SM}_3^G)\cdot\mathbf{X}_a,\\
\mathbf{u}_{a_3} &= \mathbf{u}_a + \mathbf{sm}_3 + \mathbf{sm}_3^G + \mathbf{SM}_3^G\cdot\mathbf{X}_a\\
\\
\mathbf{u}_{b_1} &= \mathbf{u}_b + \mathbf{sm}_1 + \mathbf{sm}_1^G + \mathbf{SM}_1^G\cdot\mathbf{X}_b,\\
\mathbf{u}_{b_2} &= \mathbf{u}_b + \mathbf{sm}_1 + \mathbf{sm}_3 + \mathbf{sm}_1^G + \mathbf{sm}_3^G + \mathbf{sm}_{13}^G + (\mathbf{SM}_1^G + \mathbf{SM}_3^G)\cdot\mathbf{X}_b,\\
\mathbf{u}_{b_3} &= \mathbf{u}_b + \mathbf{sm}_3 + \mathbf{sm}_3^G + \mathbf{SM}_3^G\cdot\mathbf{X}_b,\\
\\
\mathbf{u}_{c_1} &= \mathbf{u}_c + \mathbf{sm}_1 + \mathbf{sm}_1^G + \mathbf{SM}_1^G\cdot\mathbf{X}_c,\\
\mathbf{u}_{c_2} &= \mathbf{u}_c + \mathbf{sm}_1 + \mathbf{sm}_2 + \mathbf{sm}_1^G + \mathbf{sm}_2^G + \mathbf{sm}_{12}^G + (\mathbf{SM}_1^G + \mathbf{SM}_2^G)\cdot\mathbf{X}_c,\\
\mathbf{u}_{c_3} &= \mathbf{u}_c + \mathbf{sm}_2 + \mathbf{sm}_2^G + \mathbf{SM}_2^G\cdot\mathbf{X}_c,\\
\mathbf{u}_{d_1} &= \mathbf{u}_d + \mathbf{sm}_3 + \mathbf{sm}_3^G + \mathbf{SM}_3^G\cdot\mathbf{X}_d,\\
\mathbf{u}_{e_1} &= \mathbf{u}_e + \mathbf{sm}_1 + \mathbf{sm}_1^G + \mathbf{SM}_1^G\cdot\mathbf{X}_e,\\
\mathbf{u}_{f_1} &= \mathbf{u}_f + \mathbf{sm}_2 + \mathbf{sm}_2^G + \mathbf{SM}_2^G\cdot\mathbf{X}_f.
\end{aligned} \tag{B.14}$$

And, taking into account that the position vector of the master vertice node "a" is: $\mathbf{X}_a = -\frac{D_1}{2}\mathbf{N}_X^+ - \frac{D_2}{2}\mathbf{N}_Y^+ - \frac{D_3}{2}\mathbf{N}_Z^+$, the slaves vertices nodes are

$$\begin{aligned}
\mathbf{u}_b &= \mathbf{u}_a + \mathbf{sm}_1 - \tfrac{\mathbf{sm}_{12}^G}{2} - \tfrac{\mathbf{sm}_{13}^G}{2},\\
\mathbf{u}_c &= \mathbf{u}_a + \mathbf{sm}_1 + \mathbf{sm}_2 - \tfrac{\mathbf{sm}_{13}^G}{2} - \tfrac{\mathbf{sm}_{23}^G}{2},\\
\mathbf{u}_d &= \mathbf{u}_a + \mathbf{sm}_2 - \tfrac{\mathbf{sm}_{12}^G}{2} - \tfrac{\mathbf{sm}_{23}^G}{2},\\
\mathbf{u}_e &= \mathbf{u}_a + \mathbf{sm}_3 - \tfrac{\mathbf{sm}_{13}^G}{2} - \tfrac{\mathbf{sm}_{23}^G}{2},\\
\mathbf{u}_f &= \mathbf{u}_a + \mathbf{sm}_1 + \mathbf{sm}_3 - \tfrac{\mathbf{sm}_{12}^G}{2} - \tfrac{\mathbf{sm}_{23}^G}{2},\\
\mathbf{u}_g &= \mathbf{u}_a + \mathbf{sm}_1 + \mathbf{sm}_2 + \mathbf{sm}_3,\\
\mathbf{u}_h &= \mathbf{u}_a + \mathbf{sm}_2 + \mathbf{sm}_3^G - \tfrac{\mathbf{sm}_{12}^G}{2} - \tfrac{\mathbf{sm}_{13}^G}{2}.
\end{aligned} \tag{B.15}$$

B.2 Elimination of the slave degrees of freedom

In the present appendix the reduction of the degrees of freedom on the equation system is shown for the different implemented cases.

B.2.1 Linear implementation

Introducing the concept of master nodes and slave nodes into the equation system, it can be rewritten as

$$\left\{ \left[\begin{array}{c|c|c} K_{ii} & K_{im} & K_{is} \\ \hline K_{mi} & K_{mm} & K_{ms} \\ \hline K_{si} & K_{sm} & K_{ss} \end{array}\right] \left\{\begin{array}{c} u_i \\ \hline u_m \\ \hline u_s \end{array}\right\} \right\} \cdot \left\{\begin{array}{c} w_i \\ \hline w_m \\ \hline w_s \end{array}\right\} = 0 \qquad \forall\, w, \tag{B.16}$$

where the subscripts i, m, and s refer to the degrees of freedom of the internal nodes, master nodes and slave nodes, respectively. If the contribution of each type of degree of freedom is separated

$$\begin{aligned} &\left\{ \left[\begin{array}{c} K_{ii} \\ \hline K_{mi} \\ \hline K_{si} \end{array}\right] \{u_i\} + \left[\begin{array}{c} K_{im} \\ \hline K_{mm} \\ \hline K_{sm} \end{array}\right] \{u_m\} \right. \\ &\left. + \left[\begin{array}{c} K_{is} \\ \hline K_{ms} \\ \hline K_{ss} \end{array}\right] \{u_s\} \right\} \cdot \left\{\begin{array}{c} w_i \\ \hline w_m \\ \hline w_s \end{array}\right\} = 0 \qquad \forall\, w. \end{aligned} \tag{B.17}$$

Considering that *Periodic boundary fluctuations* condition are taken in the microscopic problem, it is possible to write in matrix form the master-slave kinematic relationship presented in the Section B.1.1 of the Appendix B.1 as

$$\{u_s\} = [S_{sm}]\{u_m\} + \{\triangle_d\}\,. \tag{B.18}$$

Introducing (B.18) in (B.17) is obtained

$$\begin{aligned} &\left\{ \left[\begin{array}{c} K_{ii} \\ \hline K_{mi} \\ \hline K_{si} \end{array}\right] \{u_i\} + \left[\begin{array}{c} K_{im} \\ \hline K_{mm} \\ \hline K_{sm} \end{array}\right] \{u_m\} + \left[\begin{array}{c} K_{is} \\ \hline K_{ms} \\ \hline K_{ss} \end{array}\right] [S_{sm}]\{u_m\} \right. \\ &\left. + \left[\begin{array}{c} K_{is} \\ \hline K_{ms} \\ \hline K_{ss} \end{array}\right] \{\triangle_d\} \right\} \cdot \left\{\begin{array}{c} w_i \\ \hline w_m \\ \hline w_s \end{array}\right\} = 0 \qquad \forall\, w. \end{aligned} \tag{B.19}$$

and, it is possible to arrange the above equation as

$$\begin{aligned} &\left\{ \left[\begin{array}{c} K_{ii} \\ \hline K_{mi} \\ \hline K_{si} \end{array}\right] \{u_i\} + \left[\begin{array}{c} K_{im} + K_{is}S_{sm} \\ \hline K_{mm} + K_{ms}S_{sm} \\ \hline K_{sm} + K_{ss}S_{sm} \end{array}\right] \{u_m\} \right. \\ &\left. + \left[\begin{array}{c} K_{is} \\ \hline K_{ms} \\ \hline K_{ss} \end{array}\right] \{\triangle_d\} \right\} \cdot \left\{\begin{array}{c} w_i \\ \hline w_m \\ \hline w_s \end{array}\right\} = 0 \qquad \forall\, w. \end{aligned} \tag{B.20}$$

Due to the boundary condition taking into account on the problem, it can be shown that the relationships of the displacement fluctuation field between of the boundary master and slave nodes writing in a matrix form is

$$\{w_s\} = [S_{sm}]\{w_m\}\,, \tag{B.21}$$

therefore, it is possible to reduce the system of equations shown in (B.20) as

$$\begin{aligned} &\left\{ \left[\begin{array}{c} K_{ii} \\ \hline K_{mi} + S_{sm}^T K_{si} \end{array}\right] \{u_i\} + \right. \\ &+ \left[\begin{array}{c} K_{im} + K_{is}S_{sm} \\ \hline K_{mm} + K_{ms}S_{sm} + S_{sm}^T K_{sm} + S_{sm}^T K_{ss} S_{sm} \end{array}\right] \{u_m\} + \\ &\left. + \left[\begin{array}{c} K_{is} \\ \hline K_{ms} + S_{sm}^T K_{ss} \end{array}\right] \{\triangle_d\} \right\} \cdot \left\{\begin{array}{c} w_i \\ \hline w_m \end{array}\right\} = 0 \qquad \forall\, w. \end{aligned} \tag{B.22}$$

Defining the reduced stiffness matrix, the reduced forces vector and the reduced displacements vector as

$$[K_r] = \left[\begin{array}{c|c} K_{ii} & K_{im}+K_{is}S_{sm} \\ \hline K_{mi}+S_{sm}^T K_{si} & K_{mm}+K_{ms}S_{sm}+S_{sm}^T K_{sm}+S_{sm}^T K_{ss} S_{sm} \end{array}\right], \tag{B.23}$$

$$\{u_r\} = \left\{\begin{array}{c} u_i \\ \hline u_m \end{array}\right\} \text{ and} \tag{B.24}$$

$$\{F_r\} = \left\{\left[\begin{array}{c} K_{is} \\ \hline K_{ms} + S_{sm}^T K_{ss} \end{array}\right] \{\triangle_d\}\right\}, \tag{B.25}$$

the starting problem has been reduced to

$$\{[K_r]\{u_r\} + \{F_r\}\} \cdot \{w_r\} = 0 \qquad \forall\ w. \tag{B.26}$$

Therefore, the reduced equation system to be solved is

$$\mathbf{K}_r \cdot \mathbf{u}_r = -\mathbf{F}_r. \tag{B.27}$$

Equation (B.27) shows that the degrees of freedom of the slave nodes are not included in the reduced displacements vector. The reduced equation system has less degrees of freedom than the original one and it also satisfies automatically the boundary conditions.

B.2.2 Non-linear implementation

Introducing the concept of master nodes and slave nodes into the equation system, it can be rewritten as

$$\begin{aligned} \left\{\left\{\begin{array}{c} F_i \\ \hline F_m \\ \hline F_s \end{array}\right\}^{(k-1)} + \left[\begin{array}{c|c|c} K_{ii} & K_{im} & K_{is} \\ \hline K_{mi} & K_{mm} & K_{ms} \\ \hline K_{si} & K_{sm} & K_{ss} \end{array}\right]^{(k-1)} \left\{\begin{array}{c} d_i \\ \hline d_m \\ \hline d_s \end{array}\right\}^{(k)}\right\} \\ \cdot \left\{\begin{array}{c} w_i \\ \hline w_m \\ \hline w_s \end{array}\right\} = 0 \qquad \forall\ w, \end{aligned} \tag{B.28}$$

where the subscripts i, m, and s refer to the degrees of freedom of the internal nodes, master nodes and slave nodes, respectively. Considering the update formula of the Newton-Raphson method for the master degrees of freedom as

$$\{u_m\}^{(k)} = \{u_m\}^{(k-1)} + \{d_m\}^{(k)}. \tag{B.29}$$

It is possible to write (B.18) in the current $k-th$ micro problem iteration as

$$\{u_s\}^{(k)} = [S_{sm}]\{u_m\}^{(k)} + \{\triangle_d\}^{(t)}, \tag{B.30}$$

where the superscript t is associated to the current iteration of the macro problem. Then, using (B.29) the above expression can be written as

$$\begin{aligned} \{u_s\}^{(k)} &= [S_{sm}]\{u_m\}^{(k-1)} + \{\triangle_d\}^{(t)} + [S_{sm}]\{d_m\}^{(k)}, \\ &= \{u_s\}^{(k-1)} + \{d_s\}^{(k)}, \end{aligned} \tag{B.31}$$

and the following relationships is found

$$\{d_s\}^{(k)} = [S_{sm}]\{d_m\}^{(k)}. \tag{B.32}$$

Introducing (B.32) in (B.28)

$$\left\{ \left\{ \begin{array}{c} F_i \\ \hline F_m \\ \hline F_s \end{array} \right\}^{(k-1)} + \left[\begin{array}{c} K_{ii} \\ \hline K_{mi} \\ \hline K_{si} \end{array} \right]^{(k-1)} \{d_i\}^{(k)} + \left[\begin{array}{c} K_{im} + K_{is}S_{sm} \\ \hline K_{mm} + K_{ms}S_{sm} \\ \hline K_{sm} + K_{ss}S_{sm} \end{array} \right]^{(k-1)} \{d_m\}^{(k)} \right\} \cdot \left\{ \begin{array}{c} w_i \\ \hline w_m \\ \hline w_s \end{array} \right\} = 0 \qquad \forall\, w. \tag{B.33}$$

Considering (B.21) in the above expression, it is possible to reduce the system of equations shown in (B.28) as

$$\left\{ \left\{ \begin{array}{c} F_i \\ \hline F_m + S_{sm}^T F_s \end{array} \right\}^{(k-1)} + \left[\begin{array}{c|c} K_{ii} & K_{im}+K_{is}S_{sm} \\ \hline K_{mi}+S_{sm}^T K_{si} & K_{mm}+K_{ms}S_{sm}+S_{sm}^T K_{sm}+S_{sm}^T K_{ss}S_{sm} \end{array} \right]^{(k-1)} \left\{ \begin{array}{c} d_i \\ \hline d_m \end{array} \right\}^{(k)} \right\} \cdot \left\{ \begin{array}{c} w_i \\ \hline w_m \end{array} \right\} = 0 \qquad \forall\, w, \tag{B.34}$$

or in its reduced form using the definitions of the previous section

$$\left\{ \{F_r\}^{(k-1)} + [K_r]^{(k-1)} \{d_r\}^{(k)} \right\} \cdot \{w_r\} = 0 \qquad \forall\, w. \tag{B.35}$$

Therefore, the reduced equation system to be solved is

$$\mathbf{K}_r^{(k-1)} \cdot \mathbf{d}_r^{(k)} = -\mathbf{F}_r^{(k-1)}. \tag{B.36}$$

Equation (B.36) shows that the degrees of freedom of the slave nodes are not included in the displacements vector even for the non-linear case and the reduced equation system also satisfies automatically the boundary conditions.

B.3 Derivatives of the shape functions

The finite element method uses the shape functions to approximate the continuous displacement field within the finite element domain. In general, the shape functions are defined in a iso-parametric domain, then

$$\mathbf{N} = \mathbf{N}(\boldsymbol{\xi}). \tag{B.37}$$

The derivatives of the shape functions are computed in the iso-parametric domain as

$$\mathbf{B}_\xi = \frac{\partial \mathbf{N}}{\partial \boldsymbol{\xi}} \quad ; \quad \mathbf{H}_\xi = \frac{\partial}{\partial \boldsymbol{\xi}}\left(\frac{\partial \mathbf{N}}{\partial \boldsymbol{\xi}}\right) = \frac{\partial \mathbf{B}_\xi}{\partial \boldsymbol{\xi}}. \tag{B.38}$$

Considering that the finite element domain is approximated as

$$\mathbf{X} = \mathbf{N}(\boldsymbol{\xi}) \cdot \bar{\mathbf{X}}, \tag{B.39}$$

where $\bar{\mathbf{X}}$ are the coordinate values of the finite element nodes in the element domain. Then, the Jacobian matrix which transforms the iso-parametric domain to the finite element domain, is defined as

$$\mathbf{J} = \frac{\partial \mathbf{X}}{\partial \boldsymbol{\xi}} = \frac{\partial \mathbf{N}}{\partial \boldsymbol{\xi}} \cdot \bar{\mathbf{X}} = \mathbf{B}_\xi \cdot \bar{\mathbf{X}} \tag{B.40}$$

and

$$\mathbf{J}^{-1} = \frac{\partial \boldsymbol{\xi}}{\partial \mathbf{X}} = \left[\mathbf{B}_\xi \cdot \bar{\mathbf{X}}\right]^{-1} \tag{B.41}$$

The shape functions and theirs derivatives have to be calculated in the finite element domain

$$\mathbf{N}(\mathbf{X}) \quad ; \quad \frac{\partial \mathbf{N}}{\partial \mathbf{X}} \quad ; \quad \frac{\partial}{\partial \mathbf{X}}\left(\frac{\partial \mathbf{N}}{\partial \mathbf{X}}\right). \tag{B.42}$$

Therefore, the values on the finite element domain are obtained as following

Value of the shape functions:

$$\mathbf{N}(\mathbf{X}) = \mathbf{N}(\boldsymbol{\xi}) \tag{B.43}$$

First derivative of the shape functions:

$$\mathbf{B} = \frac{\partial \mathbf{N}}{\partial \mathbf{X}} = \frac{\partial \mathbf{N}}{\partial \boldsymbol{\xi}} \cdot \frac{\partial \boldsymbol{\xi}}{\partial \mathbf{X}} = \mathbf{B}_\xi \cdot \mathbf{J}^{-1} \tag{B.44}$$

Second derivative of the shape functions:

$$\mathbf{H} = \frac{\partial}{\partial \mathbf{X}}\left(\frac{\partial \mathbf{N}}{\partial \mathbf{X}}\right) = \frac{\partial}{\partial \mathbf{X}}\left(\mathbf{B}_\xi \cdot \mathbf{J}^{-1}\right) = \frac{\partial}{\partial \boldsymbol{\xi}}\left(\mathbf{B}_\xi \cdot \mathbf{J}^{-1}\right) \cdot \mathbf{J}^{-1}, \tag{B.45}$$

and considering the above expression

$$\mathbf{H} = \mathbf{H}_\xi \cdot \mathbf{J}^{-1} \cdot \mathbf{J}^{-1} + \mathbf{B}_\xi \cdot \frac{\partial \mathbf{J}^{-1}}{\partial \boldsymbol{\xi}} \cdot \mathbf{J}^{-1}. \tag{B.46}$$

Taking intro account that

$$\mathbf{J} \cdot \mathbf{J}^{-1} = \mathbf{I} \tag{B.47}$$

and

$$\frac{\partial \mathbf{J}}{\partial \boldsymbol{\xi}} \cdot \mathbf{J}^{-1} + \mathbf{J} \cdot \frac{\partial \mathbf{J}^{-1}}{\partial \boldsymbol{\xi}} = \mathbf{0} \quad \Longleftrightarrow \quad \frac{\partial \mathbf{J}^{-1}}{\partial \boldsymbol{\xi}} = -\mathbf{J}^{-1} \cdot \frac{\partial \mathbf{J}}{\partial \boldsymbol{\xi}} \cdot \mathbf{J}^{-1}. \tag{B.48}$$

It is possible to obtain the unknown term as

$$\frac{\partial \mathbf{J}^{-1}}{\partial \boldsymbol{\xi}} = -\mathbf{J}^{-1} \cdot \bar{\mathbf{X}} \cdot \frac{\partial \mathbf{B}_\xi}{\partial \boldsymbol{\xi}} \cdot \mathbf{J}^{-1} = -\mathbf{J}^{-1} \cdot \bar{\mathbf{X}} \cdot \mathbf{H}_\xi \cdot \mathbf{J}^{-1}. \tag{B.49}$$

Therefore,

$$\mathbf{H} = \left(\mathbf{H}_\xi - \mathbf{B}_\xi \cdot \mathbf{J}^{-1} \cdot \bar{\mathbf{X}} \cdot \mathbf{H}_\xi\right) \cdot \mathbf{J}^{-1} \cdot \mathbf{J}^{-1}. \tag{B.50}$$

B.4 Derivation of displacement field, deformation gradient and gradient of the deformation gradient tensor

Displacement field:

Taking into account the previous consideration, the displacement field in the finite element domain can be approximated as

$$\mathbf{u} = \mathbf{N}(\boldsymbol{\xi}) \cdot \bar{\mathbf{u}}, \tag{B.51}$$

where $\bar{\mathbf{U}}$ are the displacement values of the finite element nodes in the element domain.

Deformation gradient tensor:

If the current configuration position of the structure is approximated as

$$\mathbf{x} = \mathbf{u} + \mathbf{X}, \tag{B.52}$$

where the deformation gradient tensor is obtained

$$\mathbf{F} = \nabla_0 \mathbf{x} = \frac{\partial \mathbf{u}}{\partial \mathbf{X}} + \mathbf{I} \tag{B.53}$$

then,

$$\mathbf{F} = \mathbf{B} \cdot \bar{\mathbf{u}} + \mathbf{I}. \tag{B.54}$$

Gradient of the deformation gradient tensor:

$$\mathbf{G} = \nabla_0 \mathbf{F} = \frac{\partial}{\partial \mathbf{X}} (\mathbf{B} \cdot \bar{\mathbf{u}}) \tag{B.55}$$

finally,

$$\mathbf{G} = \mathbf{H} \cdot \bar{\mathbf{u}}. \tag{B.56}$$

B.5 Numerical tangent constitutive tensor

The perturbation method used to obtain the homogenized tangent tensor of the RVE which was presented by Martinez et al. [71] is described in this appendix. The tangent constitutive tensor ($\mathbf{C}^t$) is defined as

$$\dot{\boldsymbol{\sigma}} = \mathbf{C}^t : \dot{\boldsymbol{\varepsilon}}. \tag{B.57}$$

The matrix description given by (B.57) can be written for orthotropic materials as

$$\begin{bmatrix} \dot{\sigma}_1 \\ \vdots \\ \dot{\sigma}_n \end{bmatrix} = \begin{bmatrix} C^t_{11} & \cdots & C^t_{1n} \\ \vdots & \ddots & \vdots \\ C^t_{n1} & \vdots & C^t_{nn} \end{bmatrix} \begin{bmatrix} \dot{\varepsilon}_1 \\ \vdots \\ \dot{\varepsilon}_n \end{bmatrix}. \tag{B.58}$$

The stress vector rate can be obtained as the sum of n stress vector, which are the product of the j component of the strain vector rate and the j column of the tangent tensor. Then

$$\dot{\boldsymbol{\sigma}} \equiv \sum_{j=1}^{n} \delta^j \boldsymbol{\sigma} = \sum_{j=1}^{n} \mathbf{C}^t_j . \delta\varepsilon_j, \tag{B.59}$$

where

$$\mathbf{C}^t_j = \begin{bmatrix} C^t_{1j} & C^t_{2j} & \cdots & C^t_{nj} \end{bmatrix}^T. \tag{B.60}$$

Equation (B.59) can be used to obtain the j column of the tangent constitutive tensor as

$$\boldsymbol{C}^t_j = \frac{^j\dot{\boldsymbol{\sigma}}}{\dot{\boldsymbol{\varepsilon}}_j} \equiv \frac{\delta^j \boldsymbol{\sigma}}{\delta \boldsymbol{\varepsilon}_j} \tag{B.61}$$

Therefore, the perturbation method consists in defining n small variations, or perturbation, of the strain vector $\delta\boldsymbol{\varepsilon}_j$, to obtain n stress vectors $\delta^j\boldsymbol{\sigma}$ to obtain the numerical approach given by (B.61) of the tangent constitutive tensor.

Appendix C
Scientific publications

The dissertation presented in this document has resulted from the following scientific publications,

F. Otero, X. Martinez, S. Oller and O. Salomon. Study and prediction of the mechanical performance of a nanotube-reinforced composite. Composite Structures. 2012, 94(9):2920-2930. doi: 10.1016/j.compstruct.2012.04.001.

F. Otero, S. Oller, X. Martinez and O. Salomon. Numerical homogenization for composite materials analysis. Comparison with other micro mechanical formulations. Composite Structures. 2015, 122:405-416. doi: 10.1016/j.compstruct.2014.11.041.

F. Otero, X. Martinez, S. Oller and O. Salomon. An efficient multi-scale method for non-linear analysis of composite structures. Composite Structures. 2015, 131:707-719. doi: 10.1016/j.compstruct.2015.06.006.

which are showing below.

Attention¡¡

Pages 120 to 181 of the thesis, containing the articles, are available at the editor's web

http://www.sciencedirect.com/science/article/pii/S0263822312001584
http://www.sciencedirect.com/science/article/pii/S0263822314006102
http://www.sciencedirect.com/science/article/pii/S0263822315004699